NOVEL WIRELESS SENSOR CONFIGURATIONS INCORPORATING ISOTROPIC RADIATORS ON CONFORMAL ARTIFICIAL MAGNETIC CONDUCTORS

A Thesis
Presented to
The Academic Faculty

by

James Roger Cooper

In Partial Fulfillment
of the Requirements for the Degree
Doctor of Philosophy in the
School of Electrical and Computer Engineering

Georgia Institute of Technology
August 2014

NOVEL WIRELESS SENSOR CONFIGURATIONS INCORPORATING ISOTROPIC RADIATORS ON CONFORMAL ARTIFICIAL MAGNETIC CONDUCTORS

Approved by:

Professor Manos M. Tentzeris,
Committee Chair
School of Electrical and Computer Engineering
Georgia Institute of Technology

Professor Manos M. Tentzeris, Advisor
School of Electrical and Computer Engineering
Georgia Institute of Technology

Professor Gregory D. Durgin
School of Electrical and Computer Engineering
Georgia Institute of Technology

Professor Paul G Steffes
School of Electrical and Computer Engineering
Georgia Institute of Technology

Date Approved: 15th of April, 2014

To my beautiful and loving wife,

Jennifer Lee Cooper,

who has been supporting and putting up with me through this process.

ACKNOWLEDGEMENTS

I wish to thank Dr. Tentzeris and the ATHENA research group of the Georgia Institute for Technology for their physical and moral support

National Science Foundation and the Graduate Research Fellowship Program for their financial support to have freedom to pursue a research project of my interest

Dr. Gregory David Durgin and Dr. Andrew F. Peterson of the Georgia Insistute of Technology, and Dr. Thomas Weller, Dr. James Leffew and Dr. Arthur David Snider of the University of South Florida for lending their knowledge and expertise to better understand the principles of electromagnetics

Dr. William N. Carr of New Jersey Microsystems for giving me the opportunity to put my knowledge into practice

TABLE OF CONTENTS

LIST OF TABLES

LIST OF FIGURES

SUMMARY

The objective of the presented research is to develop a novel, ink-jet printed, chipless, passive, wireless sensor topology, which can radiate in a near isotropic pattern without interference from embedded devices, for use in dispersed sensor networks. This objective includes the development of a hardware based, uniquely identifiable, collision avoidance communication method, and an integrated sensor system that is easily integrated into the topology.

Wireless sensor networks can be and are used in military, medical and industrial applications; and the demand for them is ever growing. However, current sensor networks have various trade-offs and limitations, including cost, number of distinguishable nodes, and ease of manufacturing. These trade-offs lead to unique sensors needing to be designed for each situation. To develop a widely used module, a topology must be developed that can meet as many demands as possible with fair tradeoffs.

Many of the above proposed criteria for the topology are already integrated into RFID technology. Therefore, much of the research is the application and advancement of current RFID technology for the purpose of designing the topology. The research begins with the theory and design of conformal artificial magnetic conductors, which is used in the design of a near isotropic radiator and isolated core for device embedding. Then, novel fabrication techniques will be investigated and deployed in the fabrication of the topology. Next, a novel "smart skin" sensor is developed which is easily integrated into the desired fabrication technique. Finally, an anti-collision RFID circuit for on-tag placement, which is based on frequency-doubling transceivers, is designed, which can also be easily integrated into the final topology.

This module is designed for use with a variety of different sensors. This versatility

gives it ruggedness for use in many different environments. For proof of concept, this topology is fabricated and tested against current commercially sold tags.

Through the design and testing of the radiator, circuitry, and embedded sensors, it is shown that this design is a suitable topology for use in many different environments and applications.

CHAPTER I

INTRODUCTION

The problem presented within is that of the creation of a novel RFID-based, wireless sensor topology. To describe the design topology and why the topology is chosen, it is first necessary to clearly and concisely define RFID and RFID-based sensors. For this particular topology, it is also necessary to cover the topics of isotropic radiators, low cost circuit fabrication methods, and artificial magnetic conductors. Therefore, this chapter opens with a description of what RFID is and what are some current methods of designing and using it. Next, the chapter covers antennas, wireless sensors, and fabrication for RFID-based systems. Finally, artificial magnetic conductors, their purpose and design is covered.

1.1 Radio Frequency Identification

Radio frequency identification, RFID, is a means of tagging items for tracking and/or identification. This tagging can be for tracking a product's parts as they move through an assembly line, identifying individuals for allowing access into secured locations [44], tracking cattle to protect against the spread of disease, tracking cars as they pass through a toll booth [41], and scanning for inventory and purchase check-out in stores. Similar to a barcode scanner, an RFID system includes a scanning device, here on referred to as an interrogator, that transmits a signal and reads a returned signal, and a tag, that receives, modulates, and reflects the interrogator's signal. The major difference between barcode scanners and RFID is the need for clear line of site between the interrogator and the tag. An RFID system uses a modulated RF signals, usually in the range from 125 kHz to 960 MHz [45]. This use of RF signals allows for an RFID interrogator to be able to communicate with a tag independent of visibility

or orientation, at much greater distances, and in much harsher environments than a barcode scanner. This visibility independence gives RFID the potential to be more robust and simpler to use than a barcode system.

As previously mentioned, the interrogator and the tag are the two fundamental parts to an RFID system. The interrogator contains a local oscillator that generates the carrier signal. Along with the local oscillator, it may also contain a switch or mixer for modulation of the carrier signal, generated by the local oscillator, with a data signal. The interrogator generates the complete signal that is sent to a tag. The interrogator also contains a method of demodulation, a sampler for use with conversion from time to frequency domain or a mixer for down conversion; and a processor for analyzing the returned data. Because of the complexity, the interrogator tends to be the most expensive part of an RFID system. However, because an RFID system only requires the use of a single reader, it is not necessarily the largest cost in the implementation of an RFID system.

The tags for RFID systems normally contain some method of signal modulation. This modulation could be from a mounted IC that receives a magnitude modulated signal and then generates its own magnitude modulated signal through a series of MOSFET-based switches; a series of resonators that phase and magnitude modulate, then reflect, an interrogator's signal [65]; or, a surface acoustic wave, SAW, device that receives a wide-band pulse from an interrogator and reflects several phase modulated pulses back [63] to the interrogator. The modulation on the tag's end is used to uniquely identify the item to which the tag is attached, create a method for determining position of the tag, and/or to show a change in the state of the tag or item that the tag is attached.

Fig 1.1 depicts an interrogator communicating with a single RFID tag. The interrogator (right) transmits a signal. This signal activates the tag (left). The now activated tag then re-transmits back to the interrogator. The interrogator then

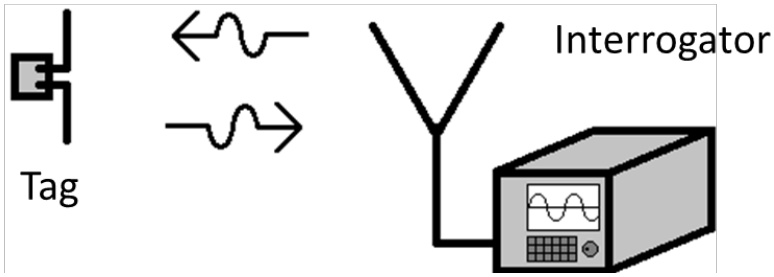

Figure 1.1: A diagram of the working parts of an RFID system

processes the re-transmitted signal.

When designing an RFID system several factors are to be considered. These factors can include whether the system relies on active or passive tags, whether the tags have integrated circuit chips or use another method for identification, whether the tags are fully printable or need more complex fabrication methods, and whether the tags are used for identification, embedded sensing, or both. The subsections to follow are meant to give an overview of the current designs in RFID tags that exist today. This overview is for the purpose of clearly defining why the particular design, which will be presented in chapter II, was chosen to have the characteristics the presented design possesses.

1.1.1 Active, Passive, and Semiactive RFID

RFID tags can be classified by existence of a power supply, method of processing data, and maximum range of communication [63]. For the sake of this section, RFID tags will be classified by the tag's power supply and will be labeled as active, passive or semiactive/semipassive.

Active tags make use of an on-board power supply for use in both data processing and signal amplification. This on-board power supply has traditionally been a battery. However, in more recent developments, tags have made use of energy scavenging for power [82].

Passive tags, as the name implies, rely completely on power received from an

interrogator's signal to process, modulate, and retransmit data without the need to have an internal energy source. Passive tags have the advantage of not needing to be replaced or recharged, as with active tags. The lack of a battery and amplifier also gives the passive tag the ability to be much more compact and have a lower cost by comparison with active tags. The drawback is that passive tags have a far shorter read range (the maximum range that an interrogator can activate a tag and receive a cohesive signal back) than an active tag. Also, the passive tag has more limitations on how much data processing it can perform in comparison to an active tag, thus limiting its ability to perform tasks such as encryption for security.

Semiactive tags, like an active tag, use an onboard power supply, but only use it for data processing. Like the passive tag, they rely on the interrogator's signal for powering the retransmission of data. Because the onboard processing unit does not require external power, the semiactive tag is able to activate under lower power levels than a passive tag, and is able to use more of the original interrogator's power for retransmitting. Thus it is able to achieve longer read ranges than the passive tag. Also, since the processor is powered, it is able to perform more complex data processing, such as encryption, like the active tag. Because, the battery is only used for data processing and not for amplification, the tag requires less power from the battery and thus can go longer amounts of time between being recharged or replaced [63].

1.1.2 Chipless RFID

RFID tags can also be classified by whether or not they include an integrated circuit, or IC. IC-based RFID tags use some form of encoding, where a signal carrying a serial of bits are sent from an interrogator to the tag, that activates the tag. Once activated, the chip will respond with a signal containing its own identifying serial of bits. The bits are generated by a series of switches, normally FET, that modulate

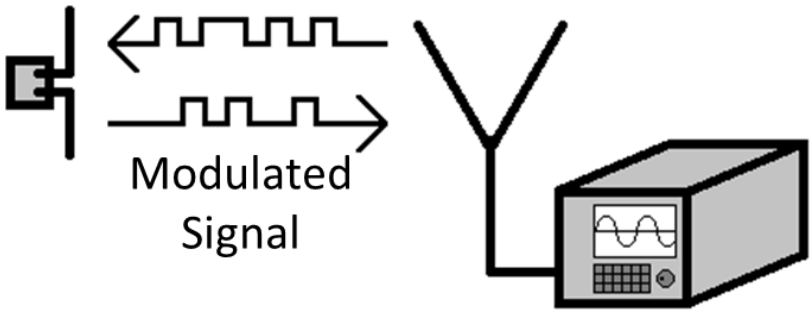

Figure 1.2: A diagram of the working parts of an RFID system demonstrating amplitude modulated communication from an IC

the carrier signal from the interrogator.

Fig 1.2 depicts the communication between an interrogator and an RFID tag using serial binary data on a modulated carrier. The interrogator (right) first sends a modulated signal carrying binary data. The tag (left) receives the signal and uses the carrier to create a new modulated signal. This new modulated signal is then sent back to the interrogator.

As for chipless RFID tags, many different methods for generating a returned signal exist. Most chipless tags use some form of modulated backscatter measurement. The most common method of modulation is the use of narrow band resonators [64, 65] on a transmission line. In this method, a wideband signal is used to excite a tag. The tag is comprised of a receive antenna (that may or may not also be the transmit antenna), a transmission line, and an array of resonators that resonate at different frequencies. When the broadband signal excites the tag, the signal is reflected back at the interrogator. At frequencies where there exists a resonator on the transmission line, the signal is attenuated and phase shifted. At frequencies that do not have a corresponding resonator on the transmission line, the signal does not receive attenuation or phase shift [64, 65]; or it receives a different amount of attenuation and phase shift.

Fig 1.3 shows a broadband signal, depicted by the frequency domain, amplitude plot on the left, exciting a resonator-based tag, depicted in the center. As the signal

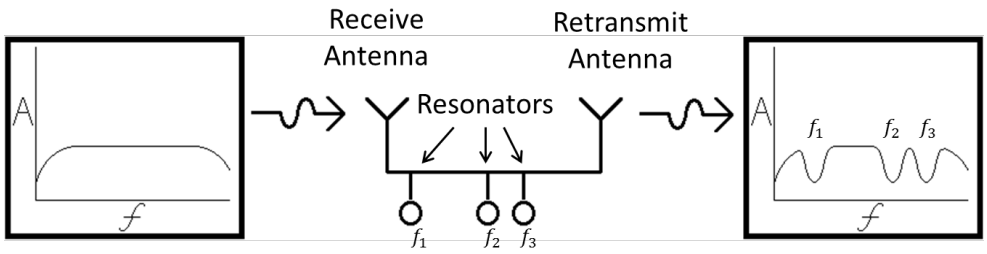

Figure 1.3: Frequency domain plot of interrogation signal before and after passing through a resonator-based, chipless RFID

passes through the tag, it will pass multiple resonators at different frequencies before being retransmitted. The retransmitted broadband signal, depicted by the frequency domain, amplitude plot on the right, will then have attenuation at each frequency that there was a resonator.

The above described method has the benefit that each discrete frequency can act as a single bit. The presence of a resonator determines whether a 1 or 0 is sent back, thus giving each tag an individual identification. If a co-planar method is used [66], the entire tag can be printed in a single, simple step, thus making the chip available for cheaper mass production than when using an IC.

The drawbacks of resonator-based tags are that they require a strong method of preventing backscatter interference; a method of preventing collisions between return signals of multiple tags does not exist; the size of the resonators is comparable to that of a single wavelength of the signal and a resonator is needed for every bit with a value of 1 (or every bit with a value of 0, depending on the reader's configuration), which can lead the tag to being very large; and, the orientation of the tag with respect to the interrogator must be controlled to receive a proper reading. These drawbacks limit the use or resonator-based tags to short ranged readers in a well controlled environments, such as tagged products on a conveyor belts.

A limited solution to the size constraint is the use of varying lengths of transmission lines instead of resonators [12, 58]. In this method, only a phase shift, not

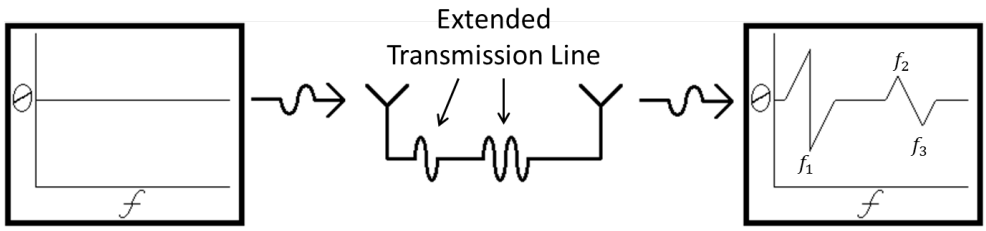

Figure 1.4: Phase of interrogation signal, in frequency domain, before and after passing through a delay-line-based, chipless RFID

amplitude attenuation, is used to determine bit values.

Fig 1.4 depicts a broadband signal, represented by the frequency domain plot on the left, exciting a delay-line-based RFID tag. The tag contains meandered transmission lines to induce a phase shift in the broadband signal. A frequency domain plot of the phase of the broadband signal, after being retransmitted, can be seen on the right. The meandered transmission lines' lengths were chosen so as to induce a phase shift at three distinct frequencies.

Both the resonator-based and delay-line-based methods are prone to backscatter interference. By having two separate antennas, one for receive and one for retransmit, interference by backscatter can be decreased for both resonator-based and delay-line-based tag. This backscatter reduction is achieved by making the antennas have orthogonal orientations [65], and having the interrogator only read from a certain polarization. Although good at eliminating backscatter interference, it further limits freedom in a tags orientation.

Instead of resonator or delay-line-based tags, another method of using backscatter response over a wide bandwidth is to use an array of shorted antennas [4] or resonant structures [56]. In this method a sweep is taken over a wide bandwidth where each discretely measured frequency is a bit. Like in the resonator structure described above, the existence of an antenna/resonant structure determines whether the bit is a 1 or 0. The difference is that the interrogator measures the direct backscatter of the tag, whereas the previous method, the tag receives, modulates, and returns

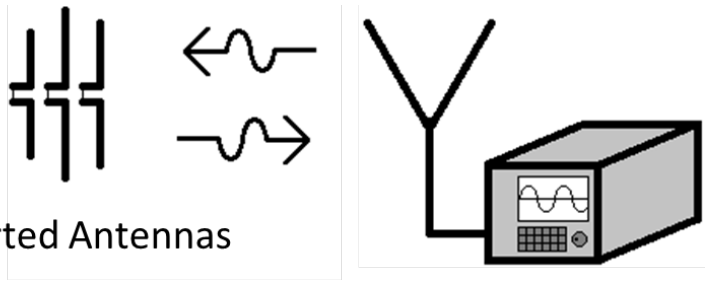

Figure 1.5: A diagram of an RFID system utilizing shorted dipoles as resonant strucutures for interrogation signal modulation

a signal. This method has most of the same advantages and disadvantages of the resonator-based tags. However, since direct backscatter, instead of a received and retransmitted, signal, cross polarized antennas cannot be used to avoid interference from unwanted backscatter.

Fig 1.5 depicts the backscatter from a series of resonant structures when excited by an interrogator. The resonators are represented by the three shorted dipoles on the left. Each dipole will cause a disturbance at a specific frequency, that the interrogator, on the right, will detect.

Chipless RFID systems also include tags with surface mount components. These include SAW and frequency-doubling methods that will be covered in the following two sections.

1.1.3 SAW-based RFID

Surface Acoustic Wave, or SAW, -based RFID systems operate by utilizing the properties of piezo-electric materials. A SAW is an electro-mechanical wave which propagates along the surface of a piezo-electric material. When an interdigitated transducer, placed on a piezo material, is excited by an electric signal, the energy from the signal is converted into a SAW. This SAW travels linearly across the surface of the piezo material until it hits a metal reflector planted in the piezo material. Depending on the dimension of the reflector, either some of or the entire SAW is reflected back towards the transducer. When the reflected SAW reaches the transducer, the

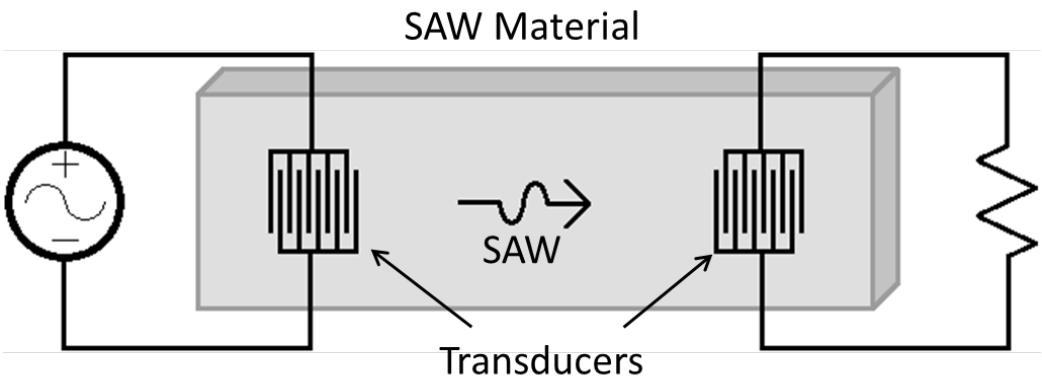

Figure 1.6: A diagram of the basic operation of surface accoustic wave, SAW, traveling across a piezo-electric material

reflected SAW is converted back into an electric signal. Because SAWs travel slower than electric signals down a wire, a significantly greater time delay is introduced into the reflected signal than had the signal just traveled down a transmission line of the same length.

The basic operation of a SAW-based device, using two transducers, can be seen in Fig 1.6. In the figure, a source (left) can be seen feeding an interdigitated transducer. A SAW, created by the transducer, travels linearly along a ballistic path until it hits the second transducer (right).

For SAW-based RFID systems, a tag consists of an antenna connected to a SAW device. This SAW device consists of the piezo-electric material, the transducer (or transducers), and a series of reflectors. An interrogator transmits a signal, that consists of a bandwidth limited pulse, that excites the tag. The tag will then modulate and retransmit the pulse. The modulated pulse is then used to identify the tag. If multiple reflectors are placed in the SAW material, then multiple pulses will be returned to the interrogator. Each returned pulse will carry bit information about the tag thus allowing for multi-bit identification of the tag [54].

Fig 1.7 depicts the operation of a SAW-based tag. In the figure are shown the antenna, the interdigitated transducer, one reference reflector, and three bit-encoded

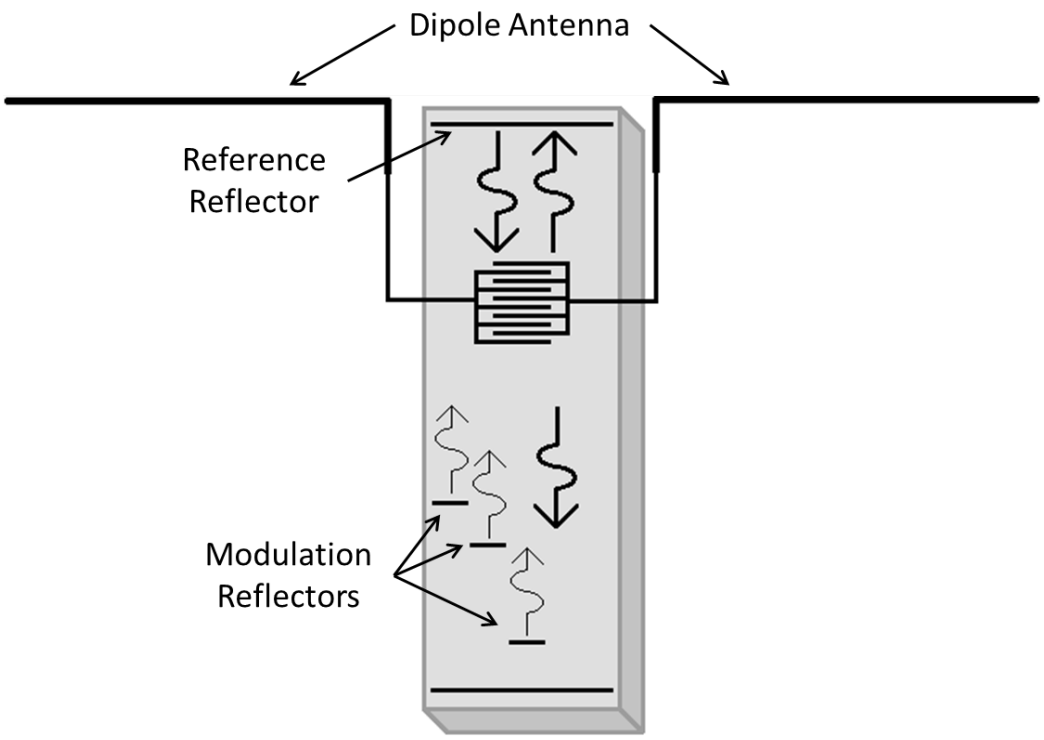

Figure 1.7: A diagram of the basic operation of SAW-based RFID tag

reflectors. The bit-encoded reflectors receive their bit encoding based on the distance between the reflectors and the interdigitated transducer.

Other materials do exist that allow for an electrically excited slow moving wave, like SAW. The advantage of SAW is that it can operate in higher frequencies, 100MHz to low GHz, than other known materials [35].

This system is very simple since it only needs one antenna for receiving and transmitting, and only one on-board component for generating the modulated, data carrying signal. The SAW tag can also carry a large number of bits, enough to meet international EPC regulations, while still requiring only a single small surface mount device [40]. The requirement of only a single surface mount component is the same as with ICs. The advantage of SAW over IC is that a need for A/D converters does not exist, which means the SAW consumes less power. This reduction in power means that the SAW has a longer read range than passive ICs [40]. The disadvantage is in

its achievable collision resolution [5]. Achievable collision resolution is the number of tags that can exist within the read range of the interrogator and still be individually recognizable. ICs can have a much higher resolution since they can be turned on and off by a control signal. SAW-based tags, on the other hand, are always in the on state [39].

It should be mentioned that the resolution can be increased through the use of post processing. Methods that are currently used include signal strength discrimination, time separation, spatial discrimination based on antenna radiation pattern, code division separation, and signal subtraction [39].

SAW-based tags have a major disadvantage over other chipless RFID tags in that they cannot be simply manufactured. While many of the chipless RFID tag topologies can be directly printed onto a substrate, the SAW tags require for the manufacturing of a cased piezo-electric material with deposited reflectors. The case then needs to be mounted on the tag, which adds more complexity.

However, SAW devices have a major advantage over resonator-based RFID in that they can be made much smaller. SAWs travel at much slower rates than EM signals on a transmission line. Therefore, large time delays can be achieved in a relatively small area. Also, SAW devices can use multiple reflectors in the same surface mount package, allowing for multiple bits to be stored in a single package. This ability to have multiple bits in a single device is as appose to resonator-based RFID that requires a single resonator for each 1 (or 0) bit.

A large amount of research has been done to reduce the size of a SAW surface mount device. This research has included the use of unidirectional transducers in conjuncture with large on-board reflectors that cause the SAW to travel in a Z-shaped path instead of a straight line; use of each reflector to represent multiple bits [37]; the use of bi-directional transducers in conjuncture with multichannel geometries [75]; and using phase as well as time delay to double the number of bits used in each

reflector [38]. The previously mentioned methods of reducing the size of SAW-based tags make SAW tags much smaller than most chipless RFID tags.

1.1.4 Frequency Doublers

The major disadvantage of the resonator-based RFID systems, and a minor disadvantage in many other types of chipless RFID, is the difficulty in being able to discriminate between backscatter that comes from the tag and backscatter that comes from reflections off of objects in the surrounding areas. Because of these random backscattered signals, many resonator-based methods require exact placement of the tags in relation to an interrogator and use of very short distances. The effects of backscatter interference can be overcome with the use of frequency-doubling RFID tags; a method that has been in use since 1979 [33].

In the basic frequency-doubling-based RFID system, the interrogator sends out a signal at a single frequency. The tag receives the signal and feeds it into a full-wave [2] or half-wave rectifier [1]. The rectifier will generate harmonics of the original signal. The generated second harmonic, or signal at twice the fundamental/original frequency of the signal, is then retransmitted. The use of a second harmonic signal lets the interrogator read a returned signal at a separate frequency from what was original transmitted and prevents interference from unwanted reflections.

Fig 1.8 shows the circuit diagram for a half-wave (left) and full-wave (right) rectifier circuit connected to a source and load. The non-linear characteristics of the diodes are what rectifies, and thus generates harmonics of, the received signal. Fig 1.9 depicts an interrogation signal before and after it passes through a full-wave rectifying frequency-doubling tag. The top plots show the time domain amplitude of the signal, while the bottom plots show the frequency domain.

In addition to avoiding backscatter interference, the frequency-doubling tag has

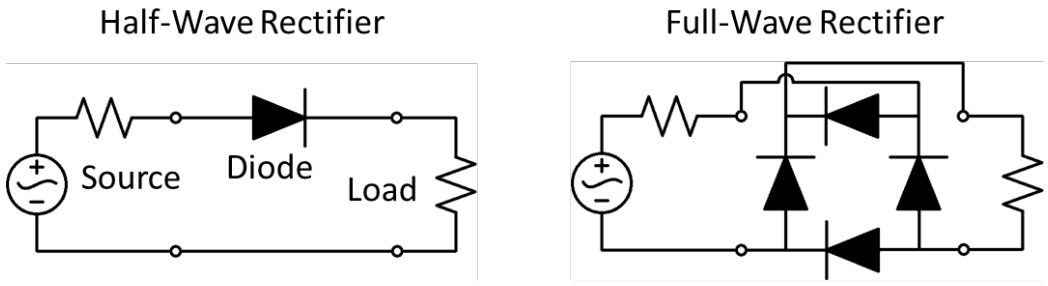

Figure 1.8: Circuit Diagrams of a half-wave (left) and full-wave (right) rectifier circuit

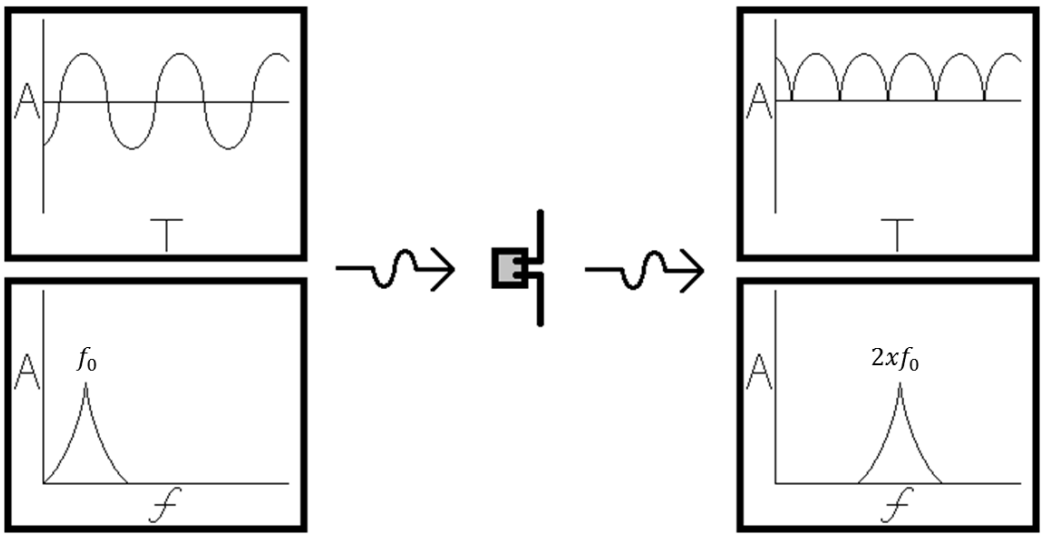

Figure 1.9: Plots of the time domain and frequency domain amplitude of an interrogation signal before and after passing though a full-wave rectifier

the advantages of lower power consumption over IC-based tags because the components consist of just one or four diodes. Like IC and SAW-based device, the doubler transceiver can also be very small in size compared to resonator-based RFID. The size constraint has made doubler transceivers very practical in size constraining applications, such as tracking flies and other small bugs [13]. Research in graphene has shown the potential for even smaller, higher efficiency frequency doublers [83]. Unlike the SAW devices, the frequency-doubling transponder relies on a standard surface mount component that is very inexpensive, and, because of the simplicity, very reliable [10].

The frequency-doubling transponder is also completely printable because of recent research in semiconductor printing [70]. These printed schotkey diodes have been printed on transponders on organic materials such as paper [62]. The ability to cheaply print the diodes, as well as the ability to print them on organic substrates, means that the transponders can be made cheaply and have limited environmental impact.

The major disadvantage in comparison to IC-based tags is that the frequency-doubling methodology is built around the idea of only a single device being in the range of the interrogator. No inherent methods for individual tag identification, or for preventing collisions between multiple tags, exist. However, because the advantages are so major, it is worth investigating methods that limit the disadvantages to use frequency doublers in more applications. A possible method is covered in chapter 2.

1.2 Antennas, Sensors, and Fabrication

Thus far, covered in this chapter have been the different types of RFID systems that currently exist. The focus has been kept on the method of modulation used within the structure of the tag. What has not been fully covered is the design of the rest of the tag and alternative uses for RFID tags. Within this section, an attempt is made to cover three topics that are crucial to modern RFID. The first is the design of

an antenna for the tag. Outside of resonator-based backscatter tags, that have very limited functionality [4, 56], every RFID needs some added method of receiving and re-radiating signals. Thus the design of an antenna is crucial to RFID design.

The second topic covered in this section is the use of RFID systems for sensing applications. Whether in industrial, medical, military, or even personal ad-hoc systems, it is necessary to be able to detect and/or measure the vitals of a system. Thus sensors are in high demand, and RFID-based sensors are able to meet many needs.

The final topic will cover fabrication of RFID tags. When it becomes necessary to track large numbers, on the order of thousands or millions, the cost, ease, and environmental impact of fabrication of a tag becomes very significant. Thus, constant research in the area of novel manufacturing techniques, which plays a significant role in the viability of RFID systems, is being done.

1.2.1 Antennas and Isotropic Radiators

An ideal isotropic radiating antenna is an antenna that transmits power in all directions equally. The maximum gain of an antenna, hereon referred to as just gain, is the maximum amount of power, measured in dBi, transmitted in a single direction by an antenna. For example, an isotropic antenna has a gain of 0 dBi, while a half-wave dipole has a gain of 2.15 dBi. A high gain antenna allows for large amounts of power to be transmitted over long distances than a low gain antenna. However, high gain antennas require controlled directioning, or else the power will be transmitted away from the desired point. Near isotropic radiating antennas don't require any type of orienting, but they radiate a very small amount of power in any given direction.

Isotropic radiators can be classified by how much their directivity varies across all points of an imaginary sphere centered on the antenna. From here on in, this quantity will be known as the variance. Examples of near isotropic radiators include, a dipole with a parasitic split ring on kapton with >9dB variance [47]; a miniature

phased array of orthogonally oriented monopoles with >8dB variance [42]; and two crossed dipoles with varience >4 dB [59].

When designing an RFID system, it is important to know what control will be had over the positioning and orientation of a tag. If the position and orientation are fixed, such as items passing under an interrogator on a conveyor belt, a linearly-polarized antenna with high gain can be used. The use of linearly-polarized, high-gain antennas will allow for higher power transfer from the interrogator to the IC/SAW device, and thus put fewer constraints on the tag for method of processing the interrogator signal and generating the return signal.

However, if the tag is placed in an arbitrary or random manner, than a high gain antenna may not be able to communicate with the interrogator if it is radiating power in the opposite direction. In this case, it is necessary to use a low gain, or near isotropic radiating antenna. An isotropic radiating tag can be dropped into any environment, and since it radiates in all directions, it will be able to communicate with the interrogator. The disadvantage of the isotropic to the high gain is that the isotropic tag will then take less power from any given single direction and will radiate energy in all directions, not just the direction of the interrogator. The reduction in power transfer means that either the tag needs to have an amplifier on board, or the maximum distance between the interrogator and tag will have to be reduced from that of a high gain radiator.

An illustration of the fundamental difference between a high directionality and low directionality antenna can be seen in Fig 1.10. In the center is an interrogator attempting to communicate with remote tags. On the left is a low directivity tag that can communicate in any direction, but that receives and sends back limited power from and to the interrogator. On the right are two tags with high gain antennas. One of the tags is able to receive and transmit a lot of power between itself and the interrogator. However, the other tag is unable to communicate at all as it is pointed

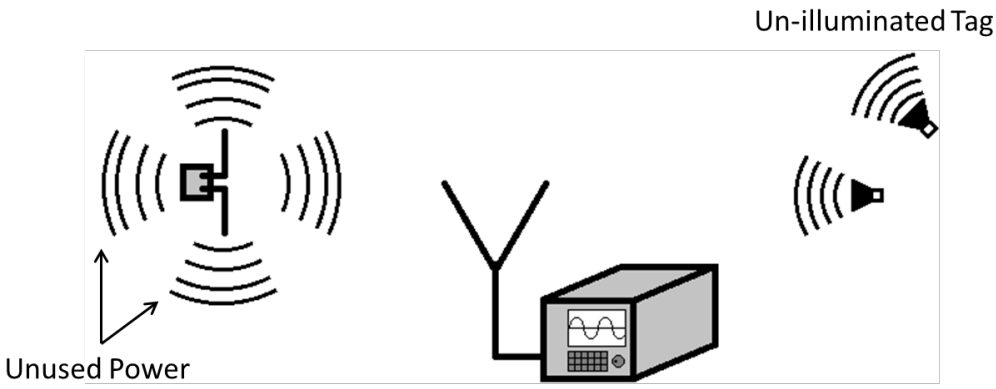

Figure 1.10: Diagram of an RFID system containing low (left) and high (right) directivity tags

in the wrong direction.

Another consideration is the necessary bandwidth versus the size of the antenna. Since methods for shrinking antennas, such as meandering, reduce bandwidth, electrically small antennas can only be used in narrowband applications, such as IC-chip-based tags that only require operation at a single frequency. Half-wavelength antennas, such as dipoles, can use notching or coupled lines for dual band operation and still be kept narrow. Thus frequency doubling can be used on small antennas. However, if it is desired to use a passive, bit encoded device such as SAW or resonators, a broadband antenna is required, which means a larger size.

1.2.2 RFID-based Sensors

Whether in the field of industry, military, medical, or even personal, the ability to sense or detect the state of a system is an important one. The problem comes in that environments are not always friendly when it comes to wired sensor placement. The problem environments include environments that contain corrosive agents that could eat through wire; environments that require a lot of sensors and wiring would take up more room or weigh more than is possible and/or practical; environments that do not allow for lines to run from the point where sensing is necessary to the point where

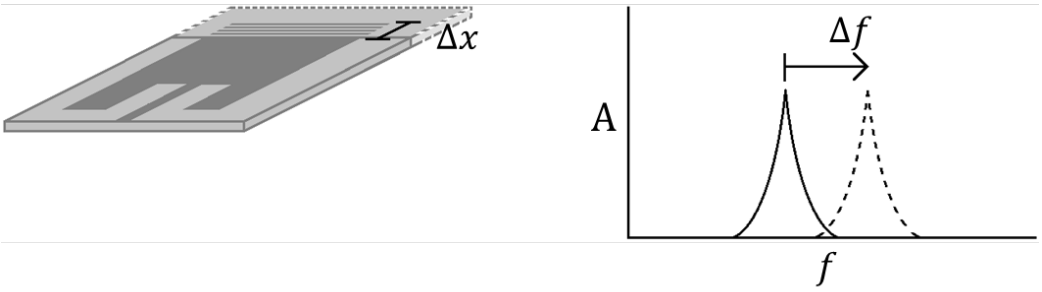

Figure 1.11: A patch antenna, distorted from a source of strain (left) and the resulting shift in resonant frequency (right)

an observer is located. In all of these environments, wireless communication with a sensor is the preferred approach.

The two responsibilities of these wireless sensors are that they are able to detect some aspect of their environment, and that they are able to communicate back to an observer or interrogator what is being detected. It is the latter that makes RFID a great solution. Since the root function of RFID is to transmit encoded data back to an interrogator, it intrinsically has the ability to transmit encoded data taken from a sensor.

A common method of using RFID for detection is by measuring shifts in the optimal operating frequency of an RFID tag, such as in strain measurements of civil structures [86]. For strain measurements, a frequency-doubling transceiver has one antenna securely glued to the structure. When strain applied, the antenna deforms and the optimal frequency of operation shifts. The interrogator uses a narrowband of excitation frequencies and looks for shifts in the optimal frequency.

Fig 1.11 shows a depiction of a patch antenna, as well as a frequency domain plot of its performance. The left image shows a change in shape caused by an application of strain. The right image shows a shift in the antenna's performance caused by the strain.

Outside of direct strain sensing, a shift in frequency can also be obtained by

attaching a load to an antenna that will have a shift in its complex impedance when the environment changes. The shift in the load means that the antenna is better matched at a different frequency, resulting in a change in optimal frequency. The shift in optimal frequency can be done by creating a matching network with the sensor/load embedded, so that when the environment shifts the matching network will match better to a different frequency. The shifting of optimal frequency can be done in a chip-based [32] or frequency-doubling system [67]. Another way is to place the sensor directly in the antenna [85], that will shift the operating frequency of the antenna as the electrical properties of the sensor shift. Both the strain sensing [86] and embedded load [85] RFID-based sensors are known as smart skin sensors.

Another method of RFID-based sensing is based on pulse response delay. In the pulse-response-delay method, a broadband pulse is sent out and multiple pulses are returned, each with a different time and phase delay. The time and phase delay can be done with a long transmission line terminated in a near completely imaginary load [12,58]. If the load is made of a material that shifts in electrical properties when in the presence of a gas, such as ethanol or ammonia, there will be a corresponding phase shift in the reflected signal that corresponds with the levels of gas [72, 77]. The time and phase delay can also be done with SAW tags that are known to be temperature dependent. When there is an increase in temperature, a larger delay between reflected pulses [68] exists.

1.2.3 Fabrication Methods

Major concerns in the areas of RFID tags and RFID-based sensors, outside of their modes of operation, are the cost and ease of fabrication, and the environmental impact of both constructing and disposing of tags. The larger the number of tags/sensors that need to be deployed means a greater concern in these areas. Therefore, many efforts are being put together to find new ways to construct tags/sensors that are low

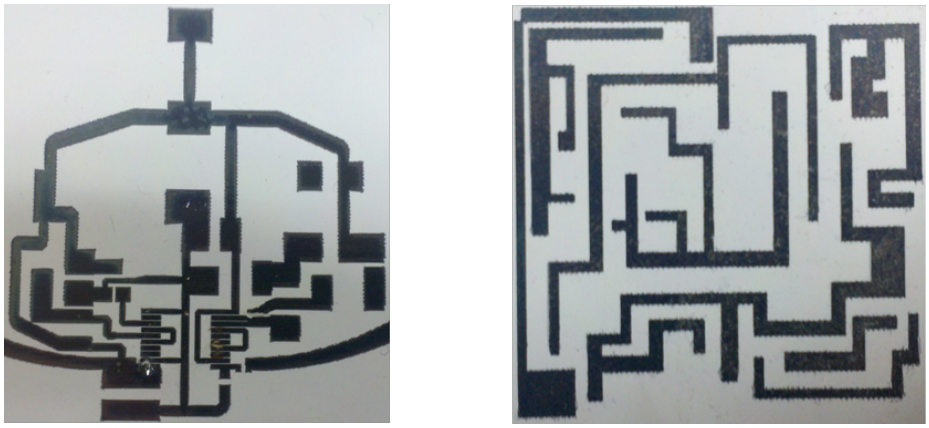

Figure 1.12: Images of inkjet printed circuits on paper substrates

cost and have less impact on the environment.

To reduce environmental impact, research has been done, and is continuing to be done, on the use of organic substrates. A common organic substrate is paper. Two inkjet printed circuits on a paper substrate can be seen in fig 1.12. Again and again, the viability of using inkjet printing technology to print conductive inks, commonly silver nano-particles, directly onto the paper [2,62,69] has been shown. Going beyond just conductive lines, one of the smart skin devices, previously mentioned in the previous section, used multiple depositions [85]. First the conductive ink was printed, then, using the same printer, a patch of single wall carbon nanotubes was deposited and cured.

Even without the use of paper substrates, inkjet printing has a lower environmental impact than the subtractive methods that are currently widely used [2, 62, 69].

Other methods of reducing environmental impact include the use of renewable energy sources for active tags. Instead of batteries, that have a limited number of charges and high environmental impact, using energy scavenging, such as solar cells, in conjunction with super capacitors can lead to low impact tags [81, 85].

For a reduction in cost, inkjet printing on paper substrates also promises a large payoff [2, 62, 81]. Inkjet printing uses less material in the manufacturing process, because it uses an additive process instead of a subtractive, like in etching. Paper

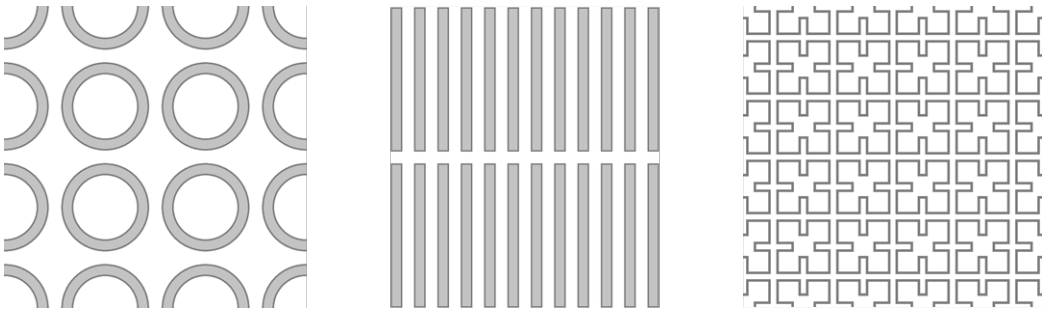

Figure 1.13: Images of different commonly used resonant structures in a planar array for use in frequency selective surfaces, or FSS

substrates mean lower prices since paper is far more abundant and cheaper to manufacture than FR4 or other common substrates.

1.3 FSS and AMC

Frequency Selective Surfaces, or FSS, are arrays of repeating structures that act as frequency-based filters for propagating waves. A simple FSS is a 2-D array of printed or etched resonant structure, such as shorted dipoles, loops, or more complex resonators [60]. More complex designs can include layers of stacked dielectric rods, long lines on thin dielectric slabs [8], and resonant structure linked with lumped elements [6].

Fig 1.13 shows some different, printable, 2-D configurations for creating FSS's. From left to right in the figure, depicted are an array of ring resonators, an array of shorted dipoles, and an array of 2nd generation convoluted squares.

FSS are of interest due to several inherent properties; One of which is the ability for an FSS to act as band-pass or band-stop filter for TEM waves. This ability makes them useful in multi-band reflector-antennas [61] and in free-space-beam splitters [36]. Another inherent property of interest is that when designed to be band-stop filters and placed over a ground plane, they can appear as infinite impedance or artificial magnetically conducting, AMC, surfaces. This property of acting as an AMC makes them very useful reflectors for dipoles and other compact antennas [36] for increasing

the directivity.

The 2-D FSS has been shown to be fully operational when working at angles in excess 45° incidence, as long as the elements and their spacing are small [46]. The ability to operate at wide angels makes them useful in half-plane radiation antennas, such as monopoles [20].

1.3.1 AMCs

Artifical Magnetic Conductor, AMC, structures are very similar to FSS. The key difference in structure is that an AMC is placed over a ground plane, while an FSS is used in free space. Although the constructions are similar, three major differences, electrically, exist between the AMCs and FSS. First is that the AMC always has a magnitude reflection coefficient of 1, while an FSS transitions between appearing as a PEC and a transparent surface, the AMC transitions between a PEC and an AMC. Second is that near the frequency of resonance, the angle of the reflection coefficient is negated. This negation of the reflection coefficient can become useful when trying to generate a matching scheme with shifting impedance [73]. Third, is that the AMC, because of the ground plane, creates perfect isolation on either side of the structure, i.e. if an antenna is placed over the AMC on one side, than neither can the antenna effect what's on the other side of the AMC, nor can anything on the other side interfere with the antenna.

1.3.2 FSS and AMC Image Theory

As previously mentioned, FSS are often used as reflectors for increasing the directivity of antennas. Because of their similar operation, AMCs are also found to be useful as reflectors. The reason for AMC's usefulness as reflectors can be found in the concept of image theory.

When a wave hits a barrier that has different impedance than free space, a portion of the wave is reflected back, as is illustrated in Fig 1.14. Also depicted in Fig 1.14

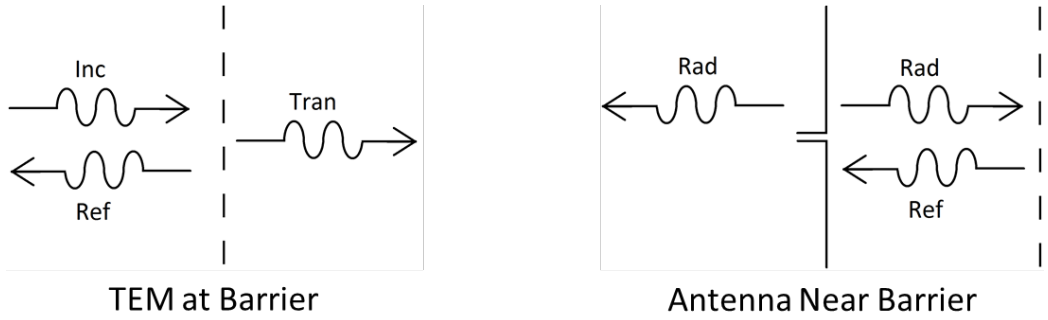

Figure 1.14: Diagram of free space (left) and antenna-generated (right) waves incident upon, and reflected from, a reflectice boundary

is an antenna near the same barrier. When the antenna radiates a wave, part of the wave will travel towards the barrier and part of the wave will travel towards the barrier. The part towards the barrier will be reflected back at the interface; and depending on the properties of the barrier, the reflected wave will have undergone some amount of phase shift. The reflected wave will then interfere, constructively or destructively, with the part of the wave that is traveling away from the barrier.

Image theory now states that if the barrier gives a reflection coefficient of magnitude 1, then the barrier can appear as a mirror for the antenna, with the image of the antenna having either in phase, for an AMC barrier, or out of phase, for a PEC barrier. This concept can be seen in fig 1.15. The appearance of a second image antenna means that if the antenna is close to an AMC barrier (less than 1/8 of a wavelength), than the antenna's propagating waves and the waves of the image of the antenna will interfere constructively and increase the gain of the antenna.

An example of an antenna that uses an AMC for gain increase can be seen in fig 1.16. In this figure, an antenna has been pulled apart to show its three layers. The first layer is a co-planar monopole, which on its own has a low directivity. Directly underneath, separated by a thin substrate, that is most commonly paper, is a periodic structure of resonators. This layer forms the top layer of the AMC. Underneath, again separated by a substrate, is the ground plane layer of the AMC. Altogether,

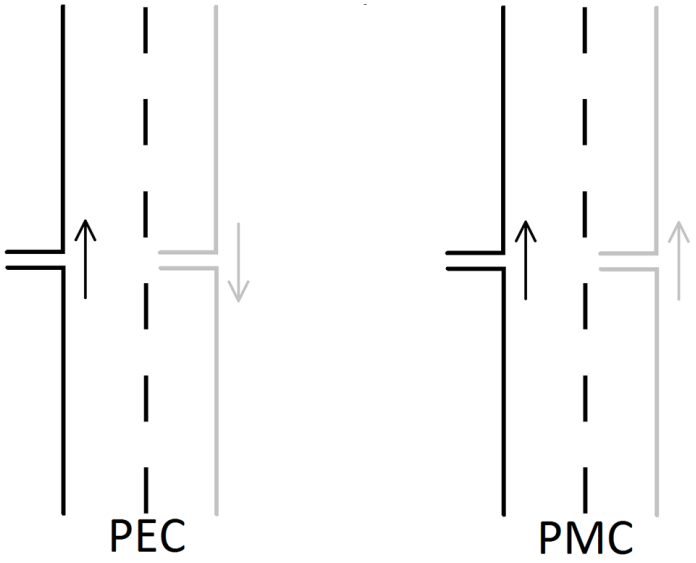

Figure 1.15: Diagram of currents induced on image of an antenna across an electricaly conductive (left) and magnetically conductive (right) boundary

this antenna appears as a monopole up against a AMC, which create reflections that constructively interfere with the monopole, thus increasing the gain.

The usage of FSS and AMCs allow for propagating waves to be directed, as is stated above. It is this ability to steer waves that makes AMCs of use in the generation of the final topology. For this reason, chapter III is dedicated to a more complete construction of theory for FSS/AMC.

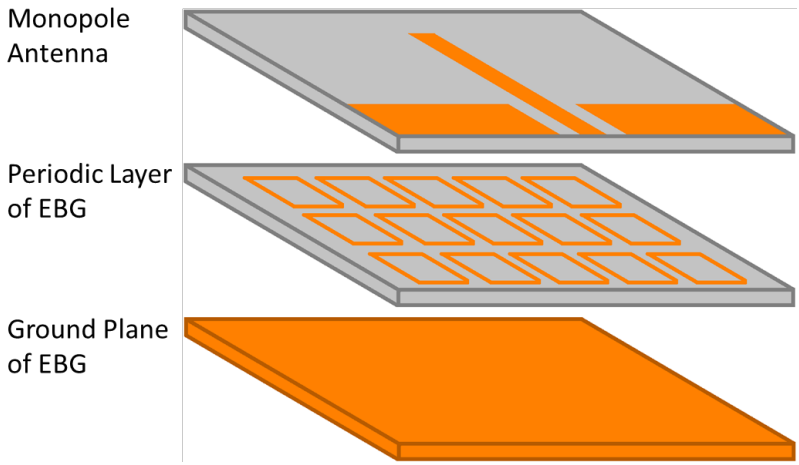

Figure 1.16: Layer-by-layer diagram of a planar monopole over an AMC

CHAPTER II

PROPOSED PROBLEM AND PLAN OF SOLUTION

Presented thus far are the basics of modern RFID technology, RFID-based sensors, antenna parameters, and artificial magnetic conductive surfaces. The purpose of this review is to build a foundation for the design of a topology for wireless sensor design. Presented herein is a proposal for the basics of that design.

The following chapter is broken into three sections. The first section covers the motivation for the proposed topology. The motivation includes both the industry demands and the constraints that must be worked around. The second section covers the fundamentals of the topology itself. The fundamentals include the mode of communication with wireless sensors, design of radiator, and sensor embedding. The third section covers a proposed proof of concept for the topology. The proof of concept includes the basic concept behind a sensor and how the data from the sensor will be transmitted back to the interrogator within the confines of the topology.

2.1 Problem

The main goals of the proposed topology are meeting an industry demand, and making the topology practical. Both can be met through the creation of a versatile and rugged topology. In the design of the embedded sensor, embedded power source and communication method, the topology is meant to lean towards the two aspects, versatility and ruggedness.

2.1.1 Embedded Sensor

In the industrial market, sensors can be used for proximity sensing for safety and security, moisture sensing for leak detection, and chemical sensing for product quality

control. In the medical field, they can be used for monitoring patient vitals, tracking the passage of visitors and patients, and logging dosage of drugs. In the military field, they can be used for detecting of ground vibrations for troop movement tracking, and detecting air born chemicals for protecting against chemical warfare.

In other words, the number of applications in that a sensor can be used, and likewise the type of sensor, is countless. To produce a wireless sensor topology that meets a large demand in the market, it is necessary to create a topology that can easily change with the desired functionality.

Therefore, the proposed topology incorporates a means of easily changing out the type of sensor that is used. It is also necessary that the implementation of a wide range of sensors does not interfere with the fundamental operation of the topology.

2.1.2 Radiator and Embedded Power Source

An antenna that can be placed anywhere in any orientation can be used for controlled location and controlled orientation applications. However, the reverse is not necessarily true. An antenna that must be properly oriented would not work in an environment where the antennas is randomly deployed. Therefore, for a versatile design, an isotropic antenna is the ideal choice for implementation in the topology.

However, the use of an isotropic antenna means that there will be a decrease in maximum read range of a wireless sensor. The decrease in maximum read range can be fixed with the use of an embedded power supply, such as a battery or power scavenging mechanism. At the same time, some applications will not need as large a read range as others. Therefore, for a versatile design, the topology, just like with the embedded sensor previously mentioned, will need to be able to operate both with and without an external power source. At the same time, the topology will need to maintain consistent operation in either case. If the existence of a power source/amplifier changes how the antenna operates, then a new antenna needs designing for each application.

2.1.3 Identifiability, Interference, and Collision Avoidance

To have reliability of communication with the tag and accuracy of transmission of data from the sensor, it is necessary to reduce the risk of interference from unwanted sources. A major source of interference is backscatter interference from the interrogator's original query signal. This backscatter interference problem is easily addressed with the use of frequency doubling in the return signal from the wireless sensor. In addition to backscatter noise reduction, frequency doubling is also easily integrated with sensors [1, 67].

The drawbacks of frequency-doubling-based RFID tags/sensors are their lack of unique identifiability and their lack of collision avoidance in the presence of other frequency-doubling tags. However, because of the benefits, such as simplicity (and thus reliability), low cost, small size, and those previously mentioned, it is worth investigating an anti-collision and identifiability method for frequency-doubling tags.

Therefore, the proposed topology attempts to create a frequency doubler with a built in collision avoidance and unique identifiability method.

2.2 Proposed Topology: Radiator and Core

As mentioned in the previous chapter, in the section on antennas and radiators, an isotropic radiator is ideal for a versatile topology. The major problem with the use of an isotropic radiator is that the addition of extra parts, such as sensors, amplifiers, and processors, can alter the performance of the radiator.

Therefore, if a truly versatile and rugged topology is to be designed then the tag needs to contain an isolated core that will not interfere with the radiation characteristics of the radiator. A solution to this issue has been by published by Cooper et al. [27].

In fig 2.1, an image of the complete topology can be seen. The image shows the three different parts. In dark grey is the core shielding. The core shielding can either

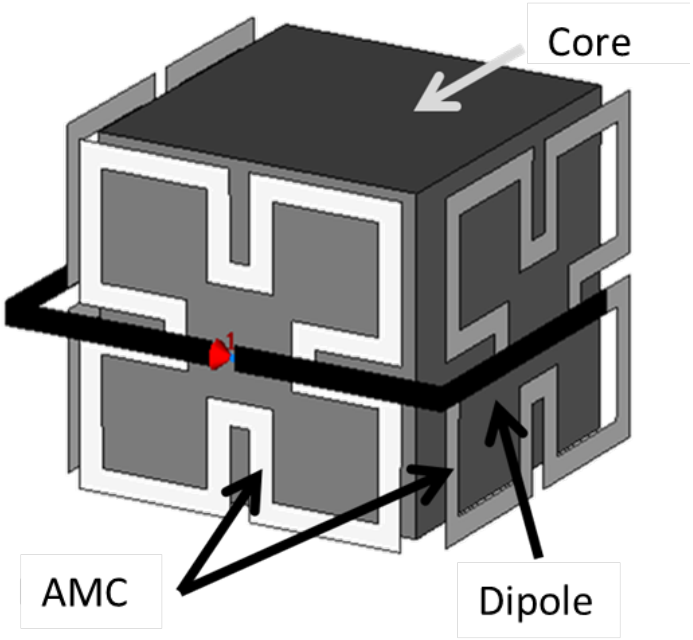

Figure 2.1: CAD drawing of complete topology

be a solid sheet of conductive material, or a sheet of babinet compliment FSS that acts as a perfect conductor at the cube's frequency of operation. In light grey is the FSS structure. The FSS structure consists of 3 unit cells wrapped around the core. These unit cells act as both reflectors and parasitic elements to isolate the core and generate the isotropic radiation pattern. In black is the excitation element for the complete radiator. Here is where any RFID components will be placed.

The normalized radiation pattern of the topology seen in fig 2.1 can be seen in fig 2.2. In fig 2.2, it can be seen that the topology achieved a front to back ratio of less than 3 dB.

The drawback to the cube design shown in fig 2.1 is rigidness of the design. Within this thesis, the full operation of this cube, and an updated version, are covered, along with a full analysis of operation and method of fabrication.

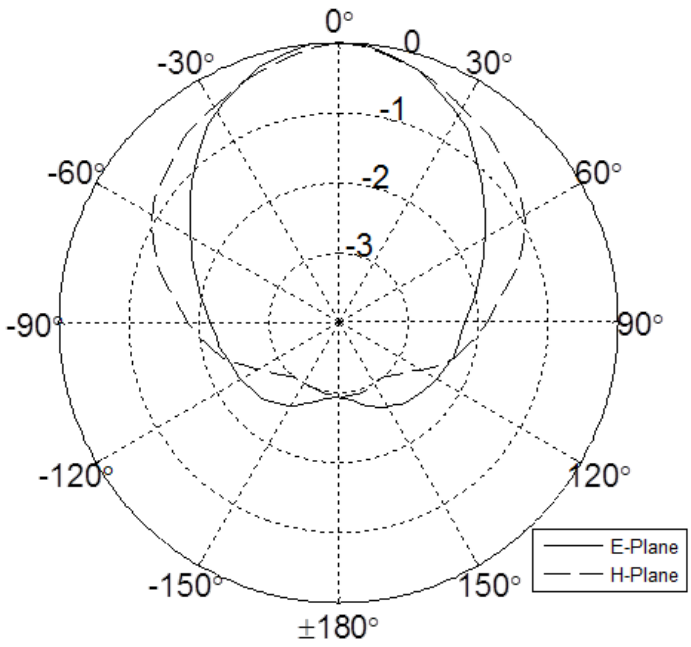

Figure 2.2: Radiation patter of the cube topology

2.3 Proposed Topology: Embedded Sensor

A novel microfluidic sensor is developed for implementing in the topology. The sensor makes use of a fabrication technique which allows for compatibility with the fabrication of the final cube topology. The sensor makes use of "smart skin" techniques for transmitting of measured data.

2.4 Proposed Topology: Communication

The fundamental operation of a frequency doubler is that it receives a sinusoidal signal and then rectifies it. The rectification of a sinusoidal signal can mean that the current flows in one direction when the voltage is positive and reverses direction when the voltage goes negative. In the case where the current reverses direction as the voltage changes is known as a full-wave rectifier. The rectification of a sinusoidal signal can also mean that the current only flows when the voltage is positive and is clipped or cut-off when the voltage is negative. The case where the current only flows

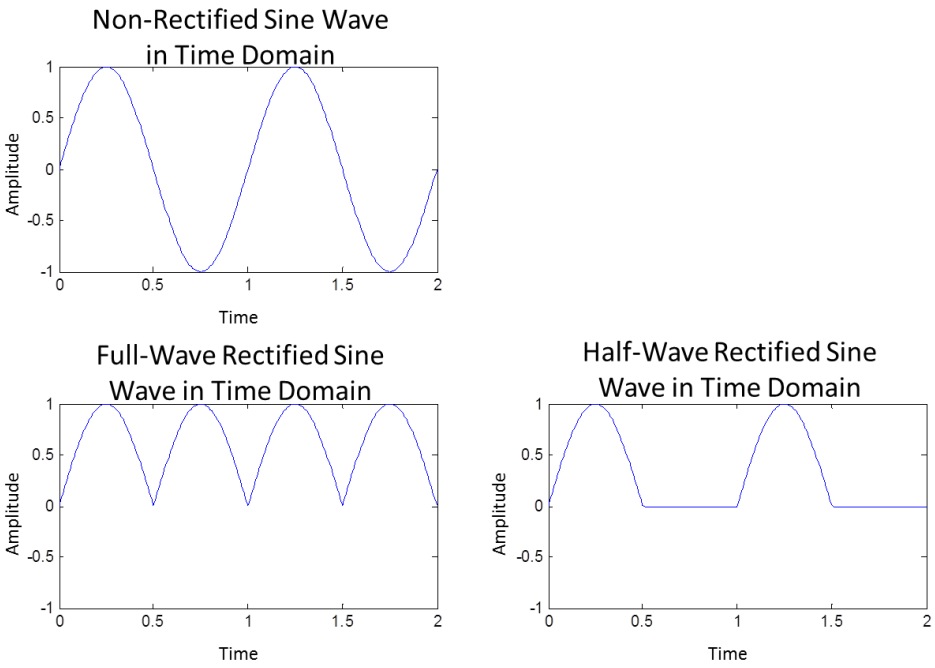

Figure 2.3: Plots of signal amplitudes in the time domain, before and after full-wave (left) and half-wave (right) rectification

under a positive voltage are knows as a half-wave rectifier.

Fig 2.3 shows three different plots. The first is a standard sine wave with a normalized period. The second and third plots show a rectified version of the sine wave in both a full-wave and half-wave rectifier, respectively.

In fig 2.4, the Fourier transform of the second and third plots from Figure 17 can be seen. In both Fourier plots, harmonics of the original sine wave can be seen. Most notably are the second harmonics, or twice the fundamental frequency of the input sinusoidal wave. In both the half-wave and full-wave rectifiers, a significant amount of power is transferred to the second harmonic.

The advantage of the full-wave rectifier, over the half-wave, can be seen in the power transferred to the second harmonic, which is 6 dB, or 4 times, greater than that of the half-wave rectifier. The advantage of the half-wave over the full-wave is in the complexity of the circuit design.

Fig 2.5 shows the circuit diagrams of both the full-wave and half-wave rectifiers.

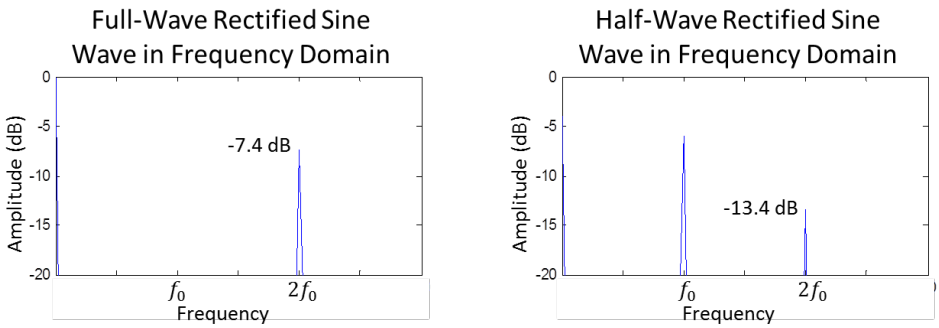

Figure 2.4: Plots of signal amplitudes in the time domain, before and after full-wave (left) and half-wave (right) rectification

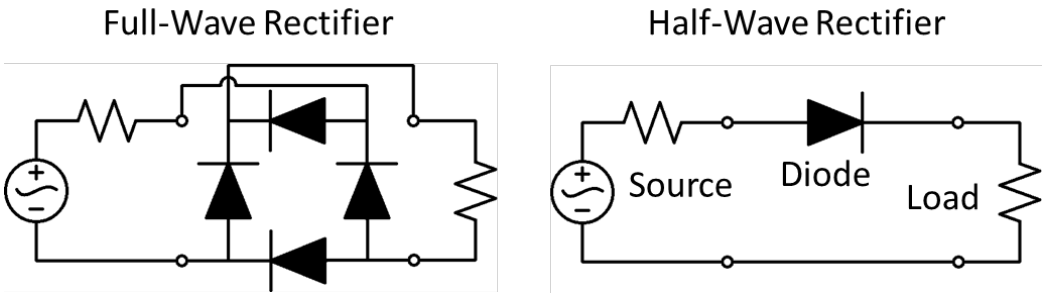

Figure 2.5: Circuit Diagrams of full-wave (left) and half-wave (right) rectifiers with source and load

As can be seen, the full-wave rectifier requires 4 times as many surface mount components.

Because of the benefits of using a frequency-doubling circuit for means of communicating with an interrogator, a frequency doubling system is developed for implementation in the topology. Since the half-wave and full-wave rectifiers have fairly even trade-offs, both will be investigated for designing and proofing the topology.

2.4.1 DC Biasing

It's the non-linear properties of the diodes, as described above, that allow for the frequency doubling to be utilized. It's also because of these nonlinear properties that the efficiency of a frequency doubler can be greatly affected with use of an external power source.

If a DC bias is placed across the rectifier, it will change how the circuit rectifies

DC Bias	Full-Wave Rectifier	Half-Wave Rectifier
0 V	-7.4 dB	-13.4 dB
+/- .1 V	-7.6 dB	-13.6 dB
+/- .5 V	-11.2 dB	-17.2 dB
+/- .95 V	-37.8 dB	-48.3 dB
+/- 1 V	-inf	-inf

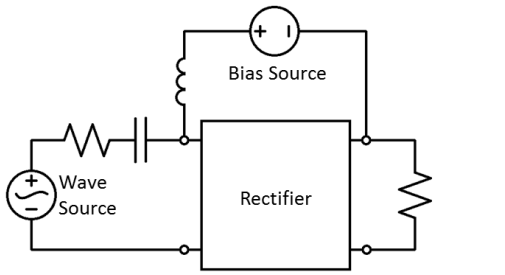

Figure 2.6: Diagram of rectifiing circuit being biased by a DC signal (right), with a table of the gain of the rectifier vs bias voltage (left)

an incoming wave. The shift in how a rectifier rectifies an incoming signal can be seen in fig 2.6, where a series of ideal case simulation are run on both a half-wave and full-wave rectifier under varying levels of biasing. For clarification, the voltages of the bias network have been normalized to the voltage of the incoming sinusoidal signal.

From the table in fig 2.6, it can be seen that any level of biasing will cause the output power of the rectifier to decrease. In fact, if the bias voltage is 95% that of the input sinusoidal wave, a drop of more than 30dB for both the half-wave and full-wave rectifiers is achieved. The drop of 30 dB means that the return signal of a frequency-doubling reflectenna can be modulated by an embedded power source within topology. The modulation of the return signal leads to two conclusions: switching and modulation.

2.4.2 Switching and Modulation

One of the advantages of an IC-based RFID tag is that it can be turned on and off using the interrogation signal. The ability to turn the tag on and off is useful in collision avoidance. If an interrogation signal turns off all but one IC, than the interrogator can directly communicate with the remaining tag without errors caused by multiple tags transmitting simultaneously.

As was shown in the previous section, using a DC source, a frequency-doubling transceiver can be attenuated by more than 30dB. If enough attenuation occurs, it

can appear as though the frequency-doubling circuit has been turned off. Therefore, if the DC source can be wirelessly controlled, an interrogator could turn on and off individual frequency-doubling tags. Just like in IC-based RFID, the ability to turn on and off individual tags could be used as a means of anti-collision.

Another benefit of IC-based, and SAW-based, RFID tags is the use of digital signals for communication. In a noisy environment, it is easier to pull out a digital signal than it is an analog signal. The interrogator need only look for whether a return signal is present or not. It does not need to know how much power is in the signal, which can be altered by noise and backscatter.

As for the frequency doubler, backscatter is not an issue because of the use of the dual frequencies. However, noise can become a problem when a frequency doubler is far away and its return signal is week. To distinguish the reflected signal from the noise, the interrogator could use the control signal for turning the doubler on and off as a modulator. The ability of the interrogator to turn on and off individual tags allows the interrogator to search through the noise for a binary modulated signal, and thus distinguish the return signal from the noise.

Finally, beyond just identification, collision avoidance and noise reduction, the modulation of the return signal from an internal power source can be used for embedded sensors. Since the modulation is analog (i.e. the attenuation is continuous from zero attenuation to infinite attenuation), a sensor could be used to control the strength of a power source that is generating the attenuation. That way, while the interrogator is identifying the tag and reducing noise via binary modulation, a sensor could be transmitting data back via analog attenuation on top of the binary.

2.4.3 Power Source

Now, for the power source to use, several options exist. One option is to have a battery or power scavenging device on board. These are not bad choices, but they

have two down sides. One is size and weight. One of the nice things about frequency doublers over resonator-based tags is that they can be very compact. Another is the simplicity and cost. A rectifier is simply one or four off the shelf components, keeping it simpler and cheaper than ICs and SAW devices. Therefore, the usage of large, heavy, complex power source should be avoided to maintain the benefits of a frequency doubler.

A rectifying circuit is primarily used for turning an AC signal into a DC signal. Therefore, instead of a large power source, the addition of a second rectifier could be used in generating the DC bias. If the second rectifier were attached to a secondary antenna, which operates at a different frequency from the primary rectifier, than an interrogator could essentially use the second frequency for turning on and off the tag.

If the secondary frequency is made to be one several discrete frequencies across a wide band, and each tag had a filter that blocked only one of those frequencies, then an interrogator could turn all but one tag off by transmitting a notched broadband signal.

Therefore, one of the main goals of the proposed research is the design of an adequate means of biasing the frequency-doubling circuit with use of a secondary frequency from an interrogator.

The full design of the frequency doubler with anti-collision can be seen in chapter IX.

CHAPTER III

THEORY OF ARTIFICIAL MAGNETIC CONDUCTORS

In order to understand the full operation of the cube topology, an understanding of frequency selective surfaces, or FSS, and artificial magnetic conductors, or AMCs, is crucial. To understand these components, first think about a planar TEM wave incident upon a boundary. Fig 3.1 depicts a boundary which is being excited by an incident, TEM wave, represented in black. As the surface is excited, two subsequent waves are induced: a reflected wave, represented in red, and a through wave, represented in blue.

The ratio of the mangitude and the difference in phase of the incident wave and the reflected wave at the boundary can be found by using the basic formula for reflection coefficient.

$$\Gamma = \frac{\eta_{Boundary} - \eta_0}{\eta_{Boundary} + \eta_0} \tag{1}$$

where $\eta_{Boundary}$ is the impedance on the surface of the boundary and η_0 is the characterisitic impedance of freespace. Note the two special case of eq (1), where $\eta_{boundary}$ is equal to 0 and when $\eta_{Boundary}$ is inf. In the first case, the reflected wave is equal in magnitude to the incident wave with a phase shift of 180°. This is equivalent to the boundary condition case in which a wave is incident upon a sheet of perfect electric conductor, or PEC. In the second case, the reflected wave is still equal in magnitude to the incident wave, but there is a 0° phase shift between the two. This is equivalent to the theoretical boundary condition case in which a wave is incident upon a perfect magnetic conductor, or PMC.

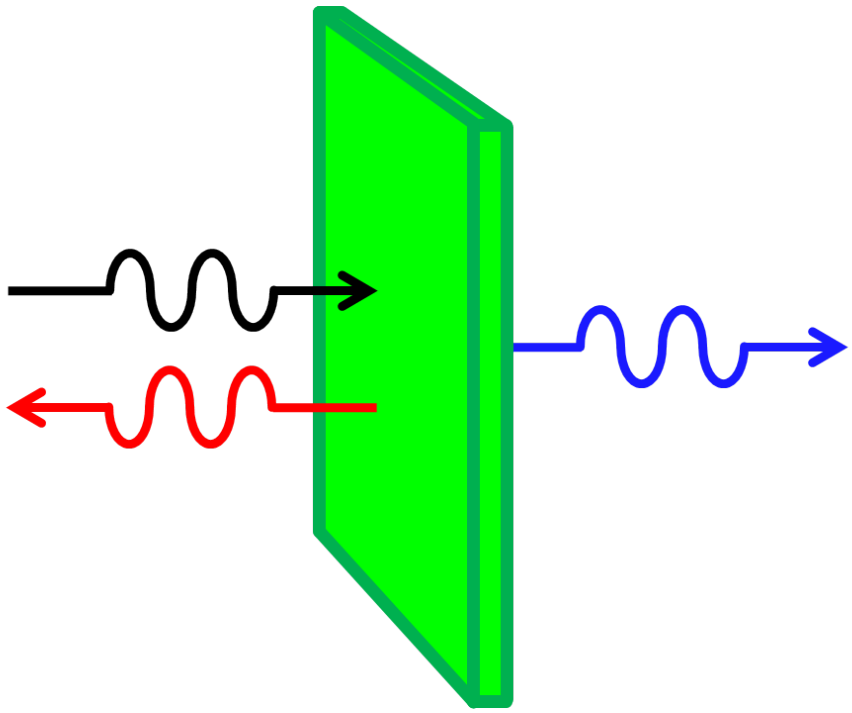

Figure 3.1: A propogating wave (black) incident upon a frequency selective surface (green), which induces a reflected wave (red) and a through wave (blue)

3.1 Antenna Proximity

The PEC and PMC boundary cases are of interest particularly when viewed in close proximity to a radiating element. For the sake of this discussion, the radiating element is considered to be a $\frac{1}{2}\lambda$ long dipole oriented in parallel to the boundary. As an omnidirectional antenna, the dipole radiates TEM waves equally in all directions about an orthogonal plane, as can be seen in fig 3.2. Some of these waves travel towards the boundary and induce a reflected wave, which travels back towards the antenna.

For simplicity, without losing generality, only waves which travel along the orthogonal plane directly towards, and directly away form the boundary are considered. The reflected waves, induced by the waves propogating towards the boundary, propagate back towards the antenna and interfere with the waves originally propagating away from the boundary. Due to the linearity of EM waves in free-space, this interaction

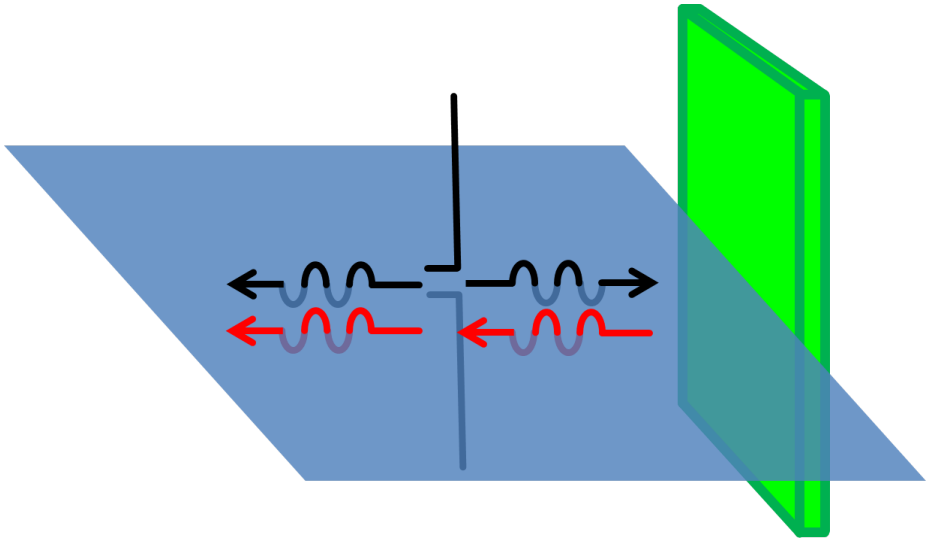

Figure 3.2: A dipole antenna radiating outward (black) along an orthogonal plane (blue) in close proximity to a surface (green), which generates phase shifted reflected waves (red)

can be described by

$$\begin{aligned} &\mid Wave_{comb} \mid *cos(\omega t - kx + \theta) \\ &\qquad = \mid Wave_{rad} \mid *cos(\omega t - kx) + \mid Wave_{ref} \mid *cos(\omega t - kx + 2kd_0 + \theta_\Gamma) \end{aligned} \tag{2}$$

where $Wave_{comb}$ is the overlay of the wave radiated away from the boundary, $Wave_{rad}$, and the wave reflected off the boundary, $Wave_{ref}$; θ_Γ is the phase shift of the reflection at the boundary; d_0 is the distance between the antenna and the boundary; x is the distance away from the antenna in the direction away form the boundary; and k is the propogation constant give by

$$k = \frac{2\pi}{\lambda_0} \tag{3}$$

where λ_0 is the free space wavelength at the frequency of operation. If it is assumed that the antenna is close to the boundary, and the boundary has a magnitude reflection coefficient of 1, then it can be assumed that $\mid Wave_{rad} \mid \approx \mid Wave_{ref} \mid$.

T1 1: Phase of reflection and optimal distance of seperation for an antenna and reflecting boundary

Boundary	Phase of Reflection (θ_{Gamma})	Optimal Seperation (d_0)
PEC	180° (π rads)	$(.5 * n + .25)\lambda$
PMC	0° (0 rads)	$.5 * n\lambda$

Accounting for this approximation, (2) becomes

$$Wave_{comb} =\mid 2 * Wave_{rad} * cos^2(\frac{2kd_0 + \theta_\Gamma}{2}) \mid *cos(\omega t - kx) \tag{4}$$

From (4), it is easily seen that the magnitude of a wave propagating away from an antenna in close proximity to a boundary is based upon the distance between the antenna and the boundary, and the phase of reflection at the boundary. In order to assure the maximum magnitude of $Wave_{comb}$, the term inside the cos^2 must be equal to $n * 180°$ for n=0,1,2..., or

$$d_0 = \frac{\theta_\Gamma + n * 2\pi}{2k} = \frac{\lambda}{2}(\frac{\theta_\Gamma}{2\pi} + n) \tag{5}$$

Going back to the two cases of a PEC and PMC boundary, table 1 shows the angle of reflection at the boundary. Using this angle of reflection, and (5), table 1 also shows the distance an antenna should be from a boundary in order to achieve the largest magnitude in radiated waves.

From this analysis, it can be seen that backing an antenna with a PMC or PEC boundary can increase the gain of the antenna by 3dB! Though PECs and PMCs yield the same increase in gain for close proximity antennas, PMC holds a distinct advantage in that an antenna can be placed in very close proximity, while a PEC requires $.25\lambda$ distance between antenna and boundary for increased gain, and at least $.125\lambda$ before there is not a decrease in signal strength. Although PMC holds this advantage, there does not exist a material which exists as a PMC. Therefore, an

artificial magnetic conductor, or AMC, is necessary.

3.2 FSS

The understanding of a frequency selective surface, or FSS, is critical to understanding the operation of basic AMCs. In order to achieve this, first consider a loaded dipole in free space. This dipole is excited by a TEM wave, in which the E-field is parallel to the antenna. When the E-field strikes the antenna, it induces a voltage on the terminals of the antenna. The voltage excites the load of the antenna, which then reflects back part of the exciting voltage per eq (1). This back reflected voltage is re-radiated with a phase shift in accordance with the phase shift at the load. The re-radiated signal travels in all direction around the antenna, including in-line with the original signal and in the reverse direction of the original signal as depicted in fig 3(a).

The "Incident" wave is the wave exciting the antenna. Although, because of the finite size of the dipole, some of the signal passes by, unaffected, which is depicted by the "Pass" wave. The exciting wave induces a voltage, "V", which is partially reflected and re-radiated. Some of the re-radiated energy, "Reverse", is sent back towards the source of the "incident" wave, while some of the re-radiated energy, "forward", is sent in the same direction of the "Pass" wave. If the load of the antenna, like the boundary conditions stated above, had an impedance of 0 Ω, then the re-radiated waves would have a 180° phase difference from the "Incident" wave. The "Forward" wave would destructively interfere with the "Pass" wave. In effect, the "Pass" will suffer very little attenuation from the interference, as is depicted in fig 3(b), very little of the energy is transmitted in that direction, and most energy is scattered in the omni-directional pattern of the dipole.

Now, so far has been the idea of a single dipole being exctied. If the dipole was extended from a single element to an infinite, 2D array, it would become an infinite

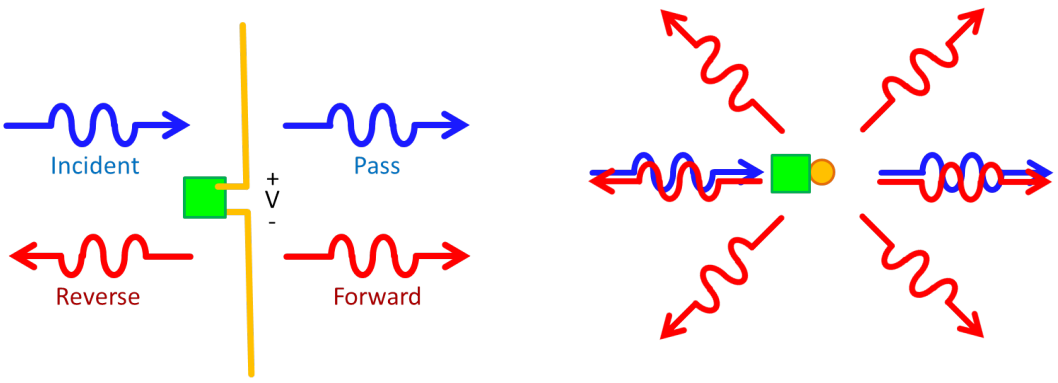

Figure 3.3: Figure of an excitation signal inducing a voltage on an antenna's load, and the re-radiation of the reflected portion of the signal from a (a)side view and a (b)top view

directivity, antenna array. If a wave of perfect incidence excited the surface of the 2D array, again, there would be an "Incident", "Pass", "Reverse", and "Forward" wave. In this case, due to no energy being radiated omni-directional, due to the extreme directivity of the array, the "Forward" wave could completely interfere with the "Pass" wave, and all the energy would be sent in the "Reverse" direction with a 180° phase shift. In essence, the array would appear as a perfect electric conductor.

Now, to point, it is assumed that there is a perfectly incident wave operating at a single frequency with which the antenna is .5λ. If frequency is varied, the phase of the re-radaited waves will shift, and there will no longer exist complete destructive interference between the "Pass" wave and the "Forward" wave. As such, less energy will be reflected back in the "Reverse" wave. It is this property of reflecting differently at different frequencies which yields the name of frequency selective surface.

Before moving into AMCs, one last topic that must be covered is what happens when the incident wave is not perfectly incident, i.e. it excites the array at an oblique angle. For this, picture the array in fig 4(a), where there is a 2D array of dipoles being excited by a plane wave at an off angle. When the plane wave hits the array, instead

of exciting all the elements simultaneously, the plane wave will excite the elements at a time delay between each dipole, as seen in fig 4(b). The time delay between elements translates into a shift in phase, where $\theta = \omega t$.

This difference in phase of the excited elements of the array makes the 2D array appear as phased array. Therefore, instead of having a radiation patter which is normal to the array, it has a radiation pattern similar to that in fig 5(a). When the plane wave hits the array, two waves are induced by the array, as seen in fig 3.4. The forward wave still cancels with the pass wave, but the reverse wave now travels in a mirrored direction from the pass wave. From analysis of the excited phases, and resulting induced waves, it can be easily calculated that the angle of incidence is supplimentary to the angle of induced propagation. The wave now appears as though it has struck an electrically conductive surface. Therefore, the array can be treated as a sheet of conductive material at any angle of incidence, but only at the central frequency of operation.

3.3 AMC

When placed in close proximity to a sheet of a highly conductive material, a dipole antenna will be de-tuned. More precisely, the impedance on the dipole's terminals will approach $-j\infty\Omega$ as the dipole approaches the sheet. This is especially true for a highly directive array of dipoles which are brought in close proximity to the sheet. This shift from short circuit loading to near infinite loading causes a 180° shift in the re-radiated waves from the infinite array in free space case, thus yielding a 0° phase shift in re-radiated waves from the initial incident wave.

Fig. 6(a) shows an incident wave hitting an array backed by a highly conductive surface and the resulting re-radiated waves. Due to the 0° phase shift, the pass wave and forward wave are in phase with each other. Due to the conductive surface behind the array, the pass and forward waves are reflected back in the direction of the reverse

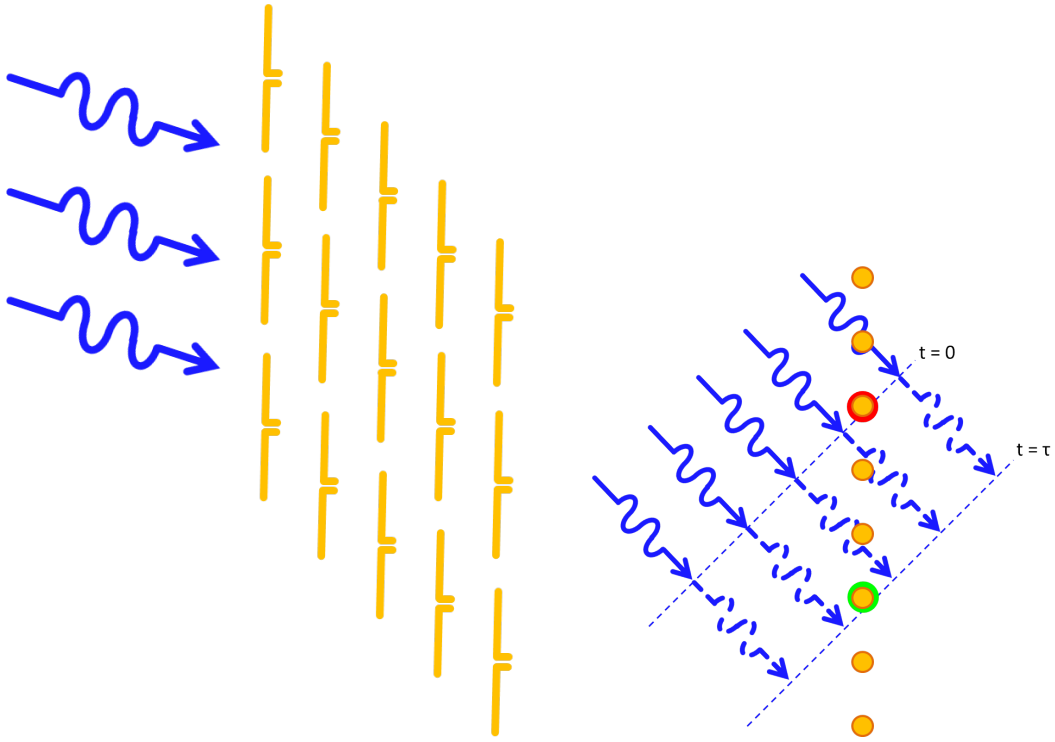

(a) (b)

Figure 3.4: Depiction of an excitation signal, obliquely incident upon (a)an array of antennas, (b)exciting different antennas in the array at time interverals, τ, as the phase plane passes

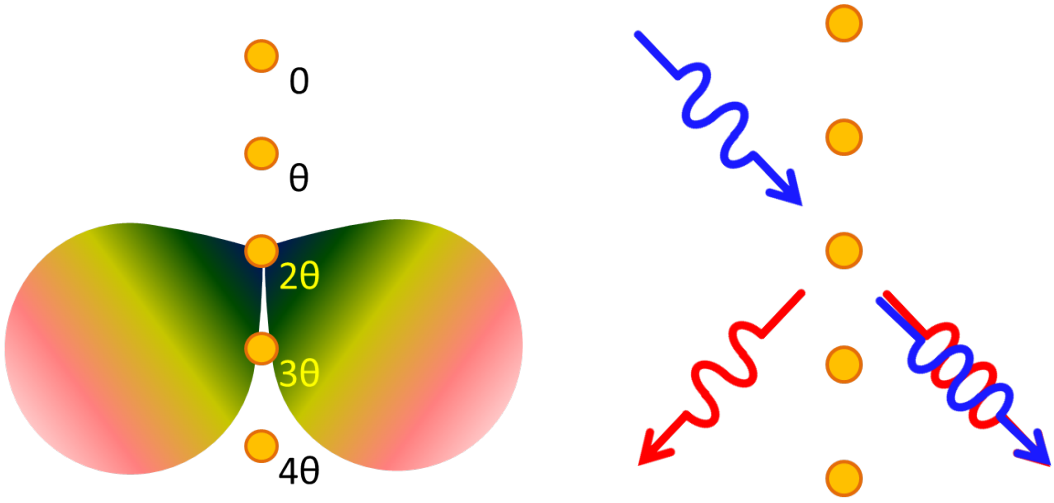

(a) (b)

Figure 3.5: Figure of an array of dipoles excited in a phased manner (a)producing a phased array radiation pattern, (b)re-radiating a signal's energy in the directions of peak array directivity

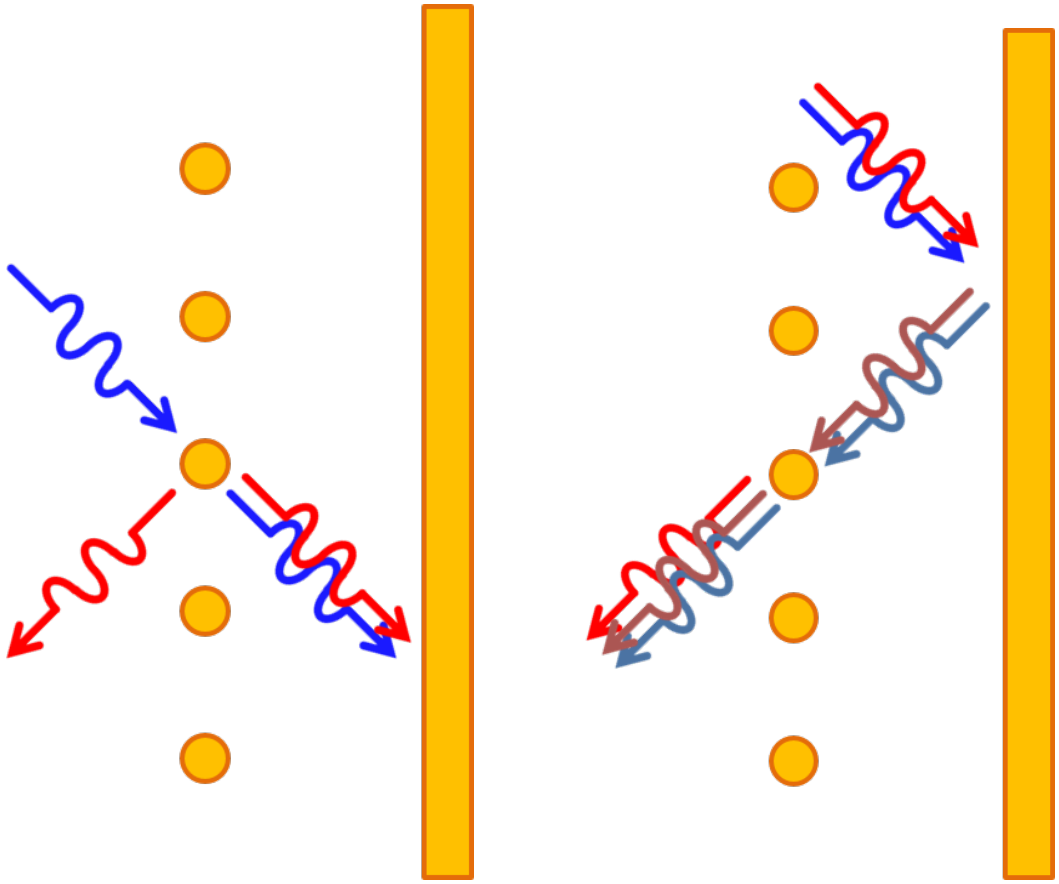

Figure 3.6: Figure of (a)an FSS, backed by a highly conductive surface, being excited by an (red) incident wave with (blue) re-radiated waves from the elements, and (b) the resulting (pale red) incident wave and (pale blue) re-radiated forward wave after reflecting off the highly conductive surface

wave. Due to the boundary conditions of a conductive surface, the reflected waves are now 180° out of phase with the reverse wave, as can be seen in 6(b). This out of phase causes destructive interference and leads to a single wave with the same magnitude of the original incident wave. Because two of the interfering waves were in phase, and one was out of phase, the resulting reflected wave also has the same phase as the original incident wave.

By comparing the results of an infinite array backed by a conductor with the boundary conditions covered earlier, it can be seen that the FSS now appears as a

magnetic conductor at the frequency of operation. Due to the frequency dependence of the material, this type of surface is known as an artificial magnetic conductor.

3.4 EBG

In all analysis in this chapter, it has been assumed that the AMCs are excited by TEM wave with an E-field normal to the surface. From this, it can be assumed, that the surface will act in the same manner whenever they are acted upon by a TE wave. Due to the high impedance nature of an AMC (derived from the boundary conditions) TE modes, such as surface waves, would be unable to propagate along the surface of an AMC at the frequency of operation. However, these structures do not hinder the propagation of TM surface waves.

Electronic bandgap materials, or EBGs, are surface which act as high impedance surfaces to TEM waves, and which have a frequency band of operation where neither TE nor TM surface waves can propagate. The design and operation of EBGs are covered in depth by Sievenpieper et al [73, 74]. The ability of an EBG to suppress surface waves makes them very useful in the increasing the directivity and efficiency of antennas [34, 74] beyond the theoretical 3 dB presented by electric and magnetic conductors. Their inherent properties also make them invaluable in implementing leaky resonant cavity antennas [30].

The downside of EBGs is the requirement of a via in the design. For the chosen design of the final topology, vias are not accessible, and therefore, AMCs are used instead.

3.5 conclusion

In the following chapter, the practical operation of an FSS will be covered and applied to a free space beam splitter. It is this early work with FSS, their design, and their fabrication, which drove much of the theory used in the cube topology. Chapters 5 and 6 will delve into the application of AMC in creating the full cube topology,

making use of the null phase shift property of an AMC, and the property of reflecting all incident waves, and thus isolating the front of the surface from the back.

CHAPTER IV

FSS APPLICATIONS

In the pursuit of generating the cube topology, which utilizes a conformal, via-less AMC structure, a full understanding of FSS structures is necessary. Herein is early work which covers the operation of an FSS both on and away from the center frequency of operation. This chapter, and the corresponding fabrication section found in chapter VII, are excerpts from a publication by Cooper et al [25].

This chapter introduces the first beam splitter that acts on free-space, planar, microwave frequency waves below 80 GHz. The design utilizes a frequency-selective surface (FSS) operating away from its normal frequency of operation. The FSS is constructed from an array of scalable printed patterns which allows for the tunability of the FSS to any frequency which the fabrication method will allow. The basic operation of an FSS, the reasoning behind selecting the chosen unit element and fabrication, and a comparison of simulated and measured results are discussed in detail. An inkjet printed prototype on a glossy paper substrate utilizing silver nano particles verifies the easy and scalable low-cost fabrication capability of the proposed topology.

4.1 Introduction: Beam Splitters

A beam splitter, which is traditionally used in optics, takes a propagating electromagnetic wave and splits it into multiple waves. This splitting may be a polarizing split, which separates the wave into two waves with orthogonal polarizations, like polarized lenses; frequency split, which splits the wave by frequency spectrum, such as a prism; or, amplitude split, which splits the wave into multiple waves with a set power ratio, such as a semi-reflective mirror. A free-space beam splitter acts on a TEM wave

traveling in open air or a vacuum. Free-space, amplitude beam splitters have been around for many years [3, 28], and are commonly used in interferometers and laser output-power trackers, but have mostly been confined to optical frequencies. This is due to beam splitters being based on total internal refraction in between two medium or on semi-transparent mirrors. The first relies on the space between the medium being dependant on wavelength. The second relies on the skin depth of the metal in the mirror being very small. Both of which become very impractical for mm wave and lower frequencies. However, due to recent advances in wireless power transfer and ad-hoc RF networks, it is desired that similar devices for lower frequencies be developed.

A free-space amplitude beam splitter for 80 to 110 GHz [84] has been developed. This beam splitter is based on a meta-material constructed by placing a metal grating on a dielectric slab, where the slab depth has a linear ratio with the wavelength of the desired frequency of operation. This increases the cost of fabrication, decreases the ease of fabrication, and leads the device to become bulky at lower frequencies. A spatial beam splitter has been developed for sub-millimeter wave applications (7GHz in this applications, but scalable to a wider range) [43]. However, this design requires a single transmission line feed and does not split free-space waves. Like [84], it also utilizes dielectric slab based meta-material, which adds cost and difficulty in fabrication.

In this chapter, a polarization-independent, free-space, amplitude beam splitter is presented which operates in the sub-millimeter wave frequency range. It is based on printed frequency selective surfaces, which are a cheaply fabricated and easily scaled meta-material. It acts on a single plane wave, which it splits into two parts with pointing vectors 90° apart, as shown in fig 4.1. Although this paper will cover the case where it is desired to split the wave into two equal parts, as will be shown, a wide range of split ratios can be achieved by adjusting the dimensions of the FSS unit

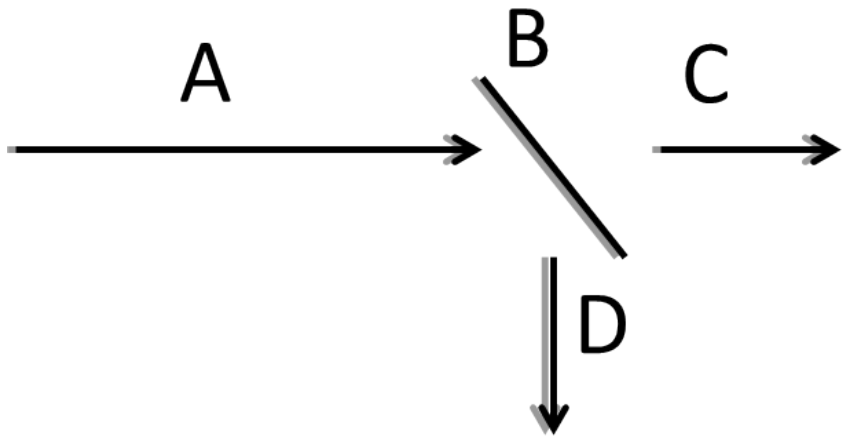

Figure 4.1: Proposed Free-Space Power Splitter A power splitter (B) takes an incoming incident wave (A) and splits it into two parts: a through transmitted signal (C) and a reference signal (D).

cell.

4.1.1 FSS

Frequency Selective Surfaces, which are a type of meta-materials, have been studied for a long time due to their many properties. Their frequency selectivity makes them useful in multi-band reflector antennas [61]. Due to the fact that for carefully chosen dimensions and spacing, and addition of a ground plane, they can act as magnetically conductive surfaces which are used as reflectors for dipoles and other compact antennas [36] to increase directivity.

Frequency selective surfaces are normally composed of some type of periodic structure. This could be a 2-D array of dipoles [60], an array of loops linked together with lumped elements [6], stacked arrays of dielectric rods [8], etc. In any configuration, they have the unique property that at a single frequency they act as an infinite impedance surface to plane waves, and at other frequencies they act as transparent surfaces [36]. This means that there exists a point, somewhere between the pass and stop band, that the FSS allows half the power to pass through and reflects the other

half.

The 2-D FSS has been shown to be fully operational when working at a 45^{circ} incidence, as long as the elements and their spacing are small [46]. If the FSS is illuminated at the half-power frequency point, a frequency located between the point of transparency and full reflection, at an angle of incidence 45, then the result would be what is shown, and desired, in figured 1.

The following section covers how the FSS structure is chosen. Section 3 covers how the measurements are setup and made. Section 4 covers the results and creates a clear definition for how to measure performance of sub millimeter wave frequency beam splitters. Section 5 brings together the results and discusses possible applications for the beam splitter.

4.2 FSS Unit Cell Design

For ease of fabrication and ease of scaling, the FSS was designed using a single printable layer of a 2-D array of unit cells. The cells were chosen on the criteria of the surface being able to operate at 45 of incidence to the transmitted signal, and needing to be non-polarized to make the surface operate the same independent of polarization of incident wave. According to [61], in order to avoid grating issues, which causes shifts in the center frequency of the surface, the unit cells should be electrically small, on the order of 1/8 of a wavelength. Most unit cells, such as the tripole, are close to 1/2 wavelength in size. Therefore a convolutable shape, or shape which can be made to minimize area while maintaining a large diameter, was chosen [60]. The Hilbert curve allows itself to be made exceptionally small, but it is polarized. Therefore, the convoluted square, which can be seen in the left of fig 4.2, are chosen for this design since it features the smallest non-polarized shape.

The total number of cells in the 2-D array were chosen so that at 45° of incidence, the cross sectional area of the FSS would be roughly the size of the plane-wave front.

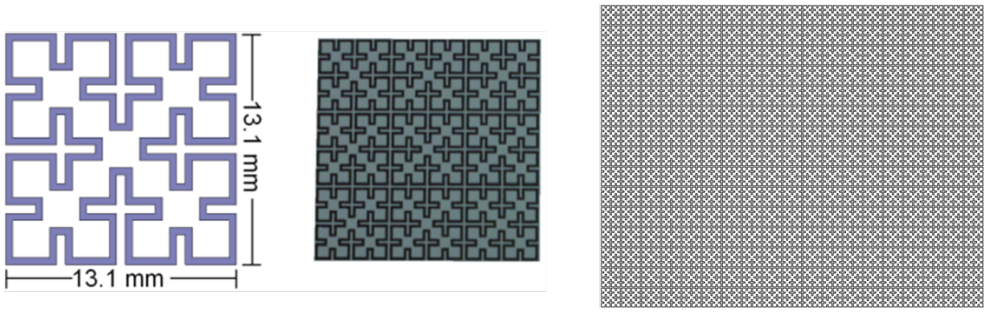

Figure 4.2: 3rd Generation Convoluted Squares Used for the FSS (Left) A bitmap image of the unit cell which was used for simulation and printing, (center) a picture of a 3x3 array of the cells after printing, and (right) a full schematic of one of the sheets. The cells are spaced .5 mm apart.

4.3 Measurement Setup

A subset of the cells after printing and curing can be seen in the center of fig. 4.2. The right most image of the same figures depicts a full sheet of the cells. As mentioned above, the full fabrication is outlined in chapter VII.

Fig 4.3 shows the setup used for testing the FSS. A horn antenna with a gain of 25dBi was used to illuminate the FSS and two receiving monopole antennas were used to measure the power levels of the split signals. The horn antenna was chosen so that the FSS could be kept out of the near field of the antenna while still acting as a complete barrier between the transmit and receive antennas. The horn and monopoles were chosen such that they each had a bandwidth wide enough to cover the desired frequency band of the FSS. For measurement, the horn was rotated around the FSS, keeping an equal distance. Both receiving antennas were also placed at equal distance from the surface and 90 apart. The value of transmission for both the through transmission (line c in fig 4.1), and the value of reflection (line d in fig 4.1) where normalized to the value of direct radiation from the Horn to the monopoles.

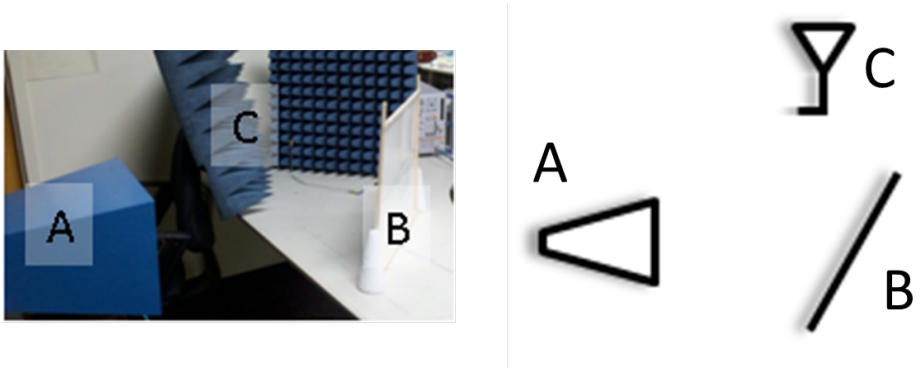

Figure 4.3: Measurement Setup for the Power Splitter A Horn antenna (A) illuminates a monopole antenna (C), first directly, then through an angle FSS (B), then at a 90 angle reflected off the FSS.

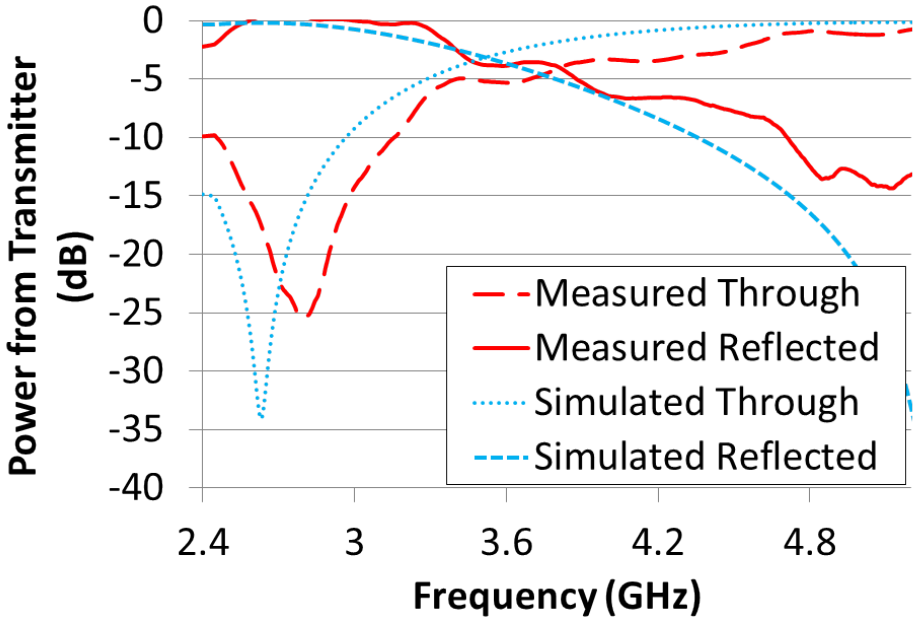

Figure 4.4: Power Levels Received After Passing Through the Power Splitter This plot shows a comparison between the power sent through the FSS and the power reflected off of the FSS.

4.4 Results

Fig 4.4 shows a comparison between the simulated results, which were made using Ansoft HFSS, and the measured results. The through and reflected (reference) are defined in fig 4.1. As can be seen, the surface acts as a good FSS and does a good job of splitting the wave. The simulated reflected and through cross at -3.1dB at 3.5GHz. The measured through and reflected cross at -4dB at 3.8GHz. The loss of 1dB and the frequency shift could be the result of misalignment between the different printed sheets, effects of the wooden dowels used to hold the surface steady, the effects of the adhesive used, or bends in the surface. These could be fixed by attaching the FSS to a porous Styrofoam sheet, which is cheap and has a dielectric constant very close to air, and by printing the FSS on a single continuous sheet with a larger inkjet printer.

4.4.1 Operational Bandwidth

Watanabe et. all [84] defined the operational bandwidth to be when the through and reflected signals were within 0.8 dB of each. This definition was chosen arbitrarily based upon how that specific beam splitter operated. In following suit, a new definition is chosen in this paper. Here, the bandwidth is chosen to be the range in which the ratio between reflected and through signal varies between 2:1 and 1:2, or 3dB to -3dB. As can be seen in fig 4.5, the simulated bandwidth comes out to be 500MHz, or 14% Bandwidth. As is to be expected from the losses observed in the system, the measured bandwidth is larger at 620 MHz, or 16%.

4.4.2 Splitting Ratios

Thus far, this paper focuses on the design of an amplitude beam splitter which equally splits a beam in two directions. However, it is often desired for the split to be uneven, such as in a laser output power tracker. In this situations, it is desired that most of the power be transmitted in a single direction and very little be used for tracking purposes. The presented beam splitter has the ability to split at ratios other than

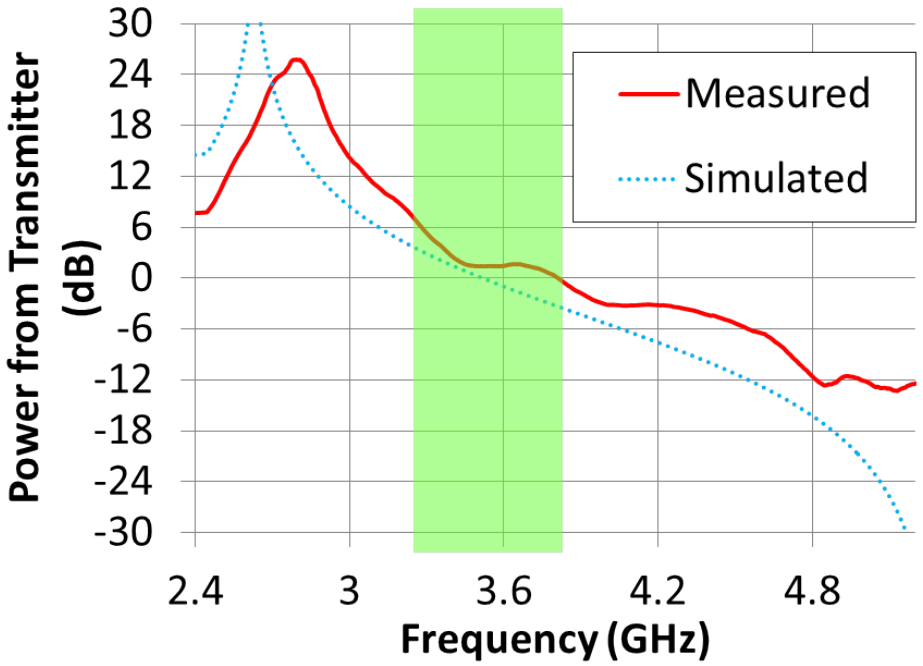

Figure 4.5: Power Ratio Between Transmitted and Reflected Power This plot show the power ratios between the power sent through the FSS and the power reflected off of the FSS.

1:1. As can be seen in fig 4.5, a split ratio can be achieved from 0dB (1:1) to 25dB (316:1) with the measured FSS. From the simulation, it appears that the theoretical limit to the split ratio is much higher.

4.5 Conclusion

Hereto has been presented the first non-polarizing, amplitude beam splitter without surface mount components which operates at low microwave frequencies with performance verified by an inkjet printed prototype on a glossy paper substrate designed around 3GHz. It has been shown, through simulation and measurement, that, over a narrow bandwidth, this beam splitter can split an incident beam into two equal parts traveling in directions 90 apart with less than 1dB of attenuation. It has also been shown that a splitting ratio other than 1:1 can be achieved by scaling the unit elements of the material.

As seen in [46], a wide range of angles for the reflected beam can be achieved. This

means that this device could be implemented in ad-hoc wireless networks, where it is necessary to disperse a signal in multiple directions in order to illuminate multiple receivers. Utilizing the various splitting ratios discussed in section IV-C, the beam splitter could also be used in wireless power transfer applications as part of a power tracker to measure how much power is being transmitted from a source. Due to the strong frequency response, the beam splitter could be used in spectrum analysis, where multiple surfaces can be used to direct a signal towards multiple sensors.

CHAPTER V

FIRST CUBE: PAPER BASED

Now that the basic operation of an FSS, which is closely tied to and necessary for the understanding of AMCs, the FSS structures will be utilized in the design of an AMC based device. This chapter presents an early design of the cube topology. It shows the first use of a conformal AMC, and lays the ground for the operation of the final cube topology design. This chapter, along with the corresponding fabrication section in chapter VII, consists of excerpts from [27].

This chapter presents a novel topology of isotropically radiating smart cubes for use in wireless sensors. The novelty of this antenna is the use of 3D conformal frequency selective surfaces which are used both for creating the desired radiation pattern and for creating a core which is electrically isolated from the antenna at the frequency of operation. The core allows for an embedded power source, processor, amplifier, and/or secondary antenna without interfering with the operation of the radiator. As demand for wireless sensors continues to grow, this device will allow for the implementation of sensors in a wider range of applications including autonomous smart skins, biosensing, and RFID-enabled sensors. The prototype is printed on glossy paper using a conductive ink, which gives it the potential for low cost production, allowing it to be used in a variety of applications requiring large numbers of sensing nodes, while meeting enhanced data processing, security or autonomy requirements.

5.1 Introduction

Wireless sensors allow for variety of different applications including the sensing of moisture [32], temperature [68], or gases such as ethanol, acetone, nitrogen, etc [72,85].

This makes it invaluable in many fields including industrial, medical and military. However, large disbursements of wireless sensors are held back by three major concerns. First is the orientation of the sensor transponder with respect to a reader. If the reader is facing a null in the transponder's field of radiation then the two will be unable to communicate. The second concern is the maximum read range between interrogator and transponder. In order to guarantee that the two can communicate at a large distance, it is necessary to use an active tag. This includes the use of either a battery or energy scavenging device [82]; both of which can have a large size and potential to interfere with the radiator. The third concern is cost, since it may be desired to deploy large numbers of these sensors.

Therefore, in the pursuit of expanding the usage of wireless sensors, presented herein is a near-isotropic radiating RFID based transponder, constructed in a low cost manner, with an isolated core for embedding sensors and/or power source. Within this chapter, the background research, which led the proposed design, is presented. Next is presented the design and simulation data of said proposed design. This is followed by verification through measurement. Finally, conclusions are presented based upon the design process and measurement data.

The fabrication of this cube is presented in chapter VII.

5.2 Background Data

5.2.1 RFID Sensors

The two responsibilities of wireless sensors are that they are able to detect some aspect of their environment and that they be able to communicate back to an observer or interrogator what is being detected. It is the latter which makes RFID a great solution. Since the root function of RFID is to transmit encoded data back to an interrogator, it should have the ability to transmit encoded data taken from a sensor.

Measurement data can be collected and encoded using a discrete sensor and processor. It can also be encoded though the parameters of communication with the tag itself. This can be done by allowing the sensor to shift the operating parameters of the tag [32,67], or the sensor can be embedded in the antenna and shift the operation of the radiator [85,86]. The latter of the two is often referred to as Smart Skin sensing. The encoding can also be done by using the sensor as a load on the tag, where a shift in the load translates to a shift in the retransmitted signal [72,77]. When these sensing methods are combined with an RFID tag, the sensed data can be transmitted to and processed by an interrogator.

Through these ends, RFID based sensors have been used in a wide range of applications as mentioned earlier. Because RFID based sensors are capable of versatile sensing, there is great demand to continue to investigate new designs and applications.

5.2.2 Isotropic Radiator

Perfect isotropic radiating antennas are a theoretical reference for how an antenna radiates energy. They are characterized by their ability to radiate an equal amount of energy in all directions. By the basic operation of an antenna, this means that they receive power equally from any direction. This makes them ideal candidates for use in RFID systems, where the orientation of a tag is random.

Perfect isotropic antennas, which have a 0dB variance in relative power between any two directions, are mathematically impossible without the use of magnetic monopoles. However, several semi-isotropic antennas have been created. These have included a dipole coupled with a resonator printed on kapton yielding less than 9dB variances [47], two crossed dipoles yielding less than 4dB variance [59] and four phased monopoles in a circle yielding less than 8dB variance [42].

5.2.3 Artificial Magnetic Conductors

FSS are normally composed of some type of periodic, resonating structure. This could be a 2-D array of dipoles [36], an array of loops linked together with lumped elements [6], stacked arrays of dielectric rods [8], etc. The AMC is different from the FSS in that it contains a ground plane underneath the structure and may contain vias [73].

In order to achieve both an isotropic radiating pattern and an electromagnetically isolated core which will not interfere with said radiation pattern (criteria one and two to be discussed in section III), AMC structures are implemented.

5.3 Design and Simulation

The design of the cube includes the meeting of two major criteria and one minor criterion. The first is that the cube be an isotropic radiator. The second is that the cube contains a portion, preferably in the middle, which can contain a wide range of materials without interfering with the first criterion. The third criterion is that the input impedance on the port of the cube be close to the input impedance of an RFID tag in order to achieve a wider bandwidth and longer read range.

5.3.1 Design

For the second criterion, a cube with PEC boundaries was chosen. This PEC could be a solid sheet of copper, or another good conductor, or it could be an FSS babinet compliment structure with an operating frequency away from that of the cube. The use of PEC boundaries allows for complete isolation at the cube's frequency of operation. The use of an FSS babinet compliment would allow for wireless transmission with a secondary radiator contained within while still acting as a broadband PEC. For the purpose of simplicity in the proof of concept, a copper plated core was used.

For the radiator, a simple dipole was used. Since the core is a good conductor,

when a dipole is placed near it, the dipole is severely detuned and non-functional as a radiator. Therefore, an FSS is placed on three sides of the core with a separation of 5 mm. The Antenna is placed 5 mm above the FSS. The FSS now acts as an artificial magnetic conductor, AMC, due to the core underneath, constructively interfering with the antenna, as well as acting as parasitic resonators, giving the antenna a less directional radiation pattern.

The FSS unit cell chosen is a second generation convoluted square. This is chosen because this structure is not polarized, unlike a split ring resonator. It is also chosen since it is easily miniaturized. A second generation is chosen due to being significantly smaller than a first generation while still having a wider bandwidth than a third generation.

At the operational frequency of 900 MHz, the square has a size of 56 mm x 56 mm. As such, the cube has dimensions of 56 mm x 56 mm x 56 mm. The antenna length was chosen to be that of a free-space dipole, 167 mm. The complete design of the cube, including core, FSS/AMC and antenna can be seen in fig 5.1.

5.3.2 Simulation

Simulation and optimization were done using CST Microwave Studio. Frequency domain analysis was done for optimizing the dimensions of the FSS/AMC. Transient Analysis was done for calculating the input impedance and radiation pattern of the cube. A plot of the input impedance can be seen in fig 5.2. The radiation pattern is covered in the results.

From the impedance plots, it can be seen that the effects of the cube have shifted the input impedance of the dipole antenna to a low real part and a large, positive imaginary part.

In order to calculate the magnitude reflection coefficient between the complex impedance of the antenna and the complex impedance of the RFID chip, Kurakowa's

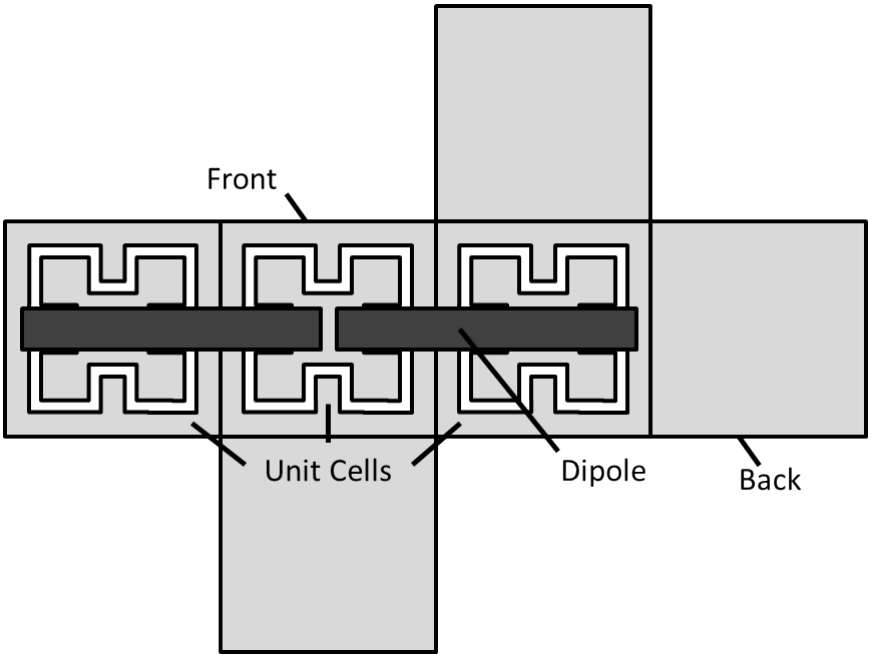

(a)

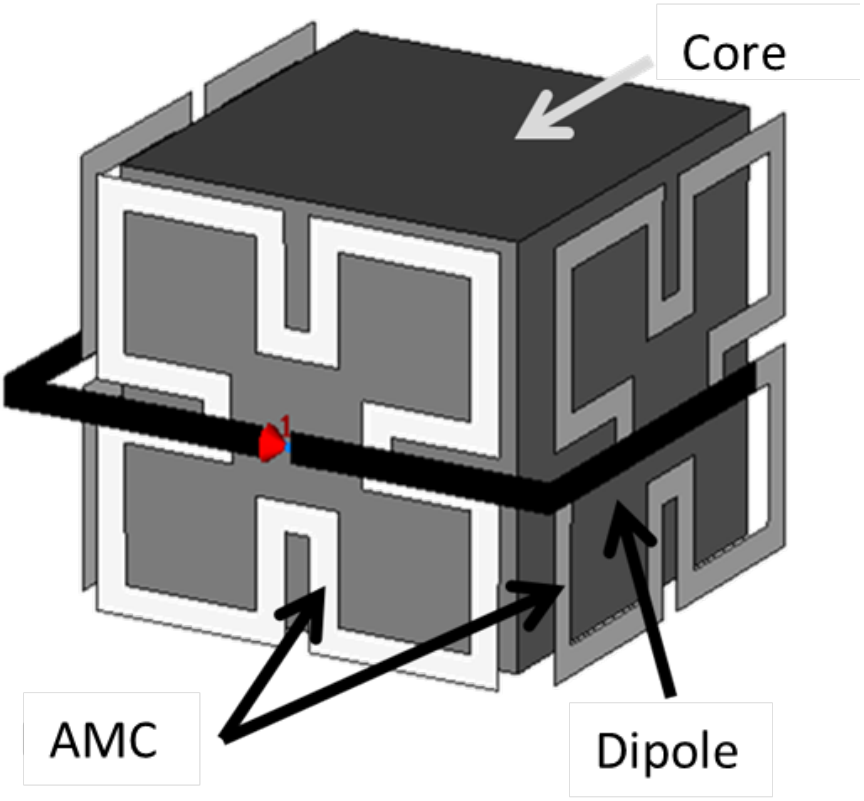

(b)

Figure 5.1: Diagram of the RFID Tag Cube (a) before and (b) after folding

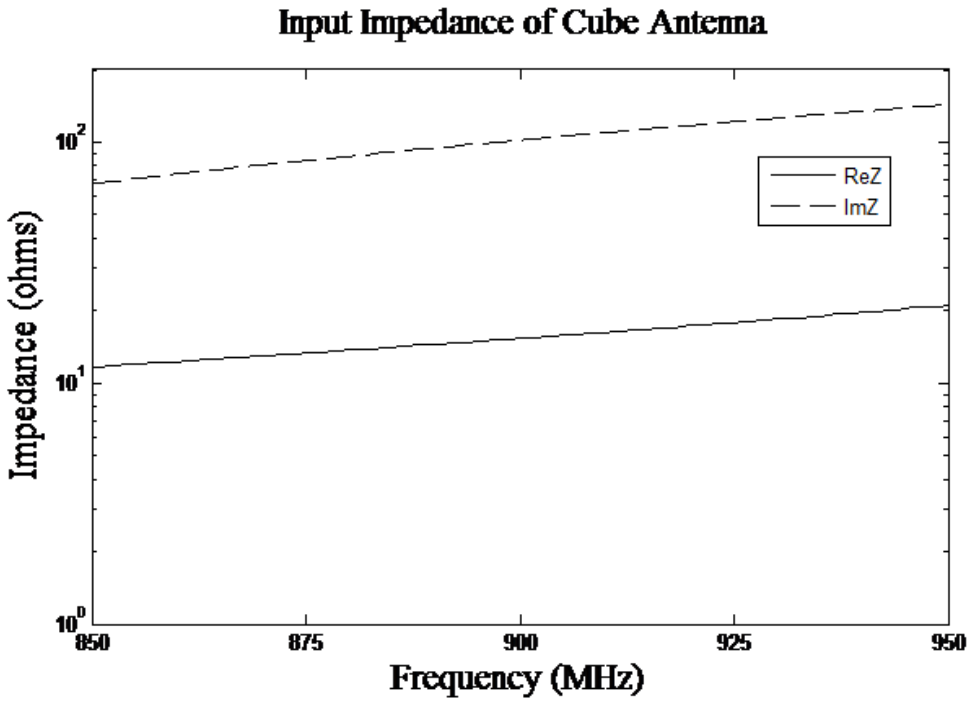

Figure 5.2: Input Impedance of the Cube Antenna

definition for reflection coeffiecent, given by

$$| \Gamma | = | \frac{Z_{cube} - Z^*_{chip}}{Z_{cube} + Z_{chip}} | \tag{1}$$

where Z_{cube} and Z_{chip} are the impedances of the cube antenna and RFID respectively, was used. The reflected power was calculated using a chip impedance of $16 - j122$ at 900 MHz, and a cube input impedance of $17.76 + j121.76$. The power reflection coefficient came out to be $\sim$ -12dB. This low value means that the cube has a good matching to an RFID chip without the need for a matching network. Thus, the third criterion is met without the need for a modification to the antenna.

5.4 Measurement

Fig 5.3 shows the cube, whose fabrication is outlined in chapter VII, under test in an anachoic chamber. As can be seen, no external connector is used on the cube. This is because the cube is meant to be used as an RFID tag, and therefore does not

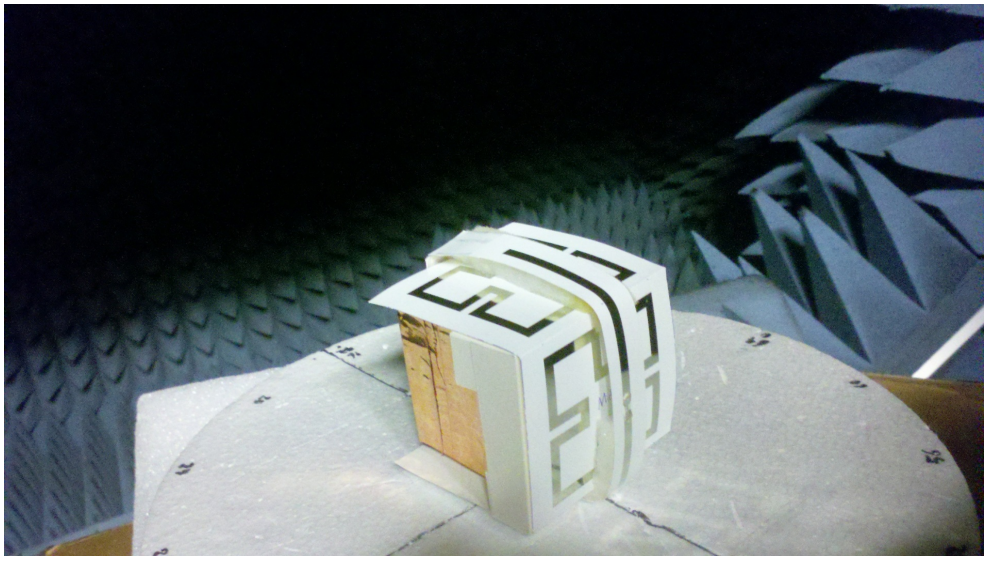

Figure 5.3: Fully Fabricated Cube

have a connector designed into it; and also any connector brought to the tag would interfere with the overall performance of the tag due to its dependence on parasitic resonators. Therefore, the measurements were made using Voyantic's Tagformance interrogator system and an off the shelf Gen2 RFID chip. The radiation pattern was calculated by determining the minimum output power required to activate the chip on the cube. These values were then negated and normalized to a maximum point (minimum before negation).

5.4.1 Results

The normalized radiation pattern, across the E-field and H-field planes, can be seen in fig 5.4. From the plot, it can be seen that the cube is an isotropic radiator with less than 3 dB variance between the direction of maximum power transmission and any other direction. Thus, the first criterion is met. At the same time, the core is made out of a solid metal housing, which isolates the inside from the outside electromagnetically.

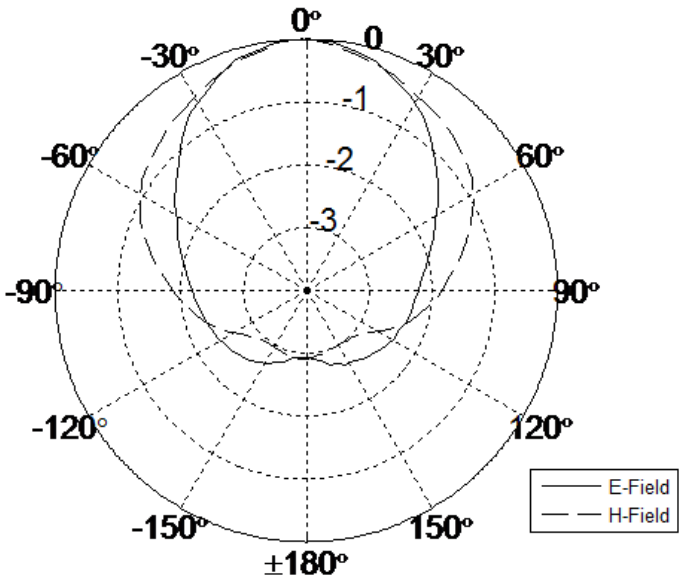

Figure 5.4: Measured Radiation Pattern of Cube for Both E-Field and H-Field

5.5 Conclusions

Presented thus far is the design, simulation, and measurement of a isotropic radiating cube antenna, with an electromagnetically isolated core, for the purpose of RFID based wireless sensing. Through measurement, it is shown that the cube acts as good isotropic radiator with less than 3dB of variance in directivity in all directions. It is explained that the core is isolated by the use of a near PEC material around the core. And, it is shown through simulation that the cube matches an RFID chip with >90% efficiency.

Through this, the cube is proven to be a versatile, low cost option in the design and implementation of RFID wireless sensors and smart skin applications.

CHAPTER VI

SECOND CUBE: FULL ANALYSIS

The previous chapter covered the basic operation of the cube topology utilizing a paper substrate. The purpose of this chapter is to build on the concepts from the previous chapter and give a complete explanation of operation. The construction of the topology presented in this chapter is outlined in detail in chapter VII.

This chapter presents a novel, 3D inkjet-printed topology for a near-isotropic radiating antenna for use in various wirelss communication, positioning, and sensor network applications. The topology makes use of a 3D conformal artificial magnetic conductor (AMC) for achieving the near-isotropic radiation pattern with less than 4.5 dB variation, and for creating an electrically isolated core for embedded hardware (e.g. microprocessor, power management, amplifier). The electromagnetic behavior of the AMC unit cells, and their role in generating the radiation pattern, is verified through simulation and measurement. The full topology is tested using a standard RFID reader. The tag's performance is proven through comparison to commercially sold RFID tags; and shown to have a gain greater than or equal to any commercial tag for $1.55\boldsymbol{\pi}$ steradians, or more than 39° from the direction of highest gain on any of the commercial tags. The topology makes use of poly-(methyl methacrylate) (PMMA) as the substrate material, which allows the topology to be rigid while still remaining low cost. The challenges of inkjet printing of silver nanoparticle-based conductive inks on PMMA are discussed, and solutions for these challenges are shown.

6.1 Introduction

In nearly all wireless systems, package based integration of antennas is a major issue. This is especially true for device fabricated in Low-Temperature Co-Fired Ceramics

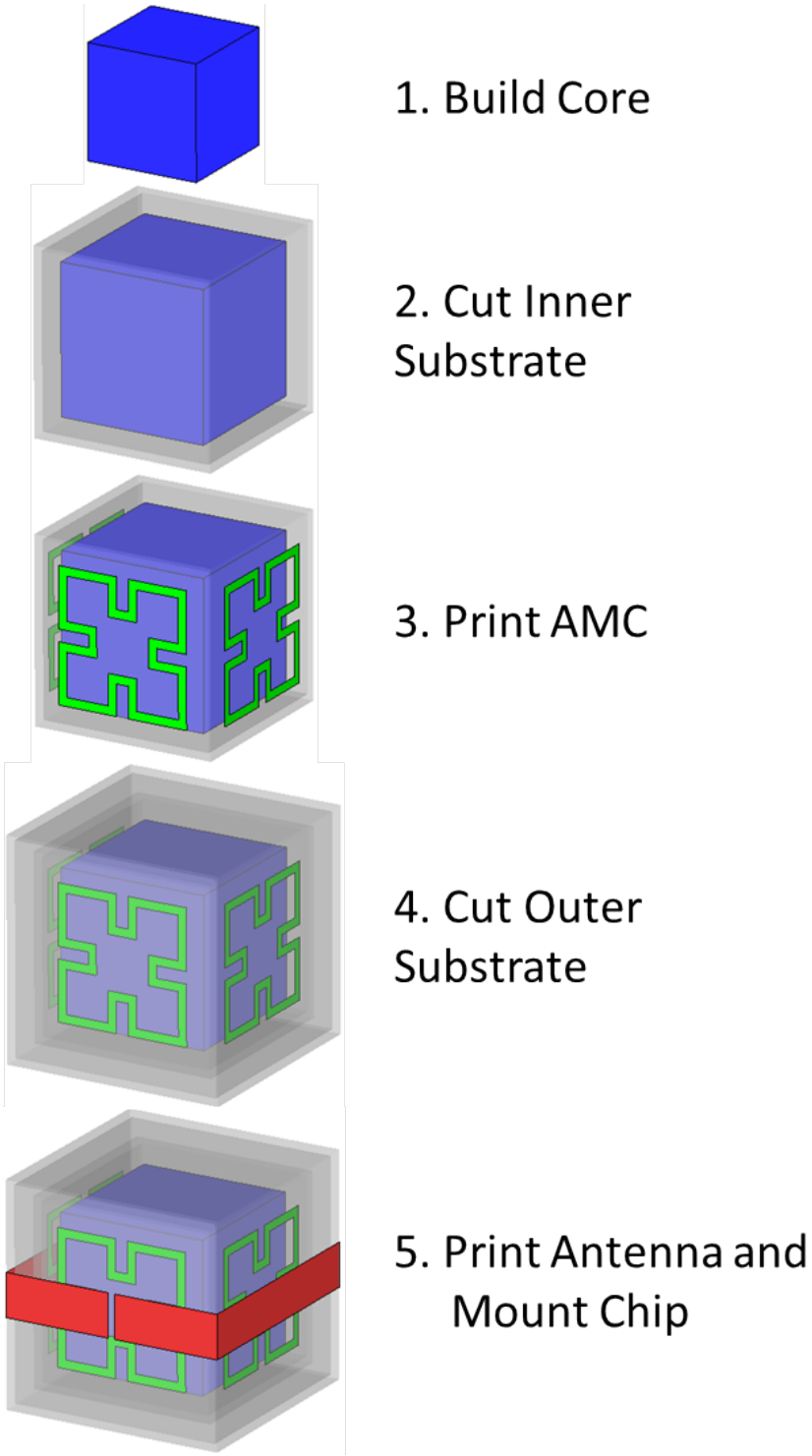

Figure 6.1: Diagram of the step-by-step fabrication procedure used in fabricating the topology.

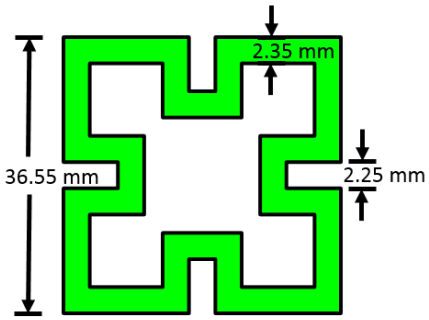

(a)

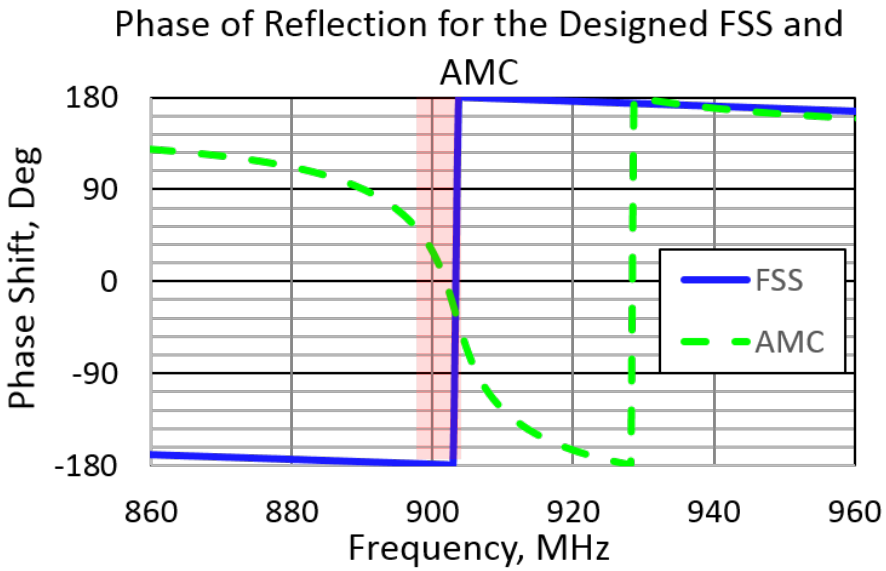

(b)

Figure 6.2: (a)An image of a 2nd generation convoluted square, and (b) the phase of Reflection for the designed FSS and AMC constructed from the convoluted square.

(LTCC) fabricated circuits, or for on-body wireless identification devices and distributed RFID-based wireless sensors. Typical wireless system packages include lossy materials and metals that degrade the performance of the integrated antennas. Therefore, attempts have been made, using planar meta-materials, to isolate an antenna from potentially disruptive parts [20, 50]. These planar structures are tuned to act as artificial magnetic conductors (AMC), which reflect the antenna's radiation away from the materials, but do not de-tune the antenna like an electric conductor. This reflection also serves to effectively increase the directivity of the antenna apparatus.

The increase in directivity obtained from a standard AMC is not always desired. For example, in applications where RFID tags, or RFID-based sensor tags, are deployed in a random manner, the orientation is difficult to control. When the tags land such that they are oriented to radiate away from an interrogator, it is difficult or impossible to achieve communication between the interrogator and tag. Thus, antennas are needed that can radiate near isotropically, or in every direction with little variance in power level.

Several near-isotropic antennas have been demonstrated in literature. These antennas include a dipole coupled with a resonator printed on Kapton Polyimide presented by Varadan et al. yielding >9dB variances [47], two crossed dipoles presented by Pan et al. yielding >4dB variance [59], four phased monopoles in a circle presented by Huchard et al. yielding >8dB variance [42], and a spherical 3D printed antenna presented by Berge et al. yielding >10dB variance [7]. Unfortunately, these antennas have a limited applicability to practical sensors, or other devices, as they have been mostly optimized for free-standing antenna configurations without embedded metal structures. Thus, a radiator is needed that can achieve near-isotropic radiation, while keeping the radiator isolated from any potentially integrated circuitry or sensors. An isolated core radiator is covered by Monti et al., which makes use of patch antennas wrapped around a core [57]. However, this leads to a very large topology ($>\mathbf{.5\lambda}$ in

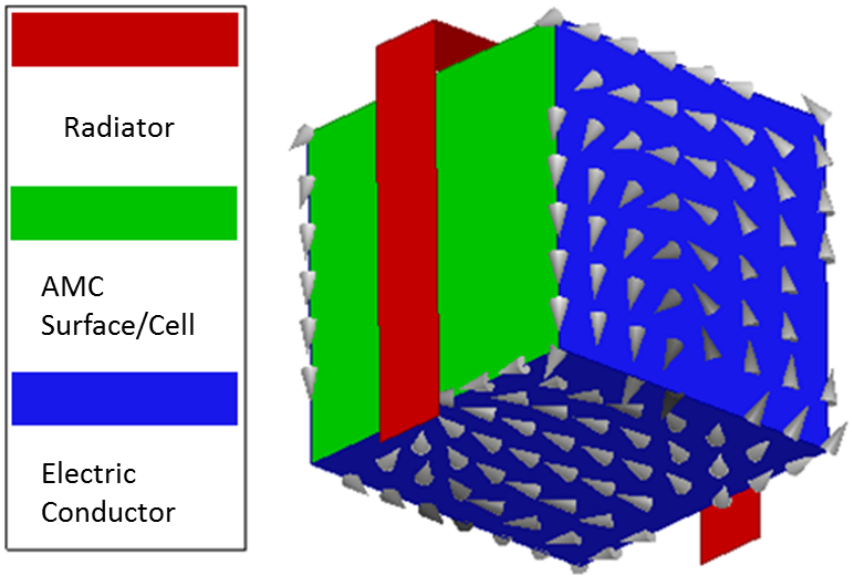

(a)

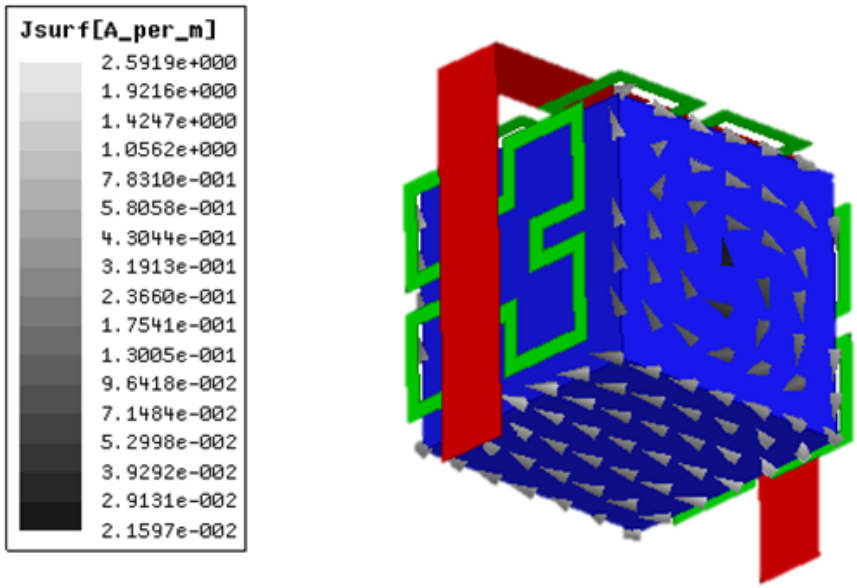

(b)

Figure 6.3: Current distributions on the conductive sides of the topology when implementing (a) PMCs and (b) AMCs on 3 of the sides.

each dimension) and does not give the desired isotropic radiation pattern. Therefore, covered within is the design of a topology which is able to achieve both a near isotropic radiation pattern and an isolated, embedded core.

Since the proposed sensing platform may be used in a wide variety of deployment schemes, it is necessary to consider the cost and ease of production. A similar design has been covered in the literature [27], which used paper due to its low cost. However, some environments, such as those containing high amounts of moisture, or those in which the topology could be structurally damaged, would be difficult for a paper based tag. The design also lacks a clear description of the AMC's operation, making it difficult to scale for different substrates. Therefore, an antenna topology is needed which utilizes a more rigid, while still low cost, substrate material, and which gives a clear description of how it operates.

Inkjet printing is chosen as the means of fabrication due to its low cost, and it being a purely additive process. Inkjet printing is also chosen as it allows for rapid fabrication without the need for a clean room, or other pieces of expensive equipment often used in metal deposition. Cook et al has demonstrated inkjet printing as a viable means of fabrication in multi-layer structures, especially those containing multiple polymer layers [18, 21], which makes it desired for this topology.

Covered in the following sections is the design, construction, and testing of the proposed topology. First is covered the design of a conformal AMC for use in the topology. This design is accompanied with an analysis of how the AMC unit cell behaves in the design-required frequency selective manner as well as why the proposed 3D AMC configuration features a near-isotropic radiation pattern. The second topic covered is the low-cost, purely additive, inkjet-printed construction of the topology, including the choice, testing, and preparation of the materials. Finally, the performance of the fabricated prototype is measured and compared with simulation. In addition, the proposed topology is benchmarked by comparing it to the performance

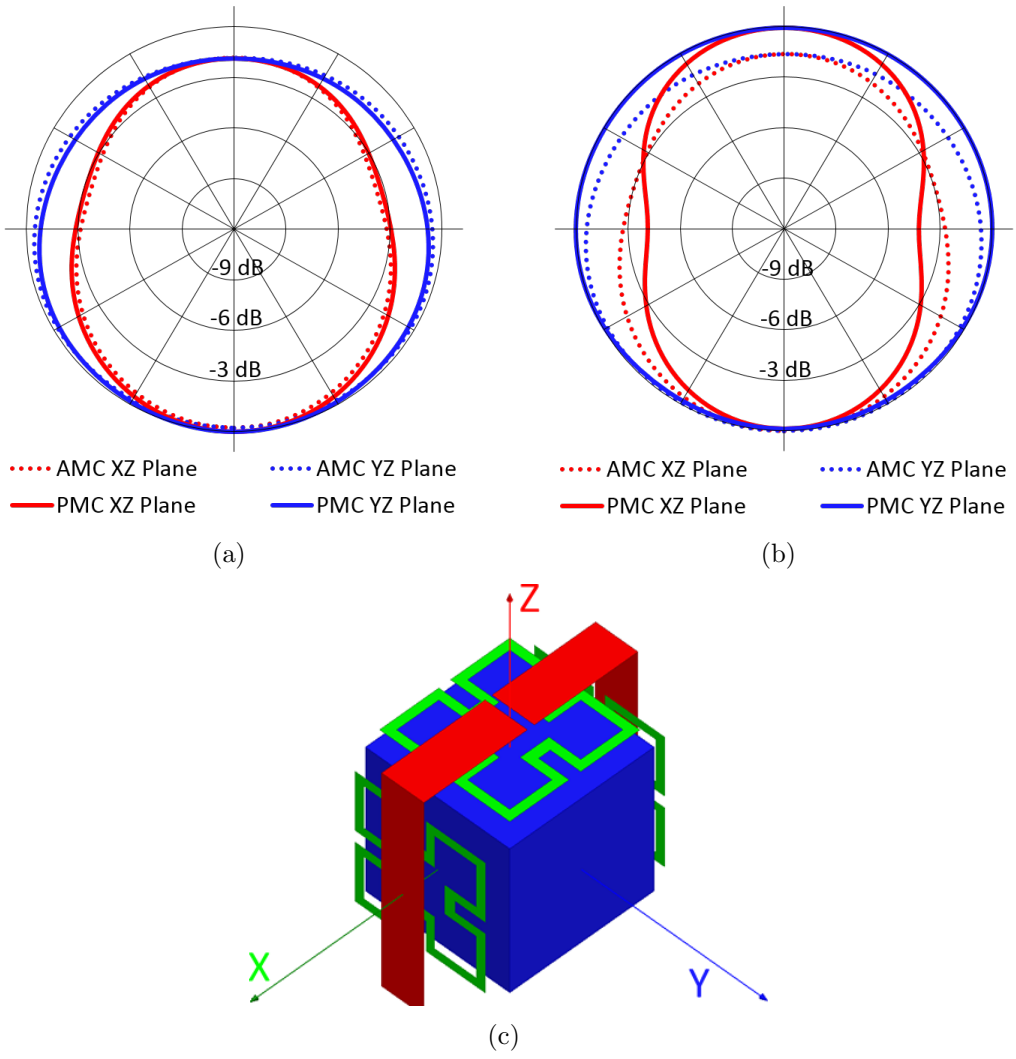

Figure 6.4: Overlay of the normalized Radiation Patterns for ideal PMCs and AMCs on (a) 3 and (b) 6 sides of the topology, with (c) an image of the topology including axis labeling.

of various, commercially sold RFID tags.

6.2 Design and Tuning

The objective of the design is threefold: the final topology is capable of radiating near isotropically; a user is able to embed a wide range of devices, including processors, power supplies, discrete sensors, and/or amplifiers; and the embedding of any devices does not interfere with the radiating properties of the topology.

To this end, a topology is designed which utilizes a cubic core constructed of six highly conductive walls to electromagnetically isolate the interior of the core from a radiating source around the core. A radiating element is designed such that when placed around the core the desired near-isotropic radiation pattern can be achieved. Since placing a radiator around a conductive core would impede its effective radiation for any radiator which does not require a via to the core [57, 80], or a very large spacing between radiator and core, the topology is designed to make use of a conformal artificial magnetic conductor, or AMC. The core is chosen to be a cube, with the AMC covering multiple sides, isolating the core and the radiating element, which is chosen. The radiating element is chosen to be a dipole wrapped around the sides of the core. The cube is chosen for the shape of the topology as it has a high volume to largest dimension ratio while remaining simple to construct. The dipole is chosen based on many characteristics, including simplicity in construction, its easily manipulated current paths, and its lack of need for a via in order to operate. A layer-by-layer design of the final, desired topology can be seen in fig. 6.1.

6.2.1 AMC Design

The AMC unit cells are designed by first creating an ideal frequency selective surface, or FSS, which is comprised of a planar array of an infinite number of identical resonating structures, or FSS unit cells. In simulation, the FSS is excited by a TEM mode wave of normal incidence. The FSS is fine tuned such that it reflects all power at the

desired frequency of operation. Per the function of an FSS, at the center frequency, where all power is reflected, the reflected wave yields a phase shift of 180 degrees, making it appear as an electric conductor. Though it yields isolation between the front and back, as is desired for the core of the topology, the appearance of being an electric conductor still causes the detuning of radiating elements placed in close proximity. However, when the FSS is placed over an infinite ground plane in close proximity, on the order of $\frac{\lambda}{10}$, the phase of reflection is shifted by 180 degrees, making the FSS now appear as an AMC [20]. The difference in phase between the FSS and AMC, constructed from the chosen unit cell shown in fig. 2(a), can be seen in fig. 2(b).

Since the wrapped dipole around the topology is in close proximity, on the order of $\frac{\lambda}{10}$, to the AMC, and the AMC will be in a non-ideal configuration (neither an infinite, nor a planar array) around the core, the AMC unit cells in the topology may be excited from varying angles and directions. Therefore, a circularly polarized unit cell is chosen. The unit cells are chosen to be around 1/6th of a wavelength long, at the center frequency of operation, as this corresponds to approximately the dimensions of the core. To this end, a 2nd generation convoluted square, which is smaller than a 1st generation, is chosen as the resonant structure in the FSS [25, 60], and thus also the AMC.

A smaller structure could be used, such as a 3rd generation convoluted square, but the bandwidth of the AMC would be reduced. As can be seen in the highighted region of fig. 2(b), the +/-45andwidth of the 2nd generation convoluted square is already small, and per the chu-harrington limit, seen in eq (1), decreasing its size would only decrease the bandwidth.

$$\boldsymbol{Q = \frac{1}{k^3 a^3} + \frac{1}{ka}} \tag{1}$$

such that

$$\boldsymbol{k} = \frac{\boldsymbol{\lambda}}{\boldsymbol{2\pi}} \tag{2}$$

where $\boldsymbol{\lambda}$ is the wavelength at the center frequency, and a is the diameter of the smaller sphere the element can fit within. A larger bandwidth is desired as it mitigates errors due to innaccuracies in fabrication.

The spacing between the AMC unit cells and the ground, as well as the spacing between the AMC unit cells and the radiating element are covered in the following section.

6.2.2 Non-ideal AMC Unit

In the design of the AMC unit cells, the assumption that was previously used that the unit cells exist in an infinite, planar array over an infinite ground plan. Of course, in applying the AMC unit cells to the full topology, all three of these assumptions are lost. In order to determine whether the unit cells still operate as AMCs, a set of simulation are run utilizing equation-based perfect magnetic conductors, PMCs, and the AMC unit cells. Since the PMMA substrates play a role in field distribution around the topology and the unit cells are tuned to operate on the PMMA substrate, the properties of the PMMA are taken into account in the unit cell simulations.

The first set of simulations compared a topology with PMC/AMC unit cells on three sides of the core. The dipole used was optimized for performance in the AMC design. Fig. 6.3, show the current distributions on the surface of the electrically conductive faces of the core for the PMC model and the AMC unit cell model respectively. As can be seen in fig. 6.3, the currents largely match up, with the disagreeing currents having two orders lower magnitude. Fig. 4(a) demonstrates a strong agreement between the PMC and AMC unit cell models, with less than half a dB of difference between the two.

The second set of simulations compare a topology in which all six sides are covered

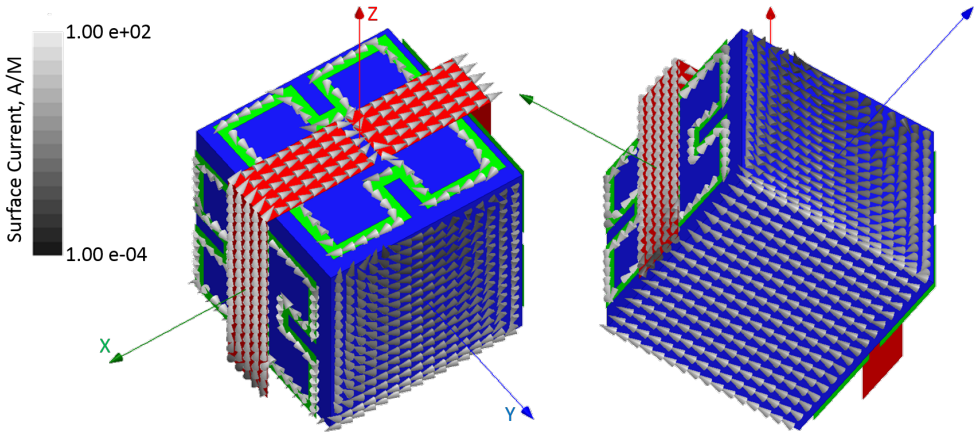

(a)

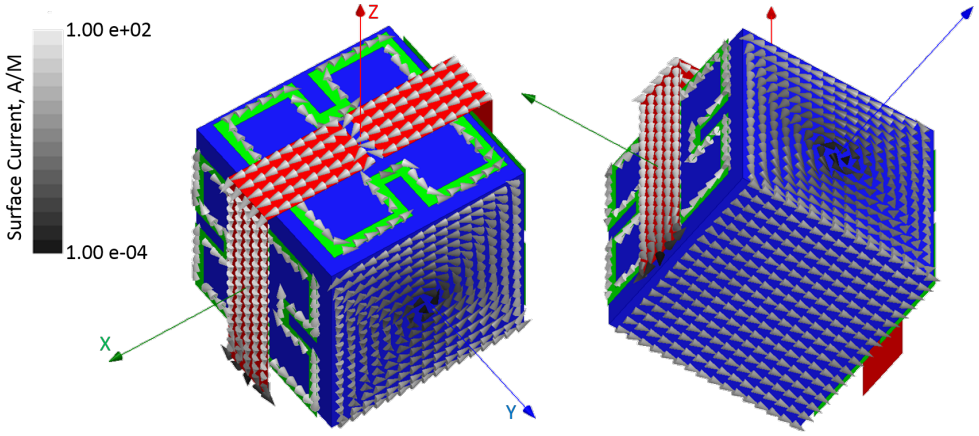

(b)

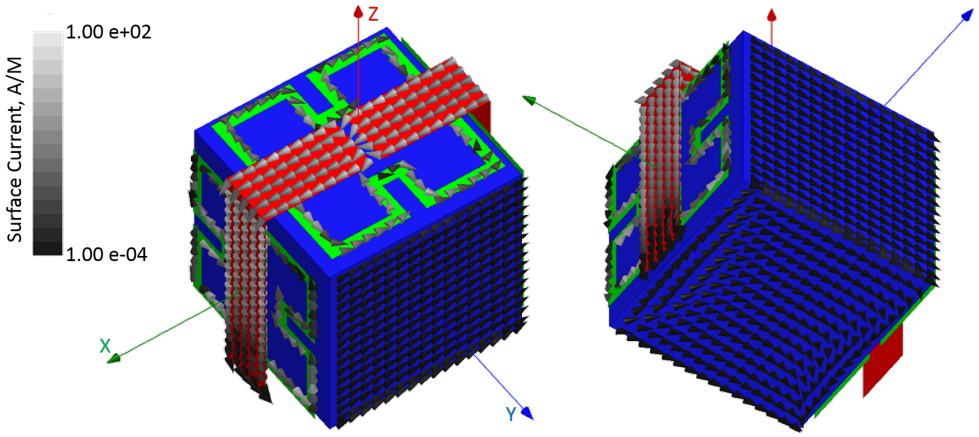

(c)

Figure 6.5: Currents induced on the topology by waves propagating in the a) -Z direction, b) -X direction, and c) -Y direction.

in PMC/AMC unit cells. Fig. 4(b) shows the overlay of the radiation patterns for both the PMC and AMC unit cell models. Due to all sides containing magnetic conductors, there are no surface currents to show. From fig. 4(b), though, it can be seen that the AMC unit cells do not operate as AMCs when covering all six sides. This discrepancy is most likely caused by the method of exciting the AMC unit cells. In the ideal AMC case, and in the AMC unit cells on three sides, the cells are excited by a source on their face. In case where the AMC are on all six sides, the unit cells not located directly underneath the dipole are excited from the edges. From Kiani et al., it can be seen that exciting an FSS/AMC at an oblique angle can alter the cells' operation [46]. It can be assumed, that these unit cells are no longer operating in the same region as the unit cells located beneath the wrapped dipole, and therefore no longer behave as AMCs.

From fig. 4(a) and 4(b), it can be seen that both cases give radiation patterns with marginally different amounts of variance between a minimum and maximum gain. Since the topology is meant to demonstrate conformal AMCs, the topology utilizing AMCs on three sides is used, as, in this model, all AMC unit cells operate as AMCs.

6.2.3 Near-isotropic Radiation Pattern

From looking at the current distributions in fig. 6.3, the topology can be considered as having 6 independent current sources for generating the radiation pattern. Three of the currents are located on the center and two sides of the wrapped dipole with the AMC backing. The other three sides, which are excited by the fields from the dipole, act as the subsequent three current sources. Since the non AMC sides on the +Y and -Y faces contain a significantly smaller current magnitude, they play an insignificant role in generating the radiation pattern.

The four significantly radiating sides line up to create a continuous circle of current

around the topology. The core isolates currents on opposing sides. Therefore, currents on opposing sides of the topology neither constructively nor destructively interfere with the radiation of each other. All currents travel in a fairly straight path and do not radiate in the direction of current flow. Therefore, the currents on adjacent sides do not significantly interfere with each other.

The non-interference means that there are no directions of phase cancellation in the radiating energy. The presence of four independent radiators on all sides of the topology, mean that a signal is being generated in all directions. Therefore, the final topology yields a near isotropic radiation pattern with a very small variance.

Fig. 5(a), 5(b), and 5(c) show the currents on the topology which correspond to waves propagating in the in the Z, X, and Y directions, respectively. From these figures, it can be seen how the individual current components, which when combined create the distribution in fig. 3(b), generates radiation along each of the axes.

6.2.4 Inter-layer Spacing

When considering the spacing in between the ground, AMC unit cells, and the radiating element, 4 different criterion are taken into account: total size of the topology, total antenna gain, total variance in gain in all directions, and input impedance of the radiator. With the goal of keeping the total size of the topology down, the spacing between the elements is kept to a few mm. To this end, a sweep of the spacing is performed while simulating the total gain of the antenna (including losses in the conductive traces and substrate, but ignoring the gain achieved from matching the input impedance of the radiator with the input impedance of the RFID chip used in the measurement in section IV), and the difference in gain between the direction of highest and the direction of lowest gain. The plots of these values can be seen in fig. 6.6.

Simultaneously, the natural input impedance, or the input impedance without

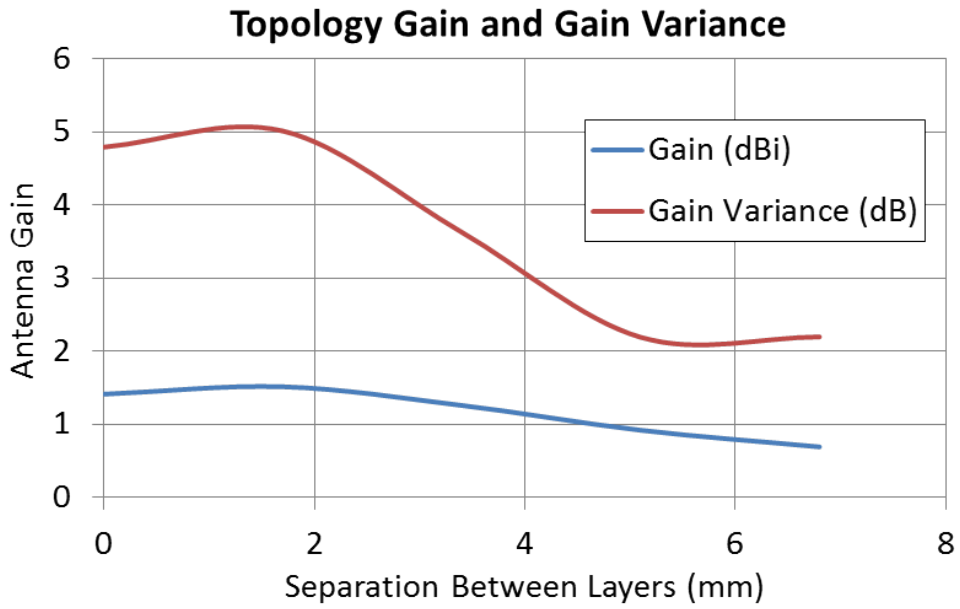

Figure 6.6: Plot of the (blue) peak gain of the topology including material losses, but not impedance mismatch losses, in dBi, and (red) the total variance of gain, in dB, in all directions vs the inter-layer spacing of the topology.

matching network, of the radiating element was tracked and plotted in fig. 7(a). The power reflection coefficient [52] between the natural input impedance and the chosen RFID chip's input impedance can be seen in fig. 7(b). Though the final design includes the use of a T-match network, the simulations are performed with the original impedance being tracked. This choice of using the original impedance is based upon the idea that the more the matching network needs to shift the impedance, or the further the natural impedance of the radiating element is from the input impedance of the RFID chip, the narrower the matching network's bandwidth will become. This increase in bandwidth is desired in order to avoid problems from layer misalignment during the fabrication phase.

Another consideration is the material being used. Since the sheets of PMMA being used vary in thickness around 1.7 mm, when choosing a spacing, it is best to use an integer multiple of this value. Therefore, based on the discrete spacing options

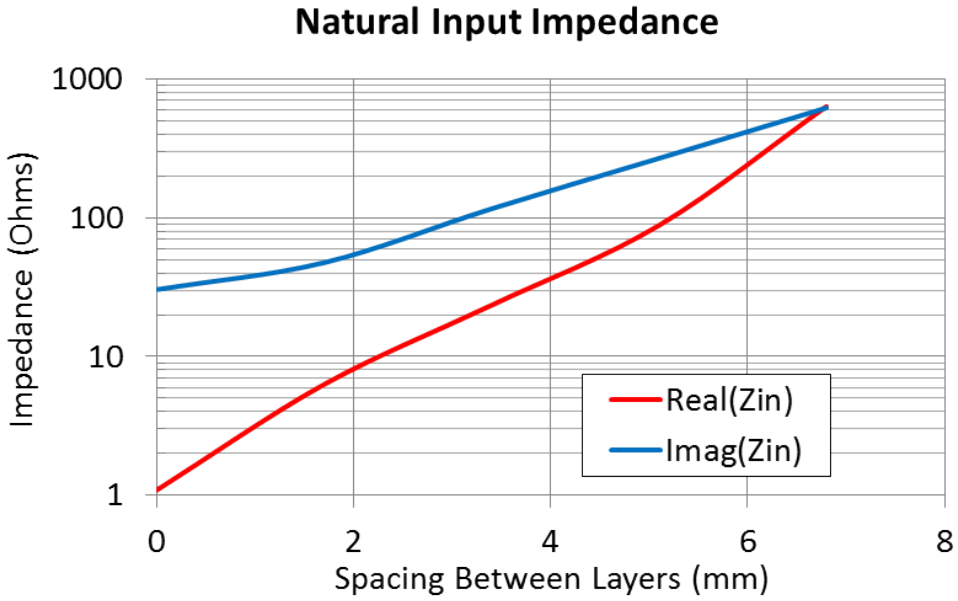

(a)

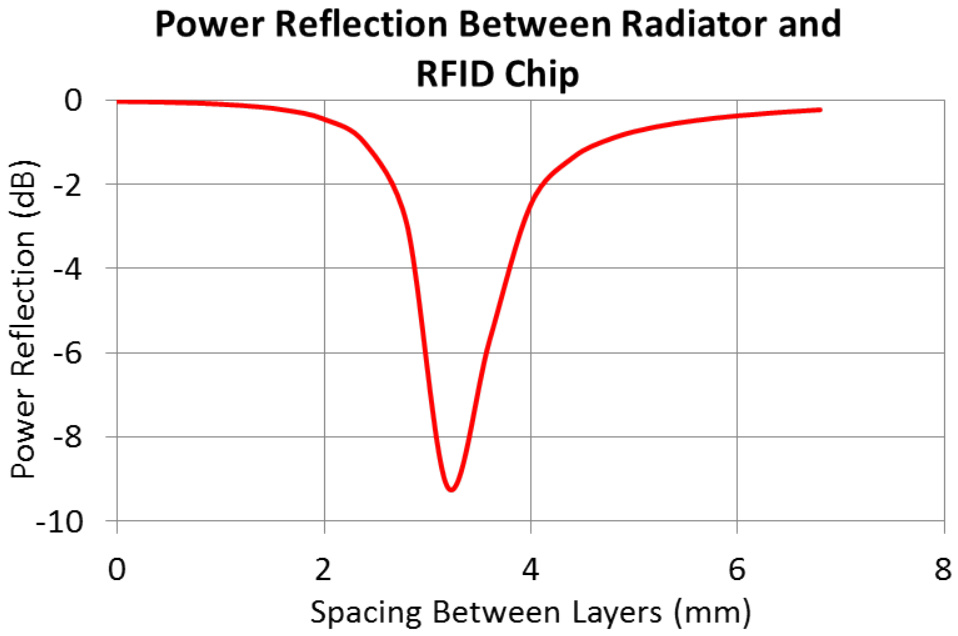

(b)

Figure 6.7: Plots of the (a) input impedance of the radiating element without a matching network attached, and (b) the power reflection coefficient of the input impedance with the RFID chip used in measurement.

and the simulation data collected above, 3.4mm is chosen as the optimal choice for spacing within the topology.

6.2.5 Substrate Preperation and Retuning

As is covered in the next section, PMMA is chosen as the substrate for the topology. Due to its thickness, permittivity, and loss tangent, PMMA contribute to decrease in the efficiency of the topology. Since the permittivity and loss tangent are constants of the material, the only solution to decreasing the losses is to decrease the thickness of the PMMA. At the same time, PMMA is chosen as a substrate in order to increase rigidness. This rigidness would be sacrificed if thinner sheets were used. Therefore, channels are etched out of the PMMA substrate directly under where any AMC unit cells or the wrapped dipole is placed in order to reduce effects of the lossiness of the PMMA. The PMMA substrate and etching are both taken into consideration in the primary (FSS stage) and secondary (AMC units placed around the core) tuning of the cube topology.

After all the elements are placed together, a T-match network is placed on the wrapped dipole and the cube topology is iteratively retuned. The retuning was done using optimization software built into CST RF & Microwave Simulator. The antenna was tuned in order to yield the least amount of variance in the radiation pattern, and an input impedance of $\mathbf{13 + j220}$ (the complex conjugate of the input impedance of the passive RFID chip used in the antenna measurements). Fig. 6.8 shows the full dimensions of the cube after the retuning has been performed.

6.3 construction

The fabrication was done using a Dimatix 2800 inkjet printer (Fujifilm) utilizing drop on demand, piezo heads, a Jelight Company Inc UVO Cleaner (UV-ozone oven), a BlueM enclosed, air-filled oven, and an epilogue mini laser milling machine. The materials used are 1.5mm thick extruded PMMA (McMaster-Carr, Atlanta), and

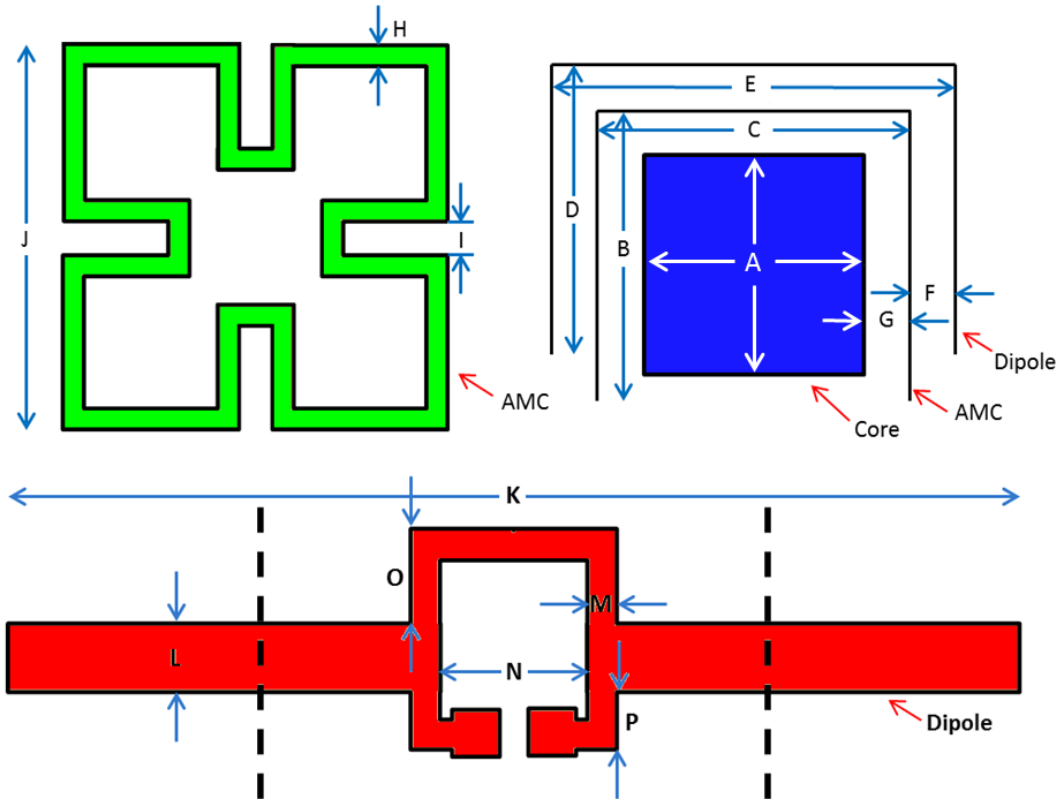

Parameter	Dimension (mm)	Parameter	Dimension (mm)
A	39.8	I	2.25
B	51.38	J	36.55
C	51.38	K	180.45
D	60.15	L	11.85
E	60.15	M	1.45
F	3.4	N	13.25
G	3.4	O	4.5
H	2.35	P	12.1

Figure 6.8: Structure and dimensions of the full topology after optimization.

Cabot Silver Conductive Ink (Sigma-Aldrich).

The step by step process of constructing the cube, described in detail in the following subsections, is outlined in fig. 6.1

6.3.1 Substrate Material

Cooper et al. covered a similar design that is inkjet printed on a paper substrate [27]. This previous design is structurally unstable, due to the use of paper as a substrate, and thus lends itself to inaccuracies during fabrication. In addition, paper is susceptible to water and physical damage. This susceptibility limits the environments and application in which paper can be used. In order to overcome these limits another material is chosen for this design.

Extruded poly(methyl methacrylate), or PMMA, is chosen as the substrate material. Though more expensive than paper, PMMA is still low cost as a substrate, costing about 1.3 cents per cubic cm of 1.5mm thick sheets(McMaster-Carr) for small quantities; and costing even less when purchased in bulk. PMMA has a lower loss tangent than paper (.01 to .007 vs papers 0.07 [19]). The higher permittivity of PMMA, combined with the use of thicker sheets of PMMA (in comparison to paper), means that more of the fields around the radiating and resonating elements will be contained within the material versus those contained in a paper substrate. Thus, the bulk losses in a PMMA substrate are a factor in the operation of the topology.

In order to decrease the losses, the PMMA substrates are laser etched underneath where the metallic trace will be printed for both the AMC unit cells and the wrapped dipole radiating element. The etched cavities are cut to be twice the width of the metallic traces, and half the depth of the PMMA sheets.

6.3.2 PMMA Etching and Cutting

As is mentioned in section II, the PMMA is etched underneath where the traces for the AMC and dipole are placed in order to reduce losses. The etching is done using a laser

etcher. It is possible to perform the etching in a single sweep; however, due to the low glass transition temperature of PMMA (120 depending on method of construction), the etching process can cause warping if done at too high of a temperature. Fig. 6.9 shows an image of a PMMA sheet which is warped from etching in an excess temperature. In order to avoid this warping, multiple passes at a high speed and low power level are performed. 10 passes, at a power setting of 4 Watts, are chosen for use in the final design to achieve a thickness of less than .8 mm while avoiding warping of the 1.5 mm thick sheets of PMMA. The power settings and thickness are determined from previous work [17].

12 Watts at 20% speed for 4 passes is used for cutting out the PMMA pieces. Again, a low power and multiple passes are used in order to prevent the PMMA from warping.

6.3.3 Printing and Curing

In order to print the conductive traces for the antenna and AMC, the surface tension of the PMMA had to be modified. PMMA normally has a very low surface energy in comparison to the organic solvent based silver ink. In addition to the inherent low surface tension, the etching of the cavities on the back side of the PMMA sheets raised its temperature and thus further lowered the surface energy. To increase the surface energy, and thus allow for printing of the silver ink, the PMMA sheets are prepared in a UV-ozone oven. In order to determine the correct amount of exposure, several traces are printed on etched pieces of PMMA, which had been exposed to different amounts of UV-ozone. Fig. 10(a) shows images of the silver traces after they had been slow dried in an air filled oven. As can be seen, low-to-no exposure of UV-ozone led to the ink pulling from some sections of the trace and pooling in the end. As the exposure to UZ-ozone increased, the traces pulled less and less. After 75 seconds of exposure, the ratio of substrate and ink surface tension was acceptable for

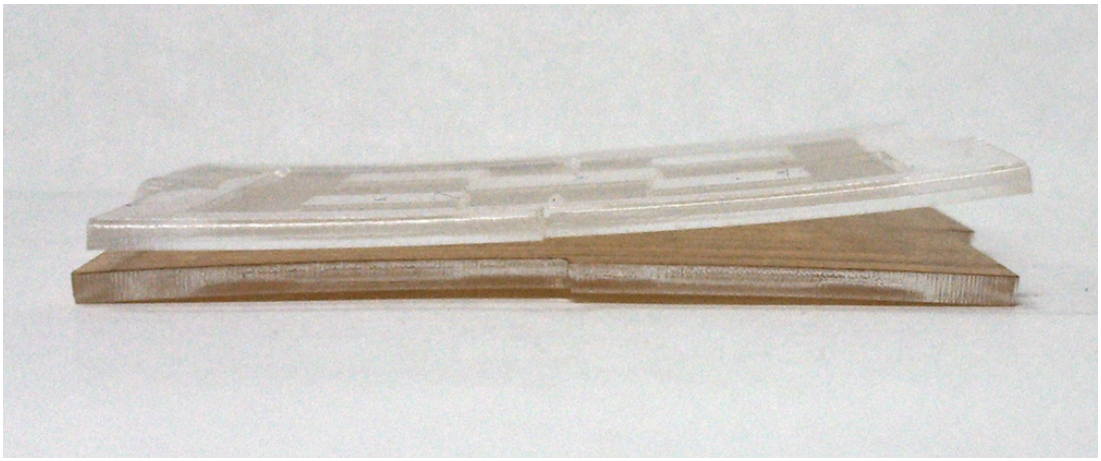

Figure 6.9: Sheet of PMMA cut at too high of a power level during the laser etching process.

adequate adhesion.

The literature shows the surface energy to be 41.1 $\boldsymbol{mJ/m^2}$ [9]. However, the surface energy of a material can change from manufacturer to manufacturer. Therefore, the surface energy is remeasured with the results shown in fig. 10(b). As can be seen, the inherent surface energy of the PMMA is 41 mN/m. However, this is increased utilizing UVO to improve the wettability of the ink.

Fig. 6.11 shows the profile of a 2mm and 10mm wide trace which are printed after the PMMA has been exposed to 75 seconds of UV-ozone. As can be seen, the traces have an average height of 1.27$\boldsymbol{\mu}$m, yielding about 450nm per layer of printer silver. The 2mm wide trace is used in determining the sheet resistance and bulk conductivity of the traces.

The silver traces, once printed, are normally raised to temperatures in excess of the PMMAs glass transition temperature [19]. Therefore, the traces are cured in two steps. The PMMA with printed silver traces is placed in an open air oven. The temperature of the oven is slowly raised to 80, and kept there until the inks solvent has fully evaporated. After drying at 80 for 4 hours, the silver traces are sintered using the epilogue mini laser. The concept of laser curing is based on the work by Laakso, et

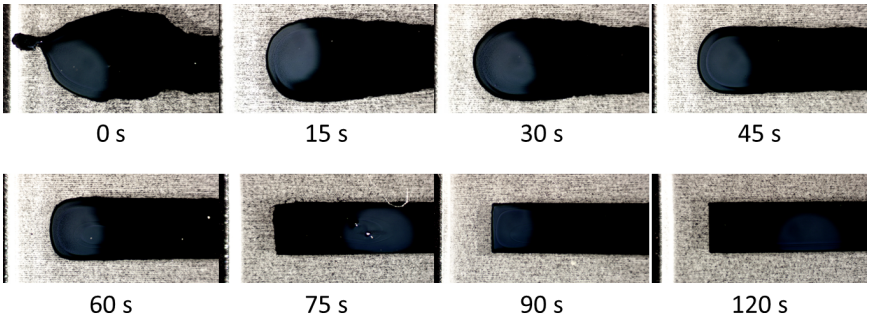

(a)

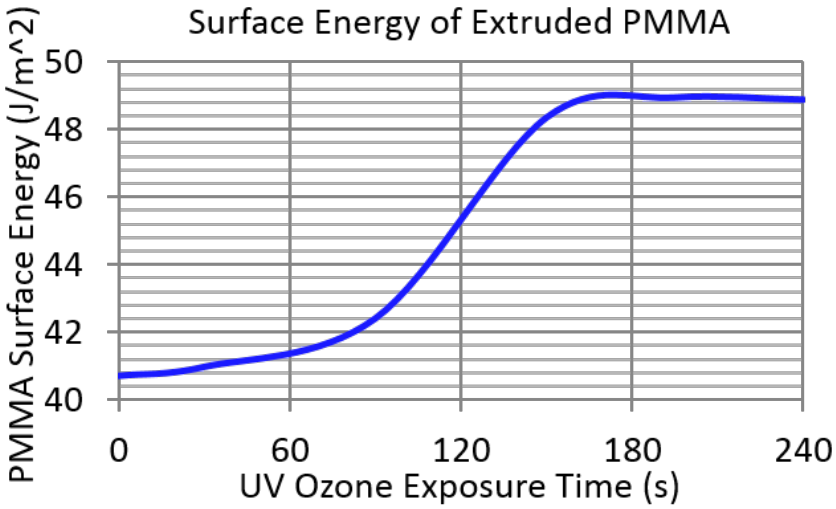

(b)

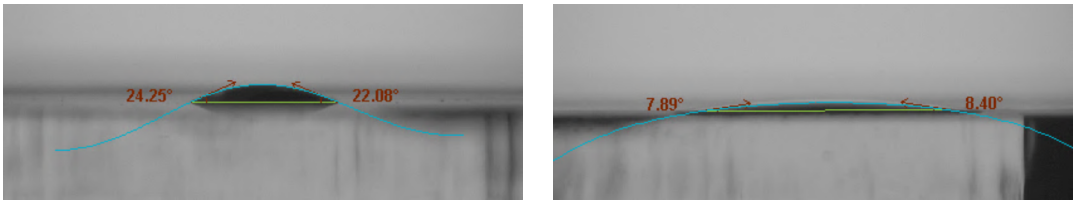

(c) (d)

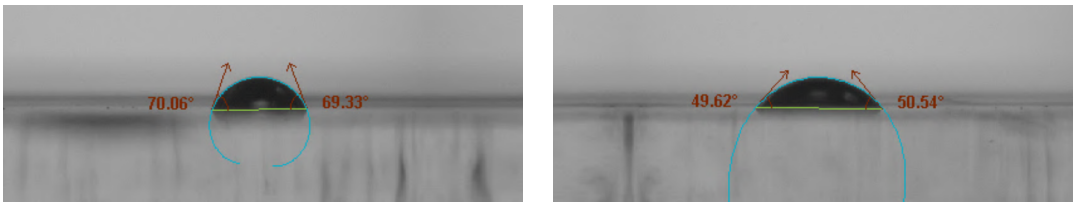

(e) (f)

Figure 6.10: (a) Images of ink adhering to PMMA after the PMMA has been exposed to varying amounts of UV-Ozone, (b) plot of the surface energy of PMMA vs UV-Ozone exposure times, and (c,d) DMSO and (e,f) DI Water droplets on a PMMA sheet with (c,e) low and (d,f) high surface energy.

al. [53]. The sintering is done in multiple passes with the lasers focal point being 7 mm above the substrate in order to prevent cracking of the silver due to rapid, localized temperature increase. As each substrate yields different results in silver curing a parametric sweep of sintering laser power levels is performed. Each pass increases the intensity of the laser from 1 W to 33 W. Fig. 6.12 shows the resistivity in ohms per square as the laser intensity is increased. The measurement was conducted three times on three structures in order to demonstrate the repeatability of the sintering process.

6.3.4 Post Processing

Once the traces are printed and sintered, the PMMA sheets are put together using crazy glue that melts the PMMA sheets together. A conductive epoxy is used to mount the RFID chip, as well as connect the antenna traces together at the joints. Due to the simplicity of the core cube, it is constructed using conductive adhesive copper tape. The tape is wrapped around the PMMA cube by hand.

The three parts of the topology and the fully fabricated structure can be seen in fig. 6.13.

6.4 Measurement and Comparison

In order to avoid cable interference, all directivity and relative gain measurement are performed using a Voyantic Tagformance Lite RFID measurement device. The cube topology is mounted with an NXP EPC Gen-2 RFID chip allowing for communication with the reader. All measurements are performed at 1.5 meters in an anechoic chamber in order to guarantee a strong, accurate signal.

The cube topology is first measured by rotating it through 360 degrees in both XZ and YZ planes, as these correspond to the E- and H- planes of the wrapped dipole. These planes are defined in fig. 4(c). A plot of the measured and simulated radiations patterns in the XZ and YZ planes can be seen in fig. 6.14 along side a picture showing

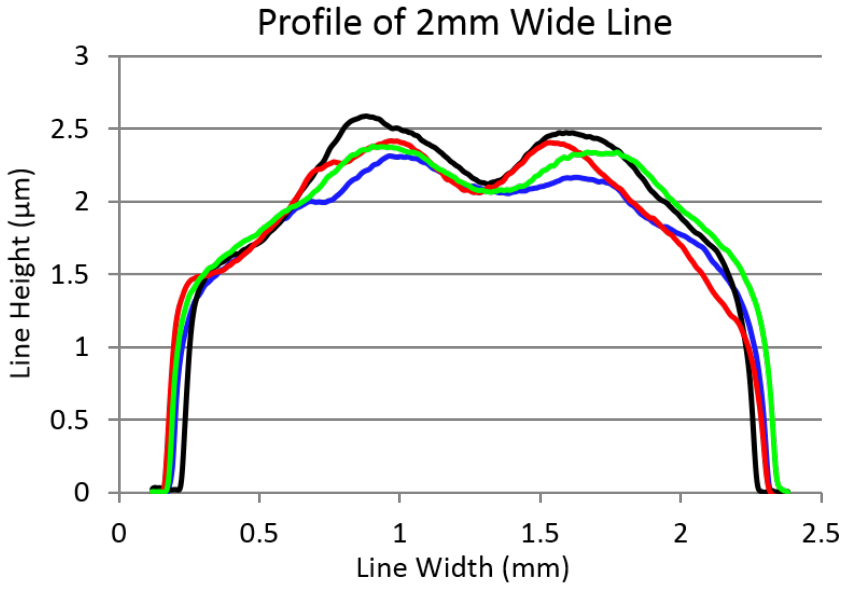

(a)

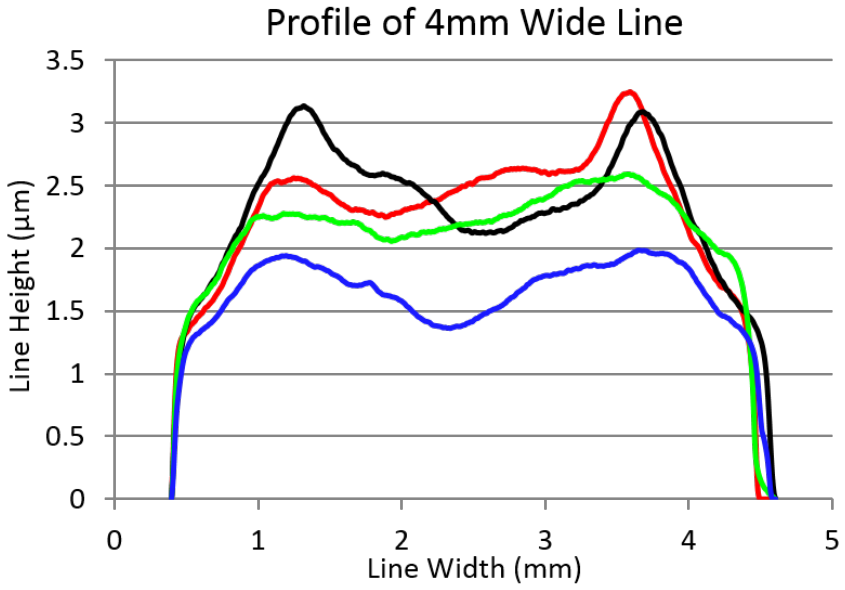

(b)

Figure 6.11: Profilometer Measurements of a (a) 2mm and (b) 10mm wide trace of silver printed on PMMA after 90 seconds of UV-ozone exposure.

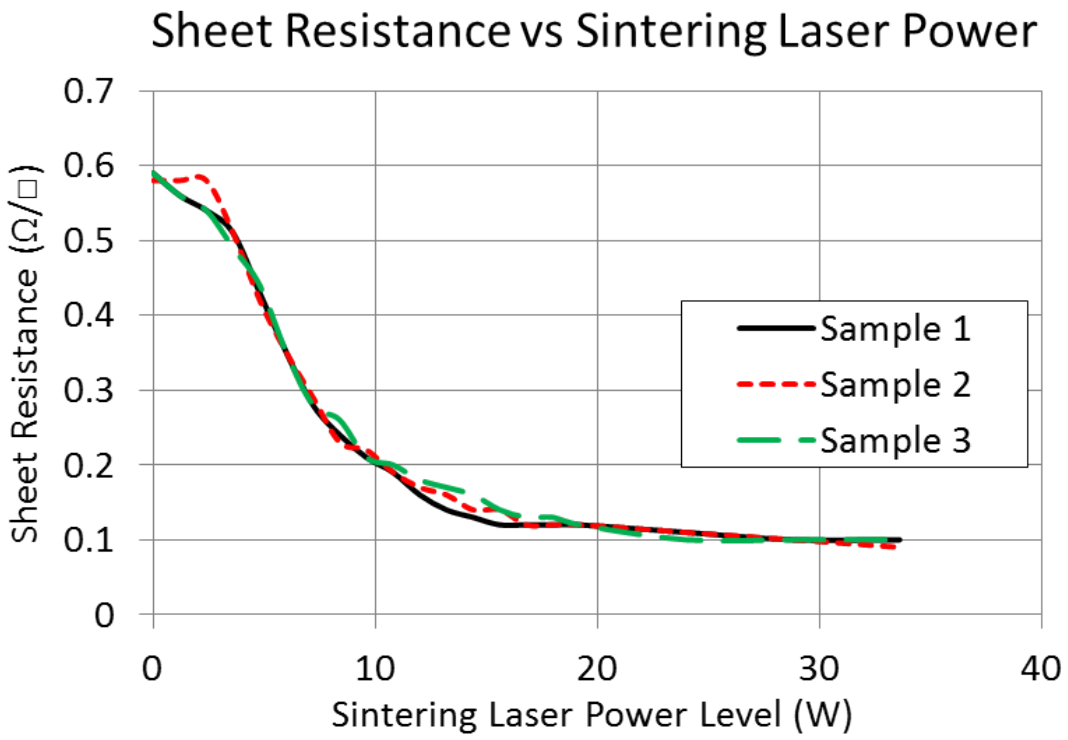

Figure 6.12: Measured sheet resistance of silver ink traces printed on PMMA after varying power levels of laser sintering.

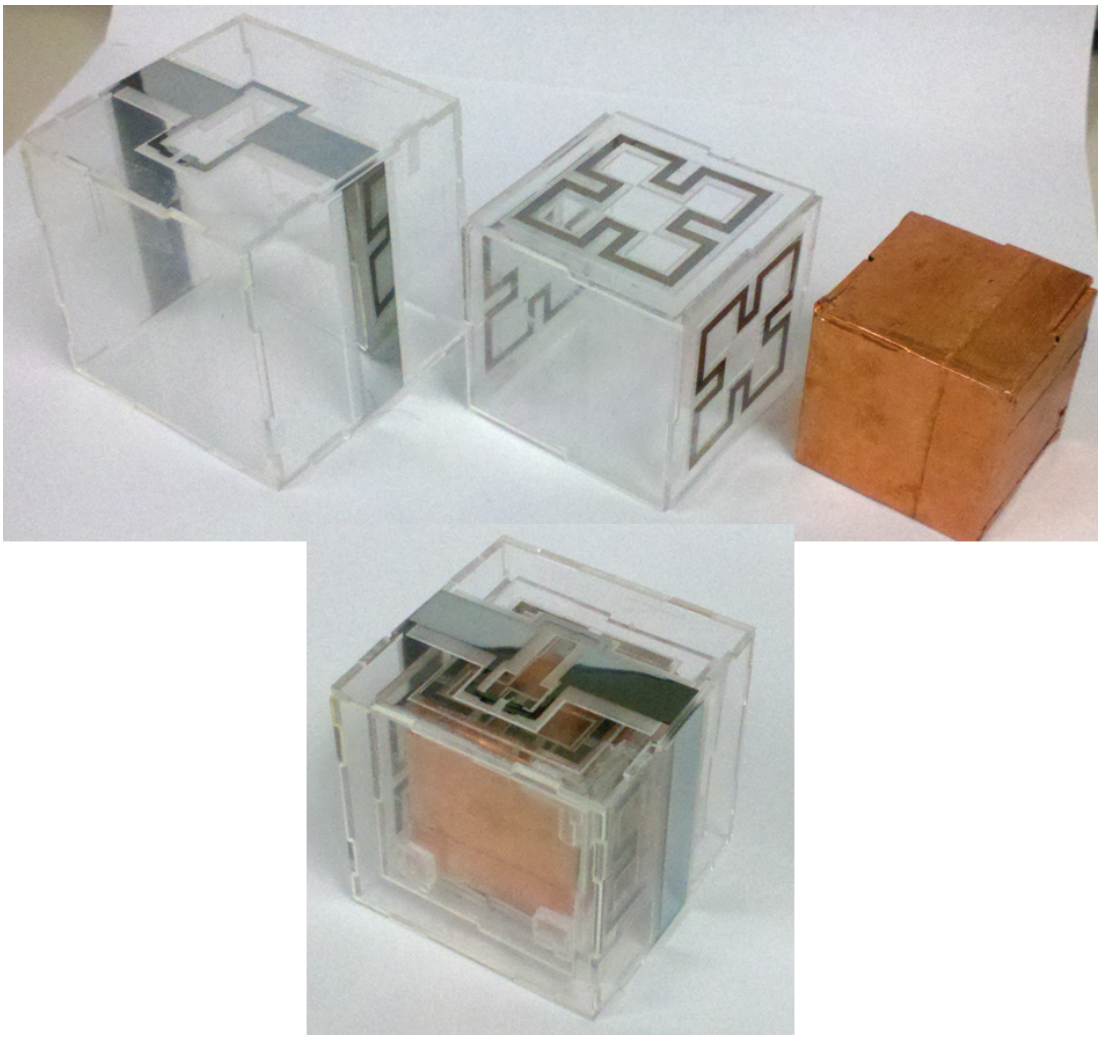

Figure 6.13: Picture of the full topology before and after final fabrication.

the full 3D radiation pattern, at its center operating frequency of 900 MHz. As can be seen, the cube is near-isotropic in its gain pattern with the gain variance at about 3 dB for the simulated cube and less than 4.5 dB for the measured.

Fig. 15(a) and 15(b) show the gain variance of the cube across the international spectrum, around which the cube was designed, in both the XZ and YZ planes, respectively. As can be seen, the gain variance stays within 6 dB across the full spectrum.

In order to demonstrate the gain of the cube topology, several commercially sold RFID tags are measured and compared to the cube. Each tag is measured from its respective direction of peak gain. The gain plots of the topology against commercially available tags can be seen in fig. 6.16. Here the peak gain of the commercially sold tags is compared to the peak and minimum gain of the topology. As can be seen, the peak gain of the topology is comparable to the peak gain of commercialy sold tags. In addition, since the commercially sold tags are all based on augmented dipole designs, their gain drops off by more than half when 30ff from the direction of peak gain; and the tags have a read range of less than 1cm when viewed from near 90ff from the direction of peak gain. This is as oppose to the topology, which when viewed from any direction, is still readable at around the same distance. Table T2 shows the required power for activation as each tag is rotated through a plane which contains both a direction of peak gain and direction of minimum gain. As can be seen, by 45 the cube has about the same gain as the Intermec and Omni-ID antenna; and beyond 45 the cube antenna outperforms both tags.

6.5 Conclusion

Presented above is a topology that acts as a near-isotropic radiator with an isolated core. Its performance is proven through comparison to commercially available RFID tags, and to other published isotropic radiators and isolated-core radiators. This

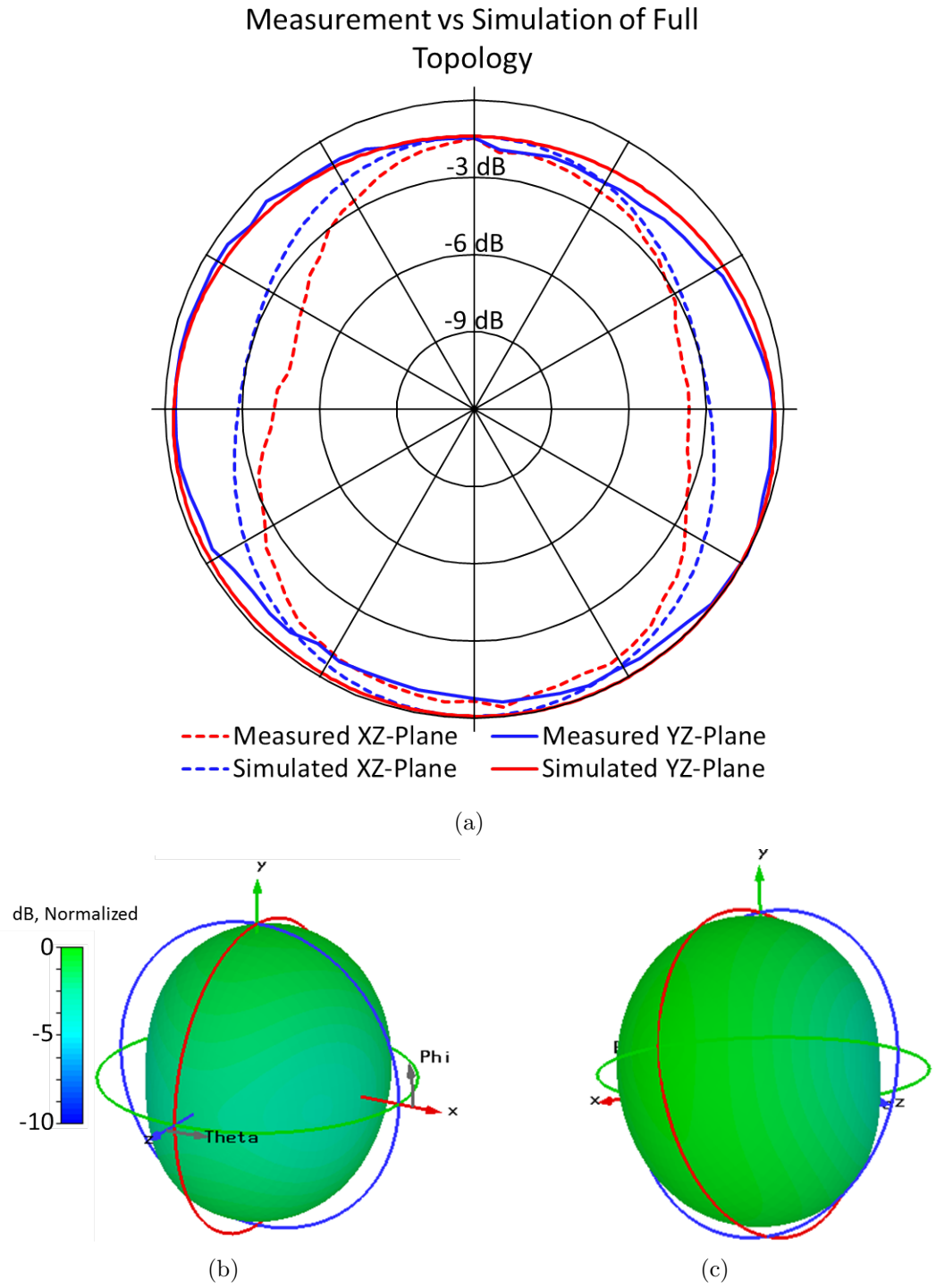

Figure 6.14: (a) Overlay of Measured and Simulated radiatin patterns in the XZ Plane and YZ Plane, and (a) front and (b) back 3D images of the simulated, normalized radiation pattern.

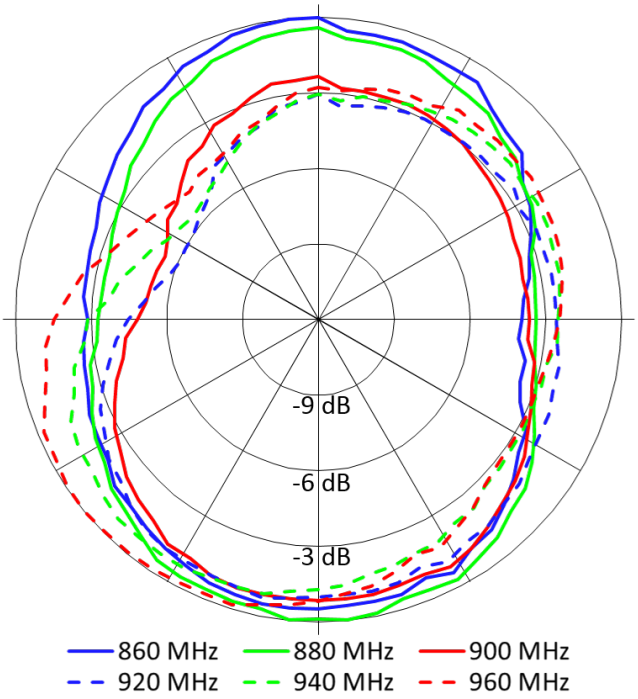

(a)

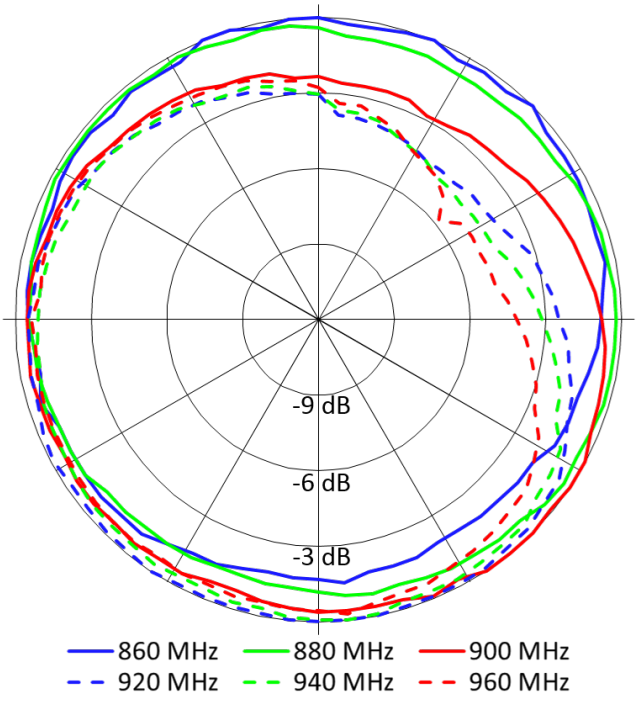

(b)

Figure 6.15: Overlay of the measured radiation patterns across a wide band for the (a) E-plane and (b) H-plane.

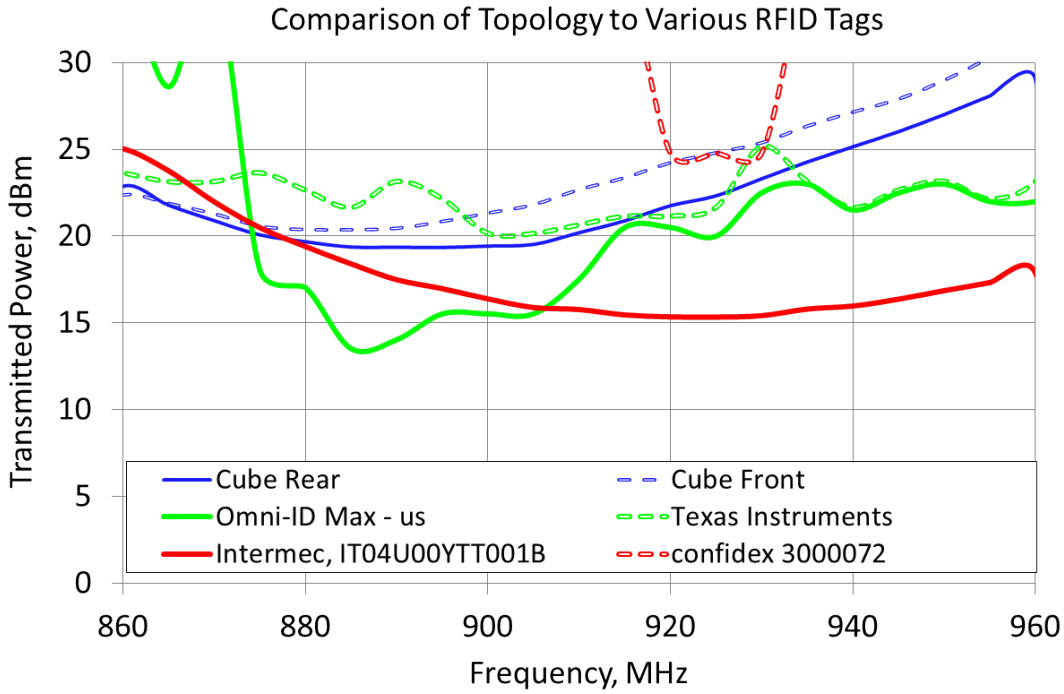

Figure 6.16: Overlay of the required power for activation over the 860 to 960 MHz band for different commercially sold tags when read from the direction of maximum gain with that of the topology when interrogated by the direction of maximum and minimum gain at 900 MHz.

T2 2: The required transmitted power required to activate the cube topology tag, the Intermec tag, and the Omni-ID tag, as the tags are rotated through a plane containing both the direction of maximum and minimum gain.

Angle (deg)	0°	22.5°	45.0°	67.5°	90.0°
Cube Topology	19.42	20.16	21.43	22.70	23.91
Intermec	16.38	17.47	20.39	28.64	null
Omni-ID	15.52	16.37	19.51	27.76	null

topology shows the first fully implemented conformal AMC, which was inkjet printed on PMMA. Through the construction of this topology, PMMA has been demonstrated as a more viable substrate for use in inkjet printed electronics. In addition, a demonstration in designing conforaml AMC devies is presented, and the outline is given for moving to other arbitray 3D shapes in AMC implementation.

This chapter serves to present the full methodology, and basis therefore, for the fabrication of the final topology. Through the demonstration of the cube being fabricated on a paper substrate, it has been shown that the cube can be produced on a rapid, low cost basis. Through the demonstration of a PMMA construction, the topology is shown to be compatible with a smart skin, microfluidic sensor platform.

In all this, the cube is shown to be versatile, not only in its performance, as is shown in the prior chapter, but also in its implementation through fabrication.

CHAPTER VII

INTEGRATED, MICROFLUIDIC SENSOR

One of the many uses of cheaply deployable antennas is in the area of remote sensor systems. To this end, many different types of sensors are investigated which can make use of the cube antenna. One such is a microfluidic test system. As is described in the fabrication section, the microfluidic system can be constructed using inkjet printing of silver traces and SU8 photo resist, in combination with the use of etched PMMA sheets. As the antenna already makes use of inkjet printing silver, and etched PMMA as a substrate, the topology is a prime device for incorporating microfluidics.

In this chapter, a microfluidic system is designed and tested, which makes use of the printing of silver and SU8, in combination with etched PMMA sheets. The fabrication of the microfluidic sensor, as well as the basic parts around which the design is based, can be seen in the fabrication section. This chapter, and the corresponding section in the fabrication chapter, are taken from two separate papers published by Cook and Cooper et al [17]. This chapter contains a paraphrase of the design, while the fabrication section found in the prior chapter contains a direct excerpt.

7.1 Introduction

Fluid quality and content measurements are of great importance in many areas. Sewage treatment needs to track particulates in fluid before reclaiming or releasing; potable product production needs to track potential contaminants or to check for correct mixtures; and biomedical applications need to perform bio-assays and blood analysis. Traditionally, these tests are performed in an environment that requires large quantities of fluid for testing; the majority of which is wasted in dead volume for filling test containers, and which is never utilized in the analysis process. For

potable production, this is wasted product; and for biomedical, this is extra tissue taken from a subject.

Microfluidic systems solve the problem of unnecessary waste in fluid volume. By using MEMS techniques, the entire microfluidic system, including fluid flow channels, fluidic manipulation structures, and sensing electronics is constructed in a single package. The monolithic design in a micro scale structure allows for minimal fluid requirement. However, the construction of these devices requires the use of costly and time consuming clean room techniques, such as photolithography and metal sputtering. Beyond the cost, these fabrication techniques also create waste material, some of which are extremely harmful to the environment.

Techniques have been pursued which allow for simpler, lower cost, more rapid fabrication [51,55,89]. Those these techniques reduce the cost and waste of the above mentioned nano scale techniques; they still require some clean room procedures. The goal of the below described design is not to minimize cleanroom procedures, but to completely eliminate them.

The basis of these design is taken from Cook et al [17]. The design is based upon a varactor that is tuned by the presence of fluids passed through sealed channels.

7.2 Basic Theory: Varactors

The basis of these design is taken from Cook et al [17]. The design is based upon a varactor that is tuned by the presence of fluids passed through sealed channels.

Table 7.2 shows the electrical properties, at microwave frequencies, of a few fluids. As can be seen, the properties of these fluids are drastically different. Due to the high values of parameters, like permittivity, these fluids could be used in microwave devices to alter the device's performance.

The most basic method of achieving this change in performance is through the use of fluid tunable varactors. A simple varactor design can be seen in fig 1(a). The

T3 3: Electrical Parameters at 900 MHz and 300 K [71, 78]

Fluid	Re(Permittivity), ϵ'	Im(Permittivity), ϵ"
Water	73	5
Ethanol	15	11
Hexanol	3	2.5

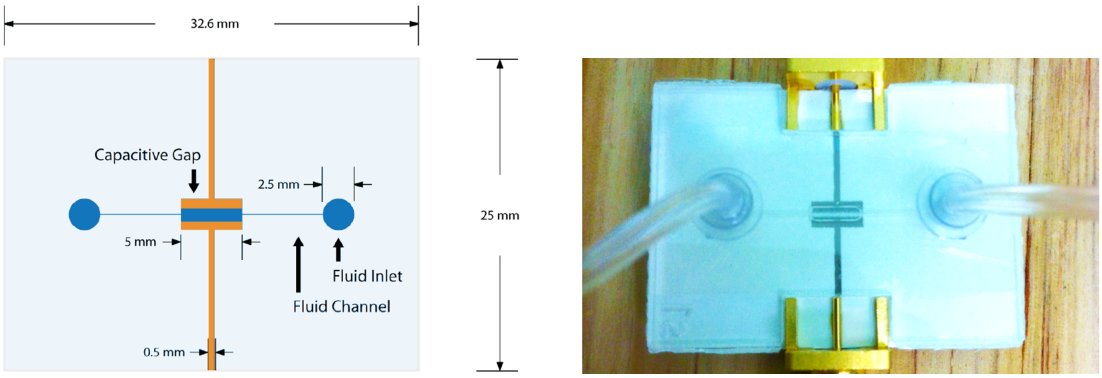

(a) (b)

Figure 7.1: (a) Schematic of fabricated microfluidic varactor, and (b) fabricated microfluidic varactor with mounted SMA connectors for performing microwave capacitance measurements

varactor consists of a planar capacitive structure with a 500 μm gap which is fed using microstrip feed lines. A 500 μm deep fluid cavity etched in PMMA is bonded directly over the gap to allow for delivery of the fluid. When different fluids are sent through the cavity, the E-field distribution and D-field intensity change. This change in fields leads to a different capacitance between the two plates.

The fabrication of the device, shown in fig. 1(b), is outlined in chapter VII. This design is fed with different fluids and measured for proof of concept.

Along with these caps, TRL calibration structures are fabricated to de-embed the microstrip feeds, and measure the S-parameter derived capacitances. De-embedding of the connectors and feed lines is performed using WinCal. The highest capacitance value has a resonance at 4 GHz. Since the capacitance becomes very non-linear near that point, the capacitances are only shown up to 2.5 GHz.

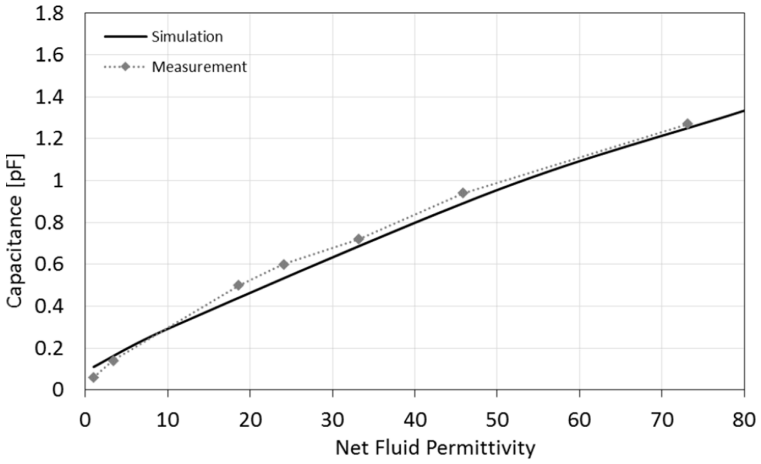

Figure 7.2: (a,b) De-embedded frequency dependent capacitance of the microfluidic varactor for different fluids, and (c) simulated versus measured varactor capacitance for different fluid permittivities

The varactor was tested using mixtures of different fluids which contain large variation in their permittivity and loss tangent, including water, ethanol and hexanol. A plot of the extracted capacitance versus permittivity can be seen in fig. 7.2. Here, the measured capacitance is compared to simulated capacitance using a lossless fluid. From this plot, it can be seen that the loss tangent plays a very small role in the total capacitance.

It is this basic concept of a fluid tunable varactor which has led to the creation of a fully additive process manufactured, low cost, re-usable, wirelessly interrogated, passive, microfluidic sensor.

7.3 Passive Wireless Lab on Chip

Moving away from wired microwave components, an area of potential high impact which can be enabled by the fluid varactor is wireless microfluidic-based lab-on-chip. Wireless lab-on-chip systems allow for the remote analysis of fluids in biomedical, production, and potentially hazardous environemnts where wired measurements are not feasible or cost effective. Currently, however, wireless lab-on-chip systems require

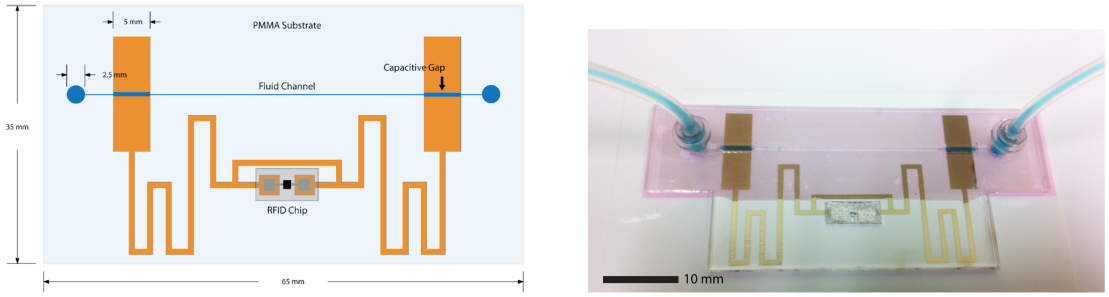

(a) (b)

Figure 7.3: (a) Schematic of the full lab-on-chip showing antenna and fluidic channels/cavities and (b) picture of fabricated design

a power source which increases cost and decreases life span.

By utilizing the microfluidic varactor to tune an RFID antenna, a completely passive RFID-based lab on chip platform is demonstrated for the first time. The design for the microfluidic RFID antenna is shown in Fig. 7.3 which consists of a meandered dipole antenna, fluid varactors to change the electrical length of the antenna, and a T-matching network for the RFID chip which will be used for communication. The microfluidic RFID antenna is designed to match the impedance of the Alien Technologies Higgs 3 EPC Gen-2 RFID chip which is approximately $16+j200$ ohms. As the readable range of the Voyantic Tagformance reader is 800-1000 MHz, the antenna is designed to resonate near 1000 MHz when empty so that the downward shifts caused by the introduction of fluid can be captured. The design is optimized for these parameters using the CST frequency domain solver. The same capacitor-gap model extracted from the previous section is utilized to simulate the expected resonant shifts in the antenna.

To confirm the agreement of the fabricated tag with the simulation before wireless backscatter measurements are performed, a cabled measurement of the return loss of the antenna is performed using a Rhode and Schwartz ZVA-8 VNA. The measured S-parameters are then re-normalized to the RFID chip impedance as displayed in Fig 4(a). The return loss shows matching at 1 GHz when the channel is empty

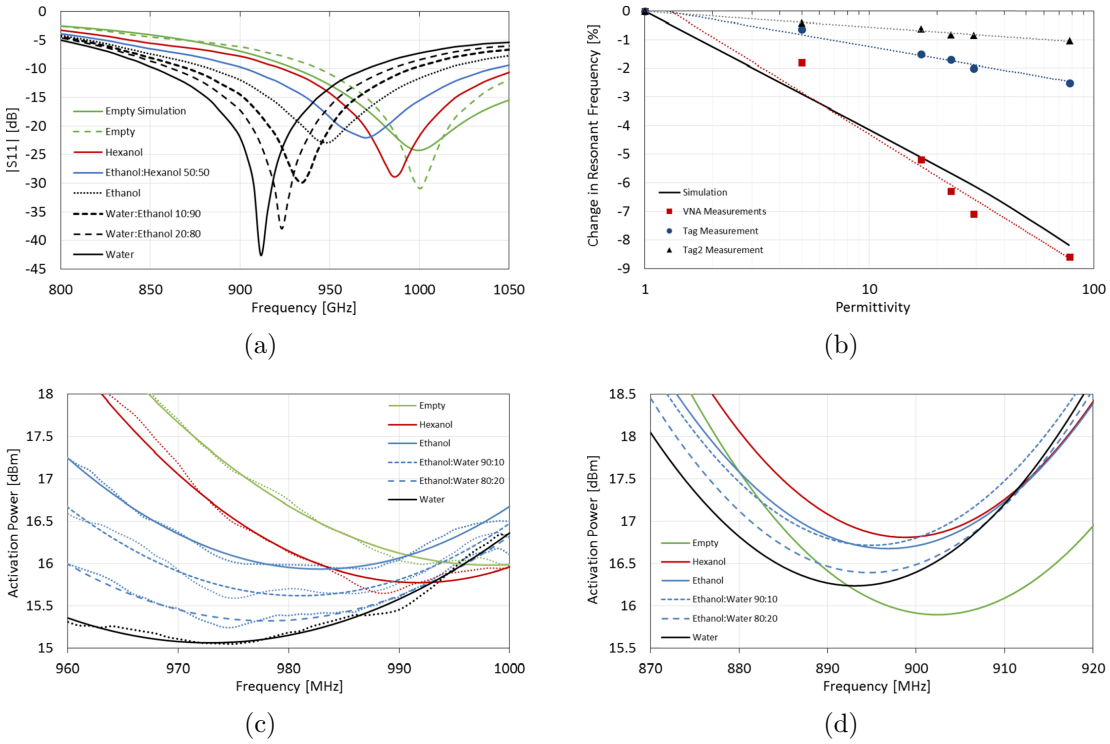

Figure 7.4: (a) Measured S-parameters of the microfluidic RFID tag, (b) Comparison of simulated and measured return loss of the microfluidic RFID antenna, along with wireless chip measurements, (c) curve fit backscatter data of a microfluidic tag with resonant frequency of 1 GHz, and (d) curve fit backscatter data of a microfluidic tag with resonant frequency of 900 MHz

which is confirmed in simulation. The various fluids utilized in the previous sections are then pumped through the fluidic channels while the return loss is measured. Distinct downward shifts in the resonance confirm that the fluidic channel is loading the capacitive gap on the antenna and increasing the electrical length. Large shifts of nearly 100 MHz are achieved in the cabled measurement. The shifts experienced in the cabled measurement are compared with simulation utilizing the gap model in Fig. 4(b) and the best fit curves show a difference below 6%.

Following cabled verification of the passive microfluidic tag, the Alien RFID chip is mounted on the tag and a wireless measurement setup is constructed as displayed in Fig. 7.5. The tag is placed 0.5 m away from the reader antenna of the Tagformance which interrogates the tag across the 800 1000 MHz band. The Tagformance returns

data on power required to activate the tag, and the reflected power and phase versus frequency. Again, the tag is measured with an empty channel, and all of the fluids used in the cabled measurement. The data returned from the Tagformance which is shown in Fig. 4(c) displays the transmit power required to activate the tag versus frequency along with the second order curve fit in Matlab which is used to extract the resonant frequency. A clear downward shift in the resonant frequency is experienced as higher permittivity fluids are sent through the channel as is expected, and the resonant shift versus fluid permittivity is plotted in Fig 4(b) against simulation and cabled measurement. After all of the liquid measurements are performed, the tag is emptied and again measured. The extracted resonant frequency of the empty tag is within a fraction of a percent of the empty measurement before being Fig. 7.5. This demonstrates a high degree of repeatability which is important in long-term monitoring situations. It is noticed that the activation power slightly decreases with the higher permittivity fluids which is due to the improving matching between the antenna and chip impedance. The T-match is designed so that optimal matching occurs when the antenna resonant frequency is 900 MHz. It is seen from Fig. 4(b) that the wireless tag exhibits lower shifts than the cabled measurement, and this is due to the variation in chip impedance over frequency which is not taken into account in the simulation or cabled measurement. The variation in chip impedance along with the T-match cause a decreased sensitivity.

To test the effects of the chip impedance versus frequency on the sensitivity of the wireless lab-on-chip, a second version of the tag is fabricated in which the center frequency of tag antenna is tuned to 900 MHz by slightly increasing the length of the antenna. The Higgs 3 RFID chip typically has its own internal resonance around 900 MHz as well which will overshadow some of the effects of the change in the electrical length of the antenna. By repeating the same procedure for wireless measurements with the previous tag, the curve-fit data of backscatter versus fluid flow is shown

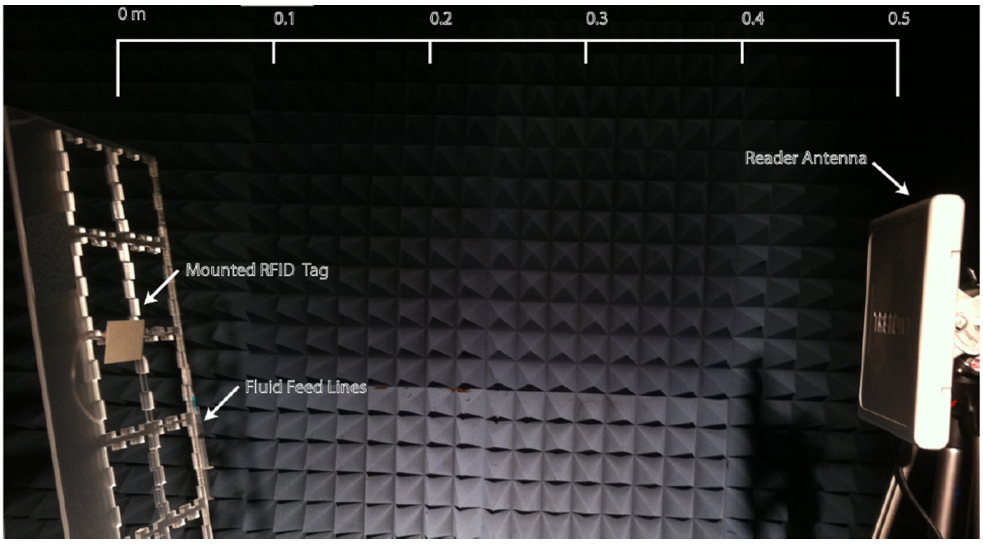

Figure 7.5: Measurement setup of the wireless lab-on-chip RFID tag

in Fig. 4(b). The resulting sensitivity is even lower than previous tag as the chip resonance begins to overshadow the electrical length change of the antenna.

7.4 Conclusions

Utilizing a novel low-cost inkjet fabrication technique, varactors, and completely passive wireless lab on chip systems have been demonstrated. The microfluidic sensing platform shows highly repeatable results with sensitvities high enough to detect as little as 1% water in ethanol while using under 3 uL of fluid. The low-cost platform has applications in lab-on-chip, bio-monitoring, and real time water and chemical analysis and monitoring.

Due to the use of microfluidic channels being etched into PMMA sheets, and the cube topology being constructed from PMMA, this sensor system lends itself to easy integration into the cube topology.

CHAPTER VIII

ANTI-COLLISION METHODOLOGY FOR FREQUENCY DOUBLERS

In the pursuit of constructing a complete topology, a robust method of communication is needed. This chapter presents the first ever hardware based methodology for collision avoidance of multiple, frequency doubling transceivers. This chapter is based on the work from Cooper et al [23], and contains excerpts there from.

Frequency doubling transceivers have many advantages over other passive RFID systems, including their simplicity, size, and read range. The drawback of frequency doubling transceivers is the lack of a method for uniquely identifying a single tag when multiple tags are within read range of an interrogator, i.e. collision avoidance. Therefore, a methodology is developed which allows for the switching on and off of individual tags while maintaining a relatively simple and small structure. Measurement demonstrates a switching mechanism which requires -10 dBm of power in a control signal for over 30 dBm of attenuation in the transceiver's doubled return power. Different modes of operation are demonstrated which allow for easier signal interrogation. Wireless measurements demonstrate the viability of the transceiver as part of an RFID system. Read range, and number of uniquely identifiable tags are covered in the conclusion.

8.1 Introduction

Frequency doubling transceivers have been used in RFID systems since the 70's [33]. Frequency doublers have the advantages of being simple (and thus reliable), small, low cost, passive, long range (for a passive tag), and, due to the use of harmonics

of the interrogating signal, are easily distinguishable from the backscatter of the interrogation signal [10, 13]. These transceivers are shown to be very useful in remote wireless sensors, due to being broadband, resilient to environmental effects, and easily detuned for smart skin applications [1, 67, 87].

The drawback of the frequency doubling transceiver is the lack of unique identifiability between multiple tags. When multiple transceivers are within the range of an interrogator, all tags will respond with the same second harmonic signal. This identical response makes it impossible for the interrogator to distinguish between tags. Therefore, the goal of this paper is to present a method for distinguishing between multiple frequency doubling transceivers without greatly increasing the complexity of the transceiver, and thus mainting its advantages of the transceiver.

This chapter presents the anti-collision method, which can be seen in fig 8.1, in the following three sections. First, the general theory of frequency doublers is covered, along with a proposed method of switching doublers "on" and "off". Second, an analysis of the doublers utilizing the switching mechanism is performed with cables and gernators in order to demonstrate the viability of the design. Finally, a wireless measurement of the doubler with switching mechanism is performed in order to show the viability of the full system.

8.2 Theory and Design

Frequency doubers for transceivers are constructed in either a half-wave rectifier configuration [1], or a full-wave rectifier configuration [2]. Due to their high switching speed and saturation current, schottky diodes are used in constructing the doubler circuits. The operation of the schottky diode can be described by

$$\boldsymbol{I} = \frac{\mathrm{d}\boldsymbol{V}}{\mathrm{d}\boldsymbol{t}}\boldsymbol{C_j} + \boldsymbol{I_s}(\boldsymbol{e}^{\frac{\boldsymbol{V}-\boldsymbol{I_{res}}\boldsymbol{R_s}}{\boldsymbol{nKT}}} - \mathbf{1}) \tag{1}$$

where $\boldsymbol{I}$ is the current through the diode, $\boldsymbol{V}$ is the voltage across the diode, $\boldsymbol{C_j}$

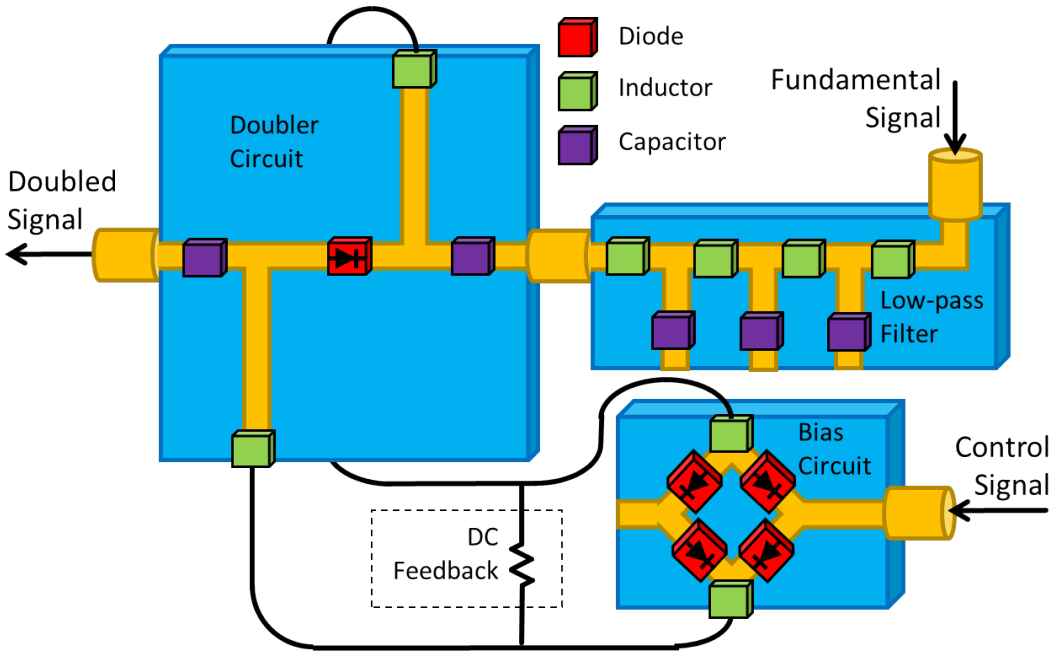

Figure 8.1: Diagram of the frequency doubling transceiver with anti-collision DC biasing source, and harmonic supressing Lowpass filter.

is the junction capacitance across the diode, $\boldsymbol{I_s}$ is the saturation current, $\boldsymbol{R_s}$ is the series resistance in the diode, $\boldsymbol{I_{res}}$ is the current through the series reistor, n is the ideality factor, K is the Boltzmann constant, and T is the thermal point of the diode in Kelvin. From this equation, it can be seen that the diode conducts well in the forward bias, while being highly resistive when placed in a reverse bias (i.e. V<0). When a signal passes across the diode, the positive half of the wave is allowed to go through and the negative half is cutoff. This non-linearity generates both a DC signal and harmonics of the original signal.

From (1), $\boldsymbol{V}$ can be pictured as the superposition of two signals: a DC biasing signal, $\boldsymbol{V_{bias}}$, and an AC signal, $\boldsymbol{V_{sig}}$ (i.e. $\boldsymbol{V = V_{bias} + V_{sig}}$). If $\boldsymbol{V_{bias}}$ is kept near zero, then $\boldsymbol{V_{sig}}$ will generate a nonlinear $\boldsymbol{I}$, and thus have a large conversion ratio from the fundamental frequency of $\boldsymbol{V_{sig}}$, $\boldsymbol{f_0}$, to the second harmonic of that frequency, $\boldsymbol{f_1}$. However, if $\boldsymbol{V_{bias}}$ were to be a positive value near the turn-on value of the schottky diode, then (1) would approach

$$\boldsymbol{I_{sig}} = \frac{\mathrm{d}\boldsymbol{V_{sig}}}{\mathrm{d}\boldsymbol{t}}\boldsymbol{C_j} + \frac{\boldsymbol{V_{sig}}}{\boldsymbol{R_s}} \tag{2}$$

where $\boldsymbol{I_{sig}}$ is the current generated by the $\boldsymbol{V_{sig}}$ component of $\boldsymbol{V}$. In this case, $\boldsymbol{I_sig}$ would be linear with regards to $\boldsymbol{V_{sig}}$, and no harmonics generated. In essence, the frequency doubler would be turned off. Based upon this concept, a switching mechanism can be generated for a frequency doubler if a power source can be used to selectively turn a DC bias on and off. It is this mechanism on which the anti-collision method is based. The only thing needed is a method of generating a DC $\boldsymbol{V_{bias}}$ that can be turned on and off.

8.3 Design

A full-wave rectifier is chosen as the means for generating $\boldsymbol{V_{bias}}$ from a control signal. The rectifier was chosen due to its high conversion rate from a fundamental signal to a DC signal in comparison to a half-wave rectifier, and its simplicity in design in comparison to an equivalent output voltage charge pump.

The full-wave rectifier is fed by a 13.56 MHz control signal. AC chokes are placed at either end of the bias line in order to prevent AC signal mixing; and a 1 kohm resistor is placed in shunt in order to allow discharging of the doubling diode, and thus improve performance.

Due to the harmonics generated by the function generator, a 5 stage Chebyshev, low-pass filter, normalized to 50 ohms, is placed at the input of the doubler circuit to block these unwanted harmonics. A DC block is also placed at the input of the doubler circuit in order to prevent the DC signal from being shorted out in either the input source or the output load. The complete system diagram can be seen in fig 8.1.

The proof-of-concept system is fed by a 235 MHz fundamental signal operating at -10 dBm. Fig 2(a) shows the power output from the system, into a 50 ohm load, in the absense of a control signal going into the biasing circuit, and when there are

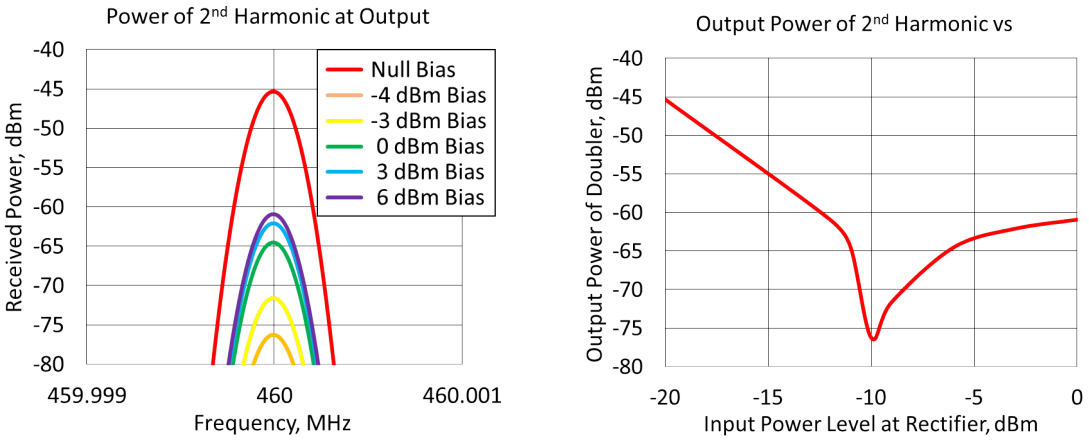

(a) (b)

Figure 8.2: Plots of the power of the 470 MHz signal out of the doubler circuit, with a fundamental signal at -10 dBm power at 235MHz, vs input power of the 13.56MHz control signal, (a) plotted in the frequency domain, and (b) plotted againt each eachother

varying levels of power going into the biasing circuit. Fig 2(b) demonstrates a unique trend in the 2nd harmonic output power vs control signal power, wherein the control signal hits an optimal control signal power level for attenuation of the doubler circuit, and then suffers a decrease in attenuation as the power level increases.

This trend is most likely due to the shift in input impedance of the frequency doubler as a function of bias power. Though the bias signal attenuates the doublers performance, the decrease in $|\boldsymbol{S_{11}}|$, and thus increase in power transferred to the doubler, cancels out the attenuation until the control signal is powerful enough to overcome the improved $|\boldsymbol{S_{11}}|$. A plot of the input impedance at the 235 MHz fundamental signal input versus control signal power level can be seen in fig 8.3.

As fig 2(b) shows, an attenuation of over 30 dB can be achieved. This attenuation is sufficient, for most cases, for determining what transceiver is being interrogated. However, if an AM control signal were to be used, it may become easier to recognize that an individual transceiver is being interrogated. Fig 8.4 shows the time domain output of the doubling circuit when the biasing circuit is fed with a 13.56MHz control

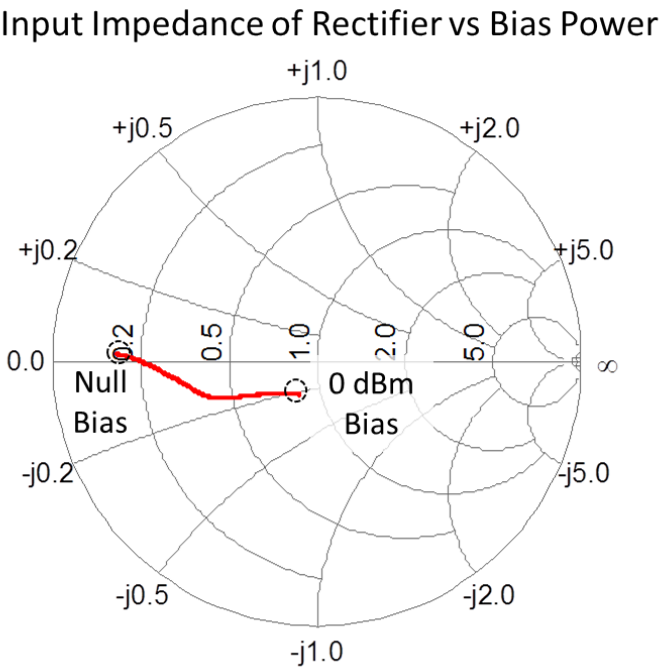

Figure 8.3: The input impedance of the frequency doubler at 235 MHz under a range of biasing circuit input powers

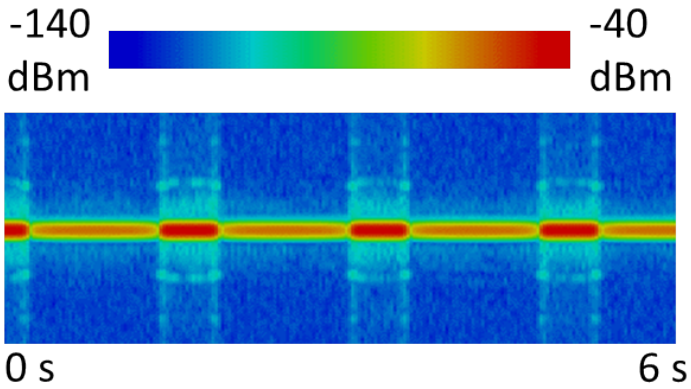

Figure 8.4: Time domain spectrograph of the output power of the doubler circuit when the biasing circuit is fed with a 2 Hz sinusiodal wave

signal amplitude modulated with a 2Hz signal.

If an interrogator signal is activating multiple doubling transceivers simultaneously, a single frequency control signal is being broadcast, and each transceiver has a unique, narrow band-pass filter on its bias circuit, then only the tag which can receive the control signal's frequency is attenuated. If the control signal is amplitude modulated, then the interrogator need only mask out all but the periodically attenuating signal in order to verify which tag is being read.

8.4 Wireless Testing

Fig 5(a) shows the setup used to measure the performance of the transceiver. Here the fundamental and the biasing signal are generated by function generators, which are fed directly into their respective circuits. A 470 MHz antenna is connected to the output of the doubler circuit, like in fig 8.1.

With an input power of 0 dBm into the doubler circuit and no power sent to the bias circuit, $\approx$ -55 dBm is received at the input to the spectrum analyzer. This power level can be seen in fig 5(b). Likewise, 6 dB of attenuation can also be seen in fig 5(b), where a 1 dBm signal has been put into the biasing circuit. This decrease in attenuation, in comparison to the above shown results, is most likely due to a shift in the matching of the doubler caused by using a 280 ohm folded dipole at the load, instead of the 50 ohm load input of the spectrum analyzer which was used before.

Fig 5(c) shows that despite the decrease in attenuation, the second harmonic can still be amplitude modulated by a sinusoidal wave being fed to the biasing circuit, and thus make unique identification possible.

The limiting factor in the read range of the transciever is the control signal. While Presas et al showed that only -30 dBm is needed on the terminals of the frequency doubler for operation [67], this research shows that around -5 to 0 dBm is needed on

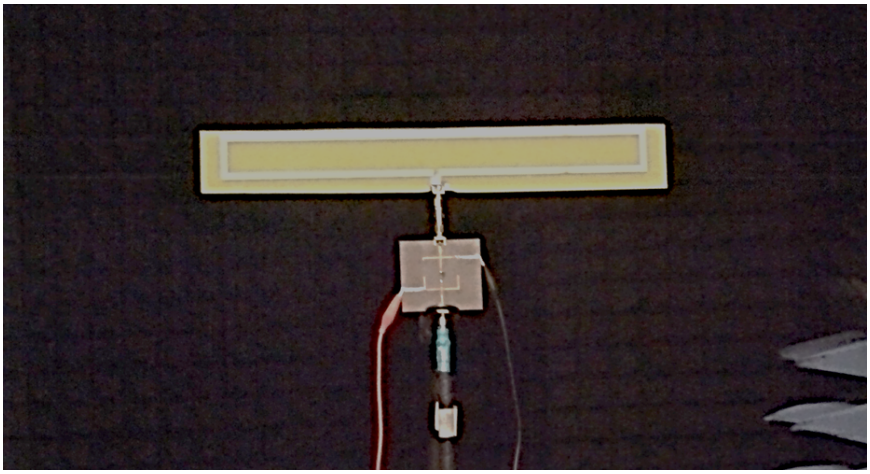

(a)

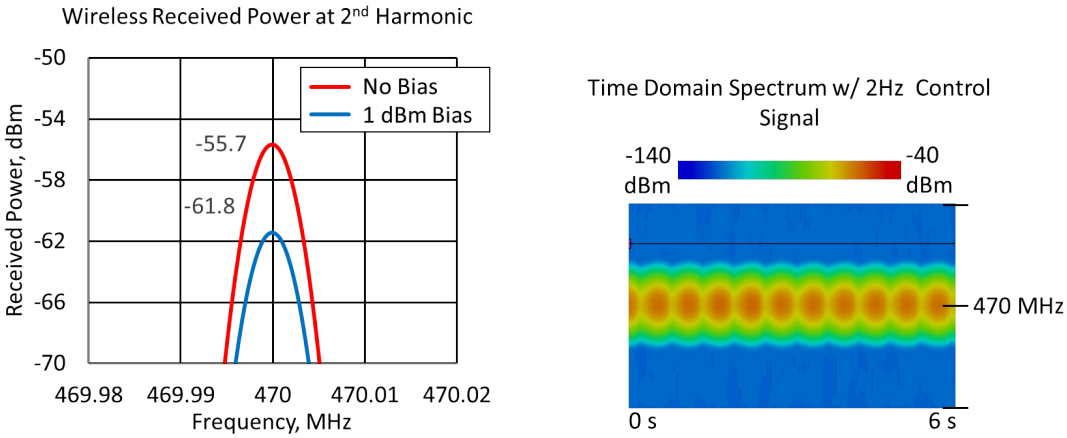

(b) (c)

Figure 8.5: (a) Image of the wireless test setup with (b) a frequency domain plot of the received doubled frequency at two control signal power levels, and (c) a time domain plot of the received doubled frequency when the control signal is amplitude modulated

the terminals of the bias network. This limits read range to about 5 meters (assuming 1W transmitted power, and an isotropic receive antenna). However, since the biasing circuit is a receive antenna and rectifier, or rectenna, Trotter et al [79] shows that read range can be greatly increased through the use of power optimized waveforms. If modified waveforms are used, then the limitation is on the doubler circuit and the theoretical read range goes back to 20 meters.

In order to be uniquely identifiable, each frequency doubling transceiver requires a unique frequency for the control signal. Therefore, the limiting factor in the number of tags which can be read is the allowed bandwidth of the control signal's frequency, and the quality factor of any bandpass filter placed on the input of the biasing network.

8.5 Conclusions

Utilizing the non-linear characteristics of a frequency doubler, combined with the simplicity of a full wave rectifier, the first hardware-based, anti-collision methodology for frequency doubling transceivers is developed. The methodology is shown to generate an on/off ratio of over 30 dB for the frequency doubler with as little as -10 dBm at the input to the rectifier. Furthermore, the methodology is shown to be functional in a wireless setting with at least 5 meters of read range, but up to 20 meters if an optimized control signal waveform is used. In addition to backscatter noise avoidance inherent in the frequency doubling transceiver, the methodology provides a means of amplitude modulation of the doubled return signal in order to further distinguish the return signal from the noise floor. This shows the anti-collision methodology to not only be viable, but desirable in RFID systems.

CHAPTER IX

CONCLUSION

Thus far is presented a complete RFID topology. This topology has focused around the design construction of a novel radiator, along with the development of an embeddable microfluidic sensor, and an integrate-able, hardware-based, anti-collision system for frequency doubling RFID.

The design of the radiator has included the development of the first ever, functional, AMC surface. The use of this surface has allowed the radiator to achieve both a near isotropic radiation pattern and a completed EMI isolated core for hardware embedding. The analysis of the operation of the AMC unit cells within a conformal structure, as presented within, servers to open the use of FSS and AMC surfaces to a wider range of applications. This work has directly led to one publication and one paper under review for publication by the author on the operation of the radiator [26,27]. It has been preceded by six papers by the author covering antenna design and testing [21, 22, 29, 31, 49, 76], one paper by the author covering the operation of frequency selective surfaces [25], and one US patent by the author [11].

The construction of the radiator, along with the development of the microfluidic sensor, has shown a wider versatility in the use of inkjet printing technology, specifically as it applies to 3D and multi-layer structures, and in its ability to utilize a wider range of substrate materials. The presented work outlines the exact steps for the fabrication of these devices, so as to open the field of inkjet printed electronics up to any application which may make need of 3D and multi-layer structures. The work on inkjet printed microfluidic sensors has directly lead to two publications by the author [14,17]. The fabrication techniques used have lead to four publications by

the author, not including those listed above [15, 16, 18, 24, 48]. The work on printed sensors is proceeded by three publications by the author in strain sensing [86–88].

The development of the hardware-based, anti-collision system has shown how a reliable, passive, low cost method of RFID, i.e. frequency doubling, can be used in a wide range of application in which frequency doubler RFIDs were unusable. The analysis of the operation of the doubler, as well as the presentation of the different ways in which the system could be implemented, has broadened the field of RFID technology to a wider range of applications where low cost, simple, and small devices are required for long range reading. The work in frequency doubling RFID nodes has lead to two publications by the author [23, 87].

In the pursuit of furthering the field, this work has to lead to 23 publications, and one US patent, which have been cited by 41 independent papers, yielding an h-index of 4 for the author.

REFERENCES

[1] Aguilar, S. M. and Weller, T. M., "Tunable harmonic re-radiator for sensing applications," in *Microwave Symposium Digest, 2009. MTT'09. IEEE MTT-S International*, pp. 1565–1568, IEEE, 2009.

[2] Alimenti, F., Palazzari, V., Orecchini, G., Pinca, G., Mezzanotte, P., Tentzeris, M., and Roselli, L., "Crossed dipole frequency doubling rfid tag based on paper substrate and ink-jet printing technology," in *Microwave Symposium Digest (MTT), 2010 IEEE MTT-S International*, pp. 840–842, IEEE, 2010.

[3] Back, F., "Lens tester for photographic lenses," *Review of Scientific Instruments*, vol. 21, no. 8, pp. 722–724, 1950.

[4] Balbin, I. and Karmakar, N. C., "Phase-encoded chipless rfid transponder for large-scale low-cost applications," *Microwave and Wireless Components Letters, IEEE*, vol. 19, no. 8, pp. 509–511, 2009.

[5] Barton, R. J., "Achievable performance and effective interrogator design for saw rfid sensor tags," in *Aerospace Conference, 2012 IEEE*, pp. 1–16, IEEE, 2012.

[6] Bayatpur, F. and Sarabandi, K., "Single-layer high-order miniaturized-element frequency-selective surfaces," *Microwave Theory and Techniques, IEEE Transactions on*, vol. 56, no. 4, pp. 774–781, 2008.

[7] Berge, L. and Reich, M., "A uhf rfid antenna for a wireless sensor platform with a near-isotropic radiation pattern," in *RFID (RFID), 2013 IEEE International Conference on*, pp. 88–95, 2013.

[8] Biancotto, C. and Record, P., "Triangular lattice dielectric amc antenna," *Antennas and Wireless Propagation Letters*, vol. 9, pp. 95–98, 2010.

[9] Biresaw, G. and Carriere, C., "Surface energy parameters of polymers from directly measured interfacial tension with probe polymers," *Journal of adhesion science and technology*, vol. 18, no. 14, pp. 1675–1685, 2004.

[10] Bouthinon, M., Gavan, J., and Zadworny, F., "Passive microwave transposer, frequency doubler for detecting the avalanche victims," in *Microwave Conference, 1980. 10th European*, pp. 579–583, IEEE, 1980.

[11] Carr, W. and Cooper, J. R., "Rfid tag with open-cavity antenna structure," 08 2011.

[12] Chamarti, A. and Varahramyan, K., "Transmission delay line based id generation circuit for rfid applications," *Microwave and Wireless Components Letters, IEEE*, vol. 16, no. 11, pp. 588–590, 2006.

[13] Colpitts, B. G. and Boiteau, G., "Harmonic radar transceiver design: miniature tags for insect tracking," *Antennas and Propagation, IEEE Transactions on*, vol. 52, no. 11, pp. 2825–2832, 2004.

[14] Cook, B. S., Cooper, J. R., Kim, S., and Tentzeris, M. M., "A novel inkjet-printed passive microfluidic rfid-based sensing platform," in *Microwave Symposium Digest (IMS), 2013 IEEE MTT-S International*, pp. 1–3, IEEE, 2013.

[15] Cook, B. S., Cooper, J. R., and Tentzeris, M. M., "Vertically-integrated inkjet printed electronics process (vipre) for high efficiency rf and mm-wave components," in *the Printed Electronics Industry , 6th LOPEC International Conference on*, pp. 1–3, in press, May 2014. Messe Munchen, Germany.

[16] Cook, B. S., Mariotti, C., Cooper, J. R., Revier, D., Aluigi, L., Roselli, L., Tehrani, B., and Tentzeris, M. M., "Inkjet-printed, vertically-integrated, high-performance inductors and transformers on flexible lcp substrate," in *Microwave Symposium Digest (IMS), 2014 IEEE MTT-S International*, pp. 1–3, IEEE, 2014.

[17] Cook, B., Cooper, J., and Manos, M., "An inkjet-printed microfluidic rfid-enabled platform for wireless lab-on-chip applications," *Microwave Theory and Techniques, IEEE Transactions on*, p. in press, 2013.

[18] Cook, B., Cooper, J., and Tentzeris, M., "Multi-layer rf capacitors on flexible substrates utilizing inkjet printed dielectric polymers," *Microwave and Wireless Components Letters, IEEE*, vol. 23, no. 7, pp. 353–355, 2013.

[19] Cook, B. and Shamim, A., "Inkjet printing of novel wideband and high gain antennas on low-cost paper substrate," *Antennas and Propagation, IEEE Transactions on*, vol. 60, no. 9, pp. 4148–4156, 2012.

[20] Cook, B. and Shamim, A., "Utilizing wideband amc structures for high-gain inkjet-printed antennas on lossy paper substrate," *Antennas and Wireless Propagation Letters, IEEE*, vol. 12, pp. 76–79, 2013.

[21] Cook, B., Tehrani, B., Cooper, J., and Tentzeris, M., "Multilayer inkjet printing of millimeter-wave proximity-fed patch arrays on flexible substrates," *Antennas and Wireless Propagation Letters, IEEE*, vol. 12, pp. 1351–1354, 2013.

[22] Cooper, J., Weller, T., DiStasi, S., and Frolik, J., "An electronically reconfigurable reverberation chamber for the emulation of severe multipath channels," in *Wireless and Microwave Technology Conference, 2009. WAMICON'09. IEEE 10th Annual*, pp. 1–4, IEEE, 2009.

[23] Cooper, J. R., Cook, B. S., and Tentzeris, M. M., "The first hardware-based, anti-collision methodology for frequency doubling transceivers for rfid and wireless sensing applications," in *Proceedings IMS, in press*, 2014.

[24] Cooper, J. R., Cook, B. S., and Tentzeris, M. M., "Fully inkjet printed, multi-layer lithium-ion battery," in *the Printed Electronics Industry , 6th LOPEC International Conference on*, pp. 1–3, in press, May 2014. Messe Munchen, Germany.

[25] Cooper, J. R., Kim, S., and Tentzeris, M. M., "A novel polarization-independent, free-space, microwave beam splitter utilizing an inkjet-printed, 2-d array frequency selective surface," *Antennas and Wireless Propagation Letters, IEEE*, vol. 11, pp. 686–688, 2012.

[26] Cooper, J. R., Kim, S., and Tentzeris, M. M., "Inkjet-printed, 3d, near isotropic radiating, wireless sensing platforms utilizing conformal amc topologies," *Transactions on Antennas and Wireless Propagation, IEEE*, 2014.

[27] Cooper, J. R. and Tentzeris, M. M., "Novel "smart cube" wireless sensors with embedded processing/communication/power core for "smart skins" applications," in *Sensors, 2012 IEEE*, pp. 1–4, IEEE, 2012.

[28] Coor, T. and Smith, D. C., "An automatic recording spectrophotometer," *Review of Scientific Instruments*, vol. 18, no. 3, pp. 173–181, 1947.

[29] DiStasi, S., Melais, S., Ketcham, R., Zivanovic, B., Cooper, J., Frolik, J., and Weller, T., "A compact, reconfigurable chamber for emulating severe multipath fading," in *Antennas and Propagation Society International Symposium, 2008. AP-S 2008. IEEE*, pp. 1–4, IEEE, 2008.

[30] Foroozesh, A. and Shafai, L., "On the design of high-gain resonant cavity antennas using different highly-reflective frequency selective surfaces as the superstrates," in *Antennas and Propagation Society International Symposium (APSURSI), 2010 IEEE*, pp. 1–4, IEEE, 2010.

[31] Frolik, J., Weller, T. M., DiStasi, S., and Cooper, J., "A compact reverberation chamber for hyper-rayleigh channel emulation," *Antennas and Propagation, IEEE Transactions on*, vol. 57, no. 12, pp. 3962–3968, 2009.

[32] Gao, J., Siden, J., and Nilsson, H.-E., "Printed electromagnetic coupler with an embedded moisture sensor for ordinary passive rfid tags," *Electron Device Letters, IEEE*, vol. 32, no. 12, pp. 1767–1769, 2011.

[33] Gavan, J., "Transponders for the detection and identification of remote cooperative targets," in *Telesystems Conference, 1994. Conference Proceedings., 1994 IEEE National*, pp. 229–232, IEEE, 1994.

[34] Gonzalo, R., De Maagt, P., and Sorolla, M., "Enhanced patch-antenna performance by suppressing surface waves using photonic-bandgap substrates," *Microwave Theory and Techniques, IEEE Transactions on*, vol. 47, no. 11, pp. 2131–2138, 1999.

[35] Hanna, S., "Rf and microwave applications to saw propagation in magnetic films," in *Ultrasonics Symposium, 1989. Proceedings., IEEE 1989*, pp. 121–124, IEEE, 1989.

[36] Hansen, R., "Effects of a high-impedance screen on a dipole antenna," *Antennas and Wireless Propagation Letters, IEEE*, vol. 1, no. 1, pp. 46–49, 2002.

[37] Harma, S., Plessky, V. P., Hartmann, C. S., and Steichen, W., "Z-path saw rfid tag," *Ultrasonics, Ferroelectrics and Frequency Control, IEEE Transactions on*, vol. 55, no. 1, pp. 208–213, 2008.

[38] Harma, S., Arthur, W. G., Hartmann, C. S., Maev, R. G., and Plessky, V. P., "Inline saw rfid tag using time position and phase encoding," *Ultrasonics, Ferroelectrics and Frequency Control, IEEE Transactions on*, vol. 55, no. 8, pp. 1840–1846, 2008.

[39] Hartmann, C., Hartmann, P., Brown, P., Bellamy, J., Claiborne, L., and Bonner, W., "Anti-collision methods for global saw rfid tag systems," in *Ultrasonics Symposium, 2004 IEEE*, vol. 2, pp. 805–808, IEEE, 2004.

[40] Hartmann, C. S., "A global saw id tag with large data capacity," in *Ultrasonics Symposium, 2002. Proceedings. 2002 IEEE*, vol. 1, pp. 65–69, IEEE, 2002.

[41] Hind, D., "Radio frequency identification and tracking systems in hazardous areas," in *Fifth International Conference on 1994*, pp. 215–227, 1994.

[42] Huchard, M., Delaveaud, C., and Tedjini, S., "Miniature antenna for circularly polarized quasi isotropic coverage," in *Antennas and Propagation, 2007. EuCAP 2007. The Second European Conference on*, pp. 1–5, 2007.

[43] Hwang, R.-B., Hsu, N.-C., and Chin, C.-Y., "A spatial beam splitter consisting of a near-zero refractive index medium," *Antennas and Propagation, IEEE Transactions on*, vol. 60, no. 1, pp. 417–420, 2012.

[44] Kaiser, U. and Steinhagen, W., "A low-power transponder ic for high-performance identification systems," *Solid-State Circuits, IEEE Journal of*, vol. 30, no. 3, pp. 306–310, 1995.

[45] Karmakar, N. C., *Handbook of smart antennas for RFID systems*. Wiley Online Library, 2010.

[46] Kiani, G., Ford, K., Esselle, K., and Weily, A., "Oblique incidence performance of an active square loop frequency selective surface," in *Antennas and Propagation, 2007. EuCAP 2007. The Second European Conference on*, pp. 1–4, 2007.

[47] Kim, I. K. and Varadan, V., "Flexible isotropic antenna using a split ring resonator on a thin film substrate," in *Antennas and Propagation (APSURSI), 2011 IEEE International Symposium on*, pp. 3333–3335, 2011.

[48] Kim, S., Cook, B. S., Le, T., Cooper, J. R., Lee, H., Lakafosis, V., Vyas, R., Moro, R., Bozzi, M., and Georgiadis, A., "Inkjet-printed antennas, sensors and circuits on paper substrate," *IET Microwaves, Antennas, and Propagation*, vol. 7 (10), pp. 858–868, May 2014. Messe Munchen, Germany.

[49] Kim, S., Cook, B., Cooper, J., Traille, A., Georgiadis, A., Aubert, H., and Tentzeris, M. M., "A novel dual-band retro-directive reflector array on paper utilizing substrate integrated waveguide (siw) and inkjet printing technologies for chipless rfid tag and sensor applications," in *Microwave Symposium Digest (IMS), 2013 IEEE MTT-S International*, pp. 1–4, IEEE, 2013.

[50] Kim, S., Tentzeris, M., and Nikolaou, S., "Wearable biomonitoring monopole antennas using inkjet printed electromagnetic band gap structures," in *Antennas and Propagation (EUCAP), 2012 6th European Conference on*, pp. 181–184, 2012.

[51] Klank, H., Kutter, J. P., and Geschke, O., "Co2-laser micromachining and back-end processing for rapid production of pmma-based microfluidic systems," *Lab on a Chip*, vol. 2, no. 4, pp. 242–246, 2002.

[52] Kurokawa, K., "Power waves and the scattering matrix," *Microwave Theory and Techniques, IEEE Transactions on*, vol. 13, no. 2, pp. 194–202, 1965.

[53] Laakso, P., Ruotsalainen, S., Halonen, E., Mäntysalo, M., and Kemppainen, A., "Sintering of printed nanoparticle structures using laser treatment," in *In: Ostendorf, A., Graf, T., Petring, D. & Otto, A.(eds.). Proceedings of the Fifth International WLT-Conference on Lasers in Manufacturing, LIM 2009, June 15-18, 2009, Munich, Germany*, 2009.

[54] Liu, J. and Yao, J., "Wireless rf identification system based on saw," *Industrial Electronics, IEEE Transactions on*, vol. 55, no. 2, pp. 958–961, 2008.

[55] Martinez, A. W., Phillips, S. T., Wiley, B. J., Gupta, M., and Whitesides, G. M., "Flash: a rapid method for prototyping paper-based microfluidic devices," *Lab on a Chip*, vol. 8, no. 12, pp. 2146–2150, 2008.

[56] McVay, J., Hoorfar, A., and Engheta, N., "Space-filling curve rfid tags," in *Radio and Wireless Symposium, 2006 IEEE*, pp. 199–202, IEEE, 2006.

[57] Monti, G., Catarinucci, L., Vasanelli, C., and Tarricone, L., "3d patch antenna using a cardbord substrate for rfid reader applications," in *Microwave Conference (EuMC), 2012 42nd European*, pp. 884–887, 2012.

[58] Nair, R., Perret, E., and Tedjini, S., "Chipless rfid based on group delay encoding," in *RFID-Technologies and Applications (RFID-TA), 2011 IEEE International Conference on*, pp. 214–218, IEEE, 2011.

[59] Pan, G., Li, Y., Zhang, Z., and Feng, Z., "An isotropic-radiated planar antenna using two crossed dipoles," in *Microwave and Millimeter Wave Technology (ICMMT), 2012 International Conference on*, vol. 3, pp. 1–4, 2012.

[60] Parker, E. and El Sheikh, A., "Convoluted array elements and reduced size unit cells for frequency-selective surfaces," in *Microwaves, Antennas and Propagation, IEE Proceedings H*, vol. 138, pp. 19–22, IET, 1991.

[61] Parker, E. and Hamdy, S., "Rings as elements for frequency selective surfaces," *Electronics Letters*, vol. 17, no. 17, pp. 612–614, 1981.

[62] Pierantoni, L., Mencarelli, D., Rozzi, T., Alimenti, F., Roselli, L., and Lugli, P., "Multiphysics analysis of harmonic rfid tag on paper with embedded nanoscale material," in *Antennas and Propagation (EUCAP), Proceedings of the 5th European Conference on*, pp. 3009–3010, IEEE, 2011.

[63] Preradovic, S., Karmakar, N., and Balbin, I., "Rfid transponders," *Microwave Magazine, IEEE*, vol. 9, no. 5, pp. 90–103, 2008.

[64] Preradovic, S. and Karmakar, N. C., "Design of fully printable planar chipless rfid transponder with 35-bit data capacity," in *Microwave Conference, 2009. EuMC 2009. European*, pp. 013–016, IEEE, 2009.

[65] Preradovic, S. and Karmakar, N. C., "Multiresonator based chipless rfid tag and dedicated rfid reader," in *Microwave Symposium Digest (MTT), 2010 IEEE MTT-S International*, pp. 1520–1523, IEEE, 2010.

[66] Preradovic, S., Roy, S. M., and Karmakar, N. C., "Rfid system based on fully printable chipless tag for paper-/plastic-ltem tagging," *Antennas and Propagation Magazine, IEEE*, vol. 53, no. 5, pp. 15–32, 2011.

[67] Presas, S. M., Weller, T. M., Silverman, S., and Rakijas, M., "High efficiency diode doubler with conjugate-matched antennas," in *Microwave Conference, 2007. European*, pp. 250–253, IEEE, 2007.

[68] Reindl, L., Shrena, I., Kenshil, S., and Peter, R., "Wireless measurement of temperature using surface acoustic waves sensors," in *Frequency control symposium and PDA exhibition jointly with the 17th European frequency and time forum, 2003. Proceedings of the 2003 IEEE international*, pp. 935–941, IEEE, 2003.

[69] Rida, A., Yang, L., Vyas, R., Basat, S., Bhattacharya, S. K., and Tentzeris, M. M., "Novel manufacturing processes for ultra-low-cost paper-based rfid tags with enhanced," in *Electronic Components and Technology Conference, 2007. ECTC'07. Proceedings. 57th*, pp. 773–776, IEEE, 2007.

[70] Roselli, L., Alimenti, F., Virili, M., Lolli, F., Popescu, B., Popescu, D., Locci, S., and Lugli, P., "Feasibility study of a fully organic frequency doubler for harmonic rfid applications," in *Silicon Monolithic Integrated Circuits in RF Systems (SiRF), 2012 IEEE 12th Topical Meeting on*, pp. 203–206, IEEE, 2012.

[71] Shibata, K., "Measurement of complex permittivity for liquid materials using the open-ended cut-off waveguide reflection method," *IEICE transactions on electronics*, vol. 93, no. 11, pp. 1621–1629, 2010.

[72] Shrestha, S., Balachandran, M., Agarwal, M., Phoha, V. V., and Varahramyan, K., "A chipless rfid sensor system for cyber centric monitoring applications," *Microwave Theory and Techniques, IEEE Transactions on*, vol. 57, no. 5, pp. 1303–1309, 2009.

[73] Sievenpiper, D., Zhang, L., and Yablonovitch, E., "High-impedance electromagnetic ground planes," in *Microwave Symposium Digest, 1999 IEEE MTT-S International*, vol. 4, pp. 1529–1532, IEEE, 1999.

[74] Sievenpiper, D., Zhang, L., Broas, R. F., Alexopolous, N. G., and Yablonovitch, E., "High-impedance electromagnetic surfaces with a forbidden frequency band," *Microwave Theory and Techniques, IEEE Transactions on*, vol. 47, no. 11, pp. 2059–2074, 1999.

[75] Skeie, H. and Armstrong, D., "Passive interrogator label system with a surface acoustic wave transponder operating at its third harmonic and having increased bandwidth," Apr. 12 1988. US Patent 4,737,790.

[76] Tehrani, B., Cook, B. S., Cooper, J. R., and Tentzeris, M. M., "Inkjet printing of a wideband, high gain mm-wave vivaldi antenna on a flexible organic substrate," in *Antennas and Propogation, 2014 IEEE International Symposium on*, pp. 1–3, in press, July 2014. Memphis, TN.

[77] Thai, T., Ratner, J., Chen, W., DeJean, G., and Tentzeris, M. M., "Characterization and testing of novel polarized nanomaterial textiles for ultra-sensitive wireless gas sensors," in *Electronic Components and Technology Conference, 2009. ECTC 2009. 59th*, pp. 1049–1052, IEEE, 2009.

[78] Tidar, A., Shafiyoddin, S., Kamble, S., Dharne, G., Patil, S., Khirade, P., and Mehrotra, S., "Microwave dielectric relaxation study of 1-hexanol with 1-propenol mixture by using time domain reflectometry at 300k," in *Applied Electromagnetics Conference (AEMC), 2009*, pp. 1–4, IEEE, 2009.

[79] Trotter, M., Griffin, J., and Durgin, G., "Power-optimized waveforms for improving the range and reliability of rfid systems," in *RFID, 2009 IEEE International Conference on*, pp. 80–87, 2009.

[80] Virga, K. and Rahmat-Samii, Y., "Low-profile enhanced-bandwidth pifa antennas for wireless communications packaging," *Microwave Theory and Techniques, IEEE Transactions on*, vol. 45, no. 10, pp. 1879–1888, 1997.

[81] Vyas, R., Lakafosis, V., Konstas, Z., and Tentzeris, M. M., "Design and characterization of a novel battery-less, solar powered wireless tag for enhanced-range remote tracking applications," in *Microwave Conference, 2009. EuMC 2009. European*, pp. 169–172, IEEE, 2009.

[82] Vyas, R., Lakafosis, V., and Tentzeris, M., "Wireless remote localization system utilizing ambient rf/solar power scavenging rfid tags," in *Microwave Symposium Digest (MTT), 2010 IEEE MTT-S International*, pp. 1764–1767, IEEE, 2010.

[83] Wang, H., Nezich, D., Kong, J., and Palacios, T., "Graphene frequency multipliers," *Electron Device Letters, IEEE*, vol. 30, no. 5, pp. 547–549, 2009.

[84] Watanabe, R., "A novel polarization-independent beam splitter," *Microwave Theory and Techniques, IEEE Transactions on*, vol. 28, no. 7, pp. 685–689, 1980.

[85] Yang, L., Orecchini, G., Shaker, G., Lee, H.-S., and Tentzeris, M. M., "Battery-free rfid-enabled wireless sensors," in *Microwave Symposium Digest (MTT), 2010 IEEE MTT-S International*, pp. 1528–1531, IEEE, 2010.

[86] Yi, X., Cooper, J., Wang, Y., Tentzeris, M., and Leon, R., "Wireless crack sensing using an rfid-based folded patch antenna," in *Proc. 6th Int'l Conf. Bridge Maint. Safety Manag.(IABMAS 2012)*, 2012.

[87] Yi, X., Lantz, G., Cooper, J., Cho, C., Wang, Y., Tentzeris, M., and Leon, R., "Sensing resolution and measurement range of a passive wireless strain sensor," in *Proceedings of the 8th International Workshop on Structural Health Monitoring, Stanford, CA., USA*, 2011c.

[88] Yi, X., Cho, C., Fang, C.-H., Cooper, J., Lakafosis, V., Vyas, R., Wang, Y., Leon, R., and Tentzeris, M., "Wireless strain and crack sensing using a folded patch antenna," in *Antennas and Propagation (EUCAP), 2012 6th European Conference on*, pp. 1678–1681, March 2012.

[89] Yuen, P. K. and Goral, V. N., "Low-cost rapid prototyping of flexible microfluidic devices using a desktop digital craft cutter," *Lab on a Chip*, vol. 10, no. 3, pp. 384–387, 2010.

VITA

Perry H. Disdainful was born in an insignificant town whose only claim to fame is that it produced such a fine specimen of a researcher.